University of Groningen

The spin temperature of high-redshift damped Lyman α systems

Kanekar, N.; Prochaska, J. X.; Smette, A.; Ellison, S. L.; Ryan-Weber, E. V.; Momjian, E.; Briggs, F. H.; Lane, W. M.; Chengalur, J. N.; Delafosse, T.

IMPORTANT NOTE: You are advised to consult the publisher's version (publisher's PDF) if you wish to cite from it. Please check the document version below.

Document Version
Publisher's PDF, also known as Version of record

Link to publication in University of Groningen/UMCG research database

The spin temperature of high-redshift damped Lyman α systems

N. Kanekar,[1][*][†] J. X. Prochaska,[2] A. Smette,[3] S. L. Ellison,[4] E. V. Ryan-Weber,[5] E. Momjian,[6] F. H. Briggs,[7] W. M. Lane,[8] J. N. Chengalur,[1] T. Delafosse,[2] J. Grave,[2] D. Jacobsen[4] and A. G. de Bruyn[9,10]

[1]*National Centre for Radio Astrophysics, TIFR, Post Bag 3, Ganeshkhind, Pune 411 007, India*
[2]*UCO/Lick Observatory, UC Santa Cruz, Santa Cruz, CA 95064, USA*
[3]*European Southern Observatory, Alonso de Cordova 3107, Casilla 19001, Vitacura, Santiago, Chile*
[4]*Department of Physics and Astronomy, University of Victoria, BC V8P 1A1, Canada*
[5]*Swinburne University of Technology, Mail H30, PO Box 218, Hawthorn, VIC 3122, Australia*
[6]*National Radio Astronomy Observatory, 1003 Lopezville Road, Socorro, NM 87801, USA*
[7]*RSAA, The Australian National University, Mount Stromlo Observatory, ACT 2611, Australia*
[8]*Naval Research Laboratory, Code 7213, 4555 Overlook Ave SW, Washington, DC 20375, USA*
[9]*Kapteyn Astronomical Institute, University of Groningen, PO Box 800, NL-9700 AV Groningen, the Netherlands*
[10]*ASTRON, PO Box 2, NL-7990 AA Dwingeloo, the Netherlands*

ABSTRACT

We report results from a programme aimed at investigating the temperature of neutral gas in high-redshift damped Lyman α absorbers (DLAs). This involved (1) H I 21 cm absorption studies of a large sample of DLAs towards radio-loud quasars, (2) very long baseline interferometric studies to measure the low-frequency quasar core fractions, and (3) optical/ultraviolet spectroscopy to determine DLA metallicities and the velocity widths of low-ionization metal lines. Including literature data, our sample consists of 37 DLAs with estimates of the harmonic mean spin temperature T_s. We find a statistically significant (4σ) difference between the T_s distributions in the high-z ($z > 2.4$) and low-z ($z < 2.4$) DLA samples. The high-z sample contains more systems with high spin temperature, $T_s \gtrsim 1000$ K. The T_s distributions in DLAs and the Galaxy are also significantly ($\approx 6\sigma$) different, with more high-T_s sightlines in DLAs than in the Milky Way. The high T_s values in the high-z DLAs of our sample arise due to low fractions of the cold neutral medium (CNM). Only 2 of 23 DLAs at $z > 1.7$ have T_s values indicating CNM fractions >20 per cent, comparable to the median value (≈ 27 per cent) in the Galaxy. We tested whether the H I column density measured towards the optical quasar might be systematically different from that towards the radio core by comparing the H I column densities inferred from H I 21 cm emission studies at different spatial resolutions (≈ 15 pc-1 kpc) in the Large Magellanic Cloud. The high-resolution $N_{H I}$ values are, on average, larger than the smoothed ones for $N_{H I} > 10^{21}$ cm^{-2}, but lower than the smoothed $N_{H I}$ estimates for $N_{H I} < 10^{21}$ cm^{-2}. Since there are far more DLAs with low $N_{H I}$ values than high ones, the use of the optical $N_{H I}$ value for the radio sightline results in a statistical tendency to underestimate DLA spin temperatures. For 29 DLAs with metallicity estimates, we confirm the presence of an anticorrelation between T_s and metallicity [Z/H], at 3.5σ significance via a non-parametric Kendall-tau test. This result was obtained with the assumption that the DLA covering factor is equal to the core fraction. However, Monte Carlo simulations show that the significance of the result is only marginally decreased if the covering factor and the core fraction are uncorrelated, or if there is a random error in the inferred covering factor. We also find statistically significant

[*] E-mail: nkanekar@ncra.tifr.res.in
[†] Ramanujan Fellow.

evidence for redshift evolution in DLA spin temperatures even for the DLA sub-sample at $z > 1$. Since all DLAs at $z > 1$ have angular diameter distances comparable to or larger than those of their background quasars, they have similar efficiency in covering the quasars. We conclude that low covering factors in high-z DLAs cannot account for the observed redshift evolution in spin temperatures.

Key words: ISM: evolution – galaxies: high-redshift – quasars: absorption lines – radio lines: ISM.

1 INTRODUCTION

Quasar absorption spectra offer the possibility of selecting galaxies by their absorption signatures, and thus obtaining samples of high-z galaxies without a bias towards the most luminous systems. The highest H I column density absorbers detected in quasar spectra are the damped Lyman α systems (DLAs). With H I column densities $N_{\rm H I} \geq 2 \times 10^{20}$ cm^{-2} (Wolfe, Gawiser & Prochaska 2005), similar to values seen in sightlines through the Milky Way and nearby gas-rich galaxies, DLAs have long been identified as the high-redshift counterparts of normal galaxies in the local Universe. The nature of galaxies that give rise to DLAs at different redshifts, and their typical size, mass, kinematic structure and physical conditions are all important ingredients for understanding galaxy evolution.

The Sloan Digital Sky Survey (SDSS; Abazajian et al. 2009) has resulted in the detection of a vast number of DLAs at high redshifts, with nearly 7000 candidate absorbers now known at $z > 2.2$ (e.g. Prochaska, Herbert-Fort & Wolfe 2005; Noterdaeme et al. 2009, 2012b; Prochaska & Wolfe 2009). Unfortunately, contamination from the background quasars has made it very difficult to identify the host galaxy of the DLAs in optical images (e.g. Warren et al. 2001; but see Fumagalli et al. 2010). The low sensitivity of today's radio telescopes has meant that one cannot image the DLA hosts in the standard radio H I 21 cm and CO emission lines that have been used for detailed studies of the kinematics and dynamics of nearby galaxies. And, even following a number of recent studies, only a handful of high-z DLAs have been detected in Hα or Lyα emission (e.g. Møller, Fynbo & Fall 2004; Fynbo et al. 2010, 2011; Noterdaeme et al. 2012a; Péroux et al. 2012), with typical star formation rates (SFRs) $\lesssim$ few M$_\odot$ per year (Péroux et al. 2012), even for high-metallicity absorbers. Thus, despite much effort over the last three decades, relatively little information has so far been gleaned from emission studies of DLAs.

Detailed absorption studies remain our primary source of information about the absorbers. Around 200 DLAs have measured metallicities, elemental abundances and kinematics, from high-resolution optical echelle spectroscopy (e.g. Pettini et al. 1994, 1997, 1999, 2008; Prochaska et al. 2003a, 2007; Dessauges-Zavadsky et al. 2004; Khare et al. 2004; Ledoux et al. 2006; Petitjean, Ledoux & Srianand 2008; Penprase et al. 2010; Cooke et al. 2011; Battisti et al. 2012). These studies have yielded interesting results. For example, mean DLA metallicities have been shown to increase with decreasing redshift, as expected from models of galaxy evolution, although low-metallicity DLAs are quite common even at low redshifts (Prochaska et al. 2003b; Kulkarni et al. 2005, 2010; Rafelski et al. 2012). A positive correlation has been found between the metallicity and both the velocity spreads of low-ionization metal lines (Wolfe & Prochaska 1998; Ledoux et al. 2006) and the rest equivalent width of the Si II λ1526 line (Prochaska et al. 2008a). This has been interpreted as evidence for a mass–metallicity relation in DLAs, similar to that seen in emission-selected high-z galaxies (e.g. Tremonti et al. 2004; Savaglio et al. 2005; Erb et al. 2006; Neeleman et al. 2013). Molecular hydrogen (H$_2$) absorption, along with C I absorption, has been detected in about a dozen DLAs, with strong upper limits on the molecular fraction in $\sim$80 per cent of the observed systems (e.g. Levshakov & Varshalovich 1985; Ge & Bechtold 1997; Ge, Bechtold & Kulkarni 2001; Ledoux, Petitjean & Srianand 2003; Noterdaeme et al. 2008; Jorgenson, Wolfe & Prochaska 2010; Milutinovic et al. 2010). This has provided information on local conditions in the molecular phase, including estimates of the number density, temperature and strength of the ultraviolet (UV) radiation field (e.g. Srianand et al. 2005), along with measurements of the microwave background temperature at different redshifts (e.g. Noterdaeme et al. 2011).

While absorption spectra have yielded many successes in DLA studies, the fact that they only trace a pencil beam through each galaxy implies that many of the major questions in the field remain to be answered. For example, the asymmetric wings seen in low-ionization metal-line profiles were originally thought to imply an origin in rapidly rotating thick discs (Prochaska & Wolfe 1997), but have also been shown to arise naturally in hierarchical merging scenarios (Haehnelt et al. 1998; but see Prochaska & Wolfe 2010), dwarf galaxy ejecta (Nulsen, Barcons & Fabian 1998) and outflows from starburst galaxies (Schaye 2001). The star formation histories of $z > 2$ DLAs, deduced from their elemental abundances, indicate an unambiguous origin in dwarf irregular galaxies for a few DLAs (Dessauges-Zavadsky et al. 2006), but also suggest that all the absorbers do not arise in a single galaxy class (Dessauges-Zavadsky et al. 2007). On the other hand, the large velocity spreads seen in a number of DLAs and the curious paucity of systems with narrow velocity spreads ($\Delta V \lesssim 30$ km s^{-1}) are difficult to reconcile with an origin in dwarf galaxies (e.g. Prochaska & Wolfe 1997; Wolfe et al. 2005). The complications of interpreting absorption spectra have meant that even basic questions pertaining to the typical size and structure of DLAs, and their redshift evolution, remain issues of controversy.

H I 21 cm emission studies of high-redshift DLAs are currently not possible owing to the weakness of the H I 21 cm line and the low sensitivity of today's radio telescopes; the highest redshift at which H I 21 cm emission has been detected is $z \approx 0.26$ (Catinella et al. 2008). However, H I 21 cm absorption studies of DLAs lying towards radio-loud quasars provide an important tool both to study physical conditions in the neutral gas in the absorbers and to probe fundamental constant evolution. For DLAs lying towards extended background radio sources, H I 21 cm absorption studies provide a measure of the spatial extent of the neutral gas as well as the opacity-weighted velocity field, although such studies have only so far been possible in a couple of DLAs (e.g. Briggs et al. 1989; Kanekar & Briggs 2004). Conversely, for DLAs towards compact radio sources, a comparison between the H I column density measured from the Lyman α absorption profile and the integrated H I 21 cm optical depth yields the spin temperature $T_{\rm s}$ of the absorbing gas. In

addition, for compact targets, comparisons between the redshifts of H I 21 cm absorption lines and those of other transitions (e.g. resonant UV lines, OH Lambda-doubled lines, rotational lines; Wolfe et al. 1976; Drinkwater et al. 1998; Chengalur & Kanekar 2003) can be used to test for changes in the fundamental constants of physics.

The spin temperature contains information on the distribution of neutral gas between the different temperature phases of the interstellar medium (ISM) in the absorber, specifically on the fractions of warm and cold gas. The fact that the spin temperature appeared systematically higher in high-z DLAs than in the Galaxy has made T_s a quantity of interest in DLA studies for the last three decades (e.g. Wolfe & Davis 1979; Wolfe, Briggs & Jauncey 1981). However, until the recent advent of new radio telescopes like the Giant Metrewave Radio Telescope (GMRT) and the Green Bank Telescope (GBT) with excellent low frequency coverage, only a few T_s estimates were available in high-z DLAs (e.g. Wolfe & Davis 1979; Wolfe et al. 1985; Carilli et al. 1996; de Bruyn, O'Dea & Baum 1996; Briggs, Brinks & Wolfe 1997; Kanekar & Chengalur 1997). Over the last decade, we have used the GBT, the GMRT and the Westerbork Synthesis Radio Telescope (WSRT) to carry out sensitive searches for redshifted H I 21 cm absorption in a large sample of DLAs at high redshifts, $z \gtrsim 2$. We have also used the Very Long Baseline Array (VLBA) to measure the low-frequency core fractions of the background quasars for most of the absorbers of the sample. Finally, we have obtained the metallicity, dust depletion and kinematic structure in the low-ionization metal lines for a significant fraction of the DLAs in our sample, either from our own observations or from the literature. In this paper, we report results from these studies and their implications for physical conditions in the neutral gas.[1]

2 OBSERVATIONS, DATA ANALYSIS AND SPECTRA

2.1 H I 21 cm absorption line searches

Our searches for redshifted H I 21 cm absorption were carried out with the GMRT, the GBT and the WSRT, targeting 26 DLAs at $0.68 < z < 3.42$. In addition, two known H I 21 cm absorbers were re-observed, to confirm earlier detections. The new targets were selected from the literature, mostly from the Complete Optical and Radio Absorption Line System (CORALS) sample of Ellison et al. (2001b), the UCSD sample of Jorgenson et al. (2006) and the SDSS. Five targets were observed with the GMRT, 22 with the GBT and one with the WSRT, all between 2003 and 2009.

2.1.1 GBT observations and data analysis

The GBT observations were carried out with the PF1-800, PF1-450 and PF1-342 receivers, in projects AGBT03A-015, AGBT05B-018, AGBT06B-042, AGBT08A-076 and AGBT09A-025. Most observations used the spectral processor (SP) as the backend, with two linear polarizations and bandwidths of 1.25, 2.5 or 5 MHz, sub-divided into 1024 channels. The SP was not available for the observations of two sources, 1122−168 and 0454+039; these were hence observed with the autocorrelation spectrometer, using two circular polarizations, a bandwidth of 50 MHz sub-divided into 16 384 channels and

nine-level sampling. All observations used position switching for bandpass calibration, with On and Off times of 5 min each, and data recorded every 5 or 10 s. A switching noise diode was used to measure system temperatures during all observations. Most runs also included observations of standard flux density calibrators like 3C286 or 3C48 to check the flux scale.

All GBT data were analysed in the AIPS++ single-dish package DISH, using standard procedures. All data were first visually inspected, both before and after calibration, and individual records affected by either radio frequency interference (RFI) or backend failures were edited out. For each target, the data were calibrated and the quasar flux density was measured in the centre of the band from the averaged spectrum. Some of the observations were affected by severe out-of-band RFI (although the receiver did not saturate), and the flux densities were found to vary dramatically from one record to another, typically yielding average flux densities very different from those in the literature and often also differing values in the two polarizations. In such cases, we chose to use flux densities from the literature, interpolating between measurements to obtain values at the respective redshifted H I 21 cm line frequencies. In general, the measured system temperatures (T_{sys}) were found to match expected values (except in the cases where the data were rendered unusable by extremely strong RFI), and the root-mean-square (rms) noise values on the spectra were close to the expected values, based on the T_{sys} estimates. After the flux density measurements, a second-order baseline was fitted to line- and RFI-free channels in each record during the process of calibration and the residual spectra were averaged together to obtain the H I 21 cm spectrum for each source. In some cases, a further first- or second-order baseline was fitted to the spectrum, again excluding line and RFI channels, to obtain the final H I 21 cm spectrum for each DLA. Finally, data on eight targets were rendered unusable by strong RFI at or near the redshifted H I 21 cm line frequencies.

2.1.2 GMRT and WSRT observations, and data analysis

The GMRT observations used the 327 MHz receivers and the 30-antenna hardware correlator, with two polarizations and a bandwidth of 1 MHz sub-divided into 128 channels, or 2 MHz sub-divided into 256 channels. The number of working antennas varied between 22 and 30 on the different runs, due to maintenance activities and technical problems. Observations of the standard calibrators 3C48, 3C147 and 3C286 were used to test the system performance at the beginning of each observing run, and then to calibrate the flux density scale. An observing run typically consisted of a full-synthesis track on the target source, interleaving 40 min scans on the target with 7 min scans on compact phase calibrators to calibrate the antenna gains. The system passband was calibrated with observations of bright radio sources, usually the flux density calibrators themselves, approximately every 3 h.

The WSRT observations of 0528−250 used the 92 cm receivers, with two DZB/IVC sub-bands of bandwidth 1.25 MHz each sub-divided into 512 channels, with two polarizations. The two intermediate-frequency DZB/IVC sub-bands were used in order to reduce the digital noise. The standard calibrators 3C48 and 3C286 were observed at the start and end of each run to calibrate the flux density scale and the system bandpass. A total of 50 h of observing time was obtained on the target source.

All GMRT and WSRT data were analysed in 'classic' AIPS, following standard procedures. After initial editing of bad data (e.g.

---

[1] When required, we will use the standard Λ cold dark matter cosmology, with $H_0 = 67.4 \, \text{km s}^{-1} \, \text{Mpc}^{-1}$, $\Omega_m = 0.315$ and $\Omega_\Lambda = 0.685$ (Planck Collaboration 2013).

due to malfunctioning antennas, shadowing, correlator problems, RFI, etc.), the antenna gains, passband shapes and amplitude scales were determined, using the data on the various calibrators. After applying the initial calibration, a number of channels were averaged together to obtain a 'channel-0' continuum visibility data set and a series of self-calibration and imaging cycles were then used to accurately determine the antenna gains. This was accompanied by intermediate flagging steps to further edit out bad data. For the GMRT, 3D imaging procedures were used for all 327 MHz data, with the field sub-divided into 37 facets during imaging. In the case of the WSRT, the low source elevation meant that additional care had to be taken to remove data affected by shadowing by foreground trees. The self-calibration and imaging procedure consisted of three to four phase-only calibration and imaging cycles, followed by a single amplitude-and-phase self-calibration and imaging step. This was followed by subtraction of the image from the calibrated visibilities, with the residual UV data then examined for any systematic behaviour and bad data edited out, after which the self-calibration and imaging cycles were repeated. This procedure was carried out for each source until no further improvement was obtained in the image and UV residuals, typically after two to three such cycles. The final image was then subtracted out from the calibrated multichannel UV visibility data set, using the task UVSUB. Following this, the task UVLIN was used to subtract out any residual emission, by a first-order polynomial fit to the spectrum on each visibility baseline. The residual UV data were then shifted to the heliocentric frame using the task CVEL, and were imaged to produce the final spectral cube. A spectrum was then obtained by taking a cut through the location of the target source. In some cases, a second-order baseline was fitted to this spectrum to obtain the final H I 21 cm spectrum of the source. Finally, the source flux density was measured by using the task JMFIT to fit a Gaussian model to the final continuum image; all target sources were unresolved by the WSRT and GMRT synthesized beams and a single Gaussian was hence used as the model in all cases.

In the case of the WSRT data, the extremely low elevation of 0528−250 meant that the flux density scale could not be determined accurately. We found that both the source flux density and the rms noise on the spectrum were lower by a factor of ≈1.71 than the expected values, indicating a multiplicative problem with the flux scale. Fortunately, this scaling issue does not affect the H I 21 cm optical depth spectrum. Note that the quoted flux density and rms noise values in Table 1 have been corrected by this factor of 1.71, for consistency with the literature.

Table 1. Summary of H I 21 cm observations.

| QSO	z_{QSO}	z_{DLA}	$\nu_{21\,cm}$ (MHz)	Telescope	Time (h)	BW (MHz)	Resn. (km s^{-1})	rms (mJy)	$S^a_{21\,cm}$ (Jy)	$\int \tau_{21} dV$ (km s^{-1})
0149+335	2.431	2.1408	452.24	GBT	2	2.5	3.2	RFI	–	–
0201+113	3.610	3.3869	323.78	GMRT	20	1.0	7.2	1.0	0.42	0.714 ± 0.017
0336−017	3.200	3.0621	349.67	GMRT	11	1.0	6.7	1.1	0.83	<0.07
0347−211	2.944	1.9470	481.98	GBT	2	1.25	1.5	16.8	0.94	<0.29
0405−331	2.570	2.5693	397.95	GBT	6	5, 1.25	1.8,7.4	2.5^b	1.0	<0.12
0432−440	2.649	2.3020	430.17	GBT	0.5	5.0	6.8	5.6	0.61	<0.22
0438−436	2.863	2.3474	424.33	GBT	1.5	1.25	1.7	10.4	7.1	0.216 ± 0.027
0405−443	3.020	1.9130	487.61	GBT	0.2	1.25	1.5	RFI	–	–
0454+039	1.350	0.8597	763.78	GBT	0.5	50	2.4	3.2	0.46	<0.15
0458−020	2.229	2.0395	467.32	GBT	1	0.625, 1.25	0.78,1.6	16.2	1.5	5.866 ± 0.059^c
0528−250	2.779	2.8112	372.69	WSRT	50	1.25	3.9	7.0^d	0.140^d	<1.3
0800+618	3.033	2.9603	358.66	GMRT	5	2.0	6.5	4.0	0.70	<0.19
0824+355	2.249	2.2433	437.95	GBT	2	1.25	1.7	9.6	2.6	<0.068
0913+003	3.074	2.7434	379.44	GBT	1	12.5	1.2	10.2	0.84	<0.18
0944+636	2.617	2.4960	406.29	GBT	2	2.5	3.6	RFI	–	–
1013+615	2.800	2.7670	377.07	GBT	4	2.5	3.9	8.1	1.00	<0.20
1122−168	2.397	0.6819	844.52	GBT	1.5	50.0	2.2	1.7	0.58	<0.059
1157+014	2.000	1.9436	482.47	GBT	2	0.625	0.76	14.2	0.70	1.020 ± 0.091
1215+333	2.610	1.9991	473.61	GBT	0.2	1.25	1.6	RFI	–	–
1230−101	2.394	1.9314	484.55	GBT	1	1.25	1.5	RFI	–	–
1354−170	3.150	2.7799	375.78	GBT	2.5	2.5	3.9	8.7	2.6	<0.10
1402+044	3.215	2.7076	383.11	GBT	1.5	2.5	3.8	11.5	1.1	<0.21
1418−064	3.689	3.4483	319.31	GMRT	11	1.0	7.3	1.3	0.44	<0.10
1614+051	3.215	2.5200	403.52	GBT	3	2.5	3.6	16	1.1	<0.30
1645+635	2.380	2.1253	454.49	GBT	0.5	1.25	1.6	RFI	–	–
1755+578	2.110	1.9698	478.28	GBT	1	1.25	1.5	RFI	–	–
1850+402	2.120	1.9888	475.24	GBT	1	1.25	1.5	RFI	–	–
2342+342	3.053	2.9082	363.44	GMRT	10	1.0	6.4	1.4	0.29	<0.22

$^a S_{21\,cm}$ is the source flux density at the redshifted H I 21 cm line frequency.
^{b}The quoted rms noise is on the final H I 21 cm spectrum, produced by smoothing the two spectra to the same velocity resolution and then averaging with weights based on the rms noise values.
^{c}The quoted integrated H I 21 cm optical depth for the $z = 2.0395$ DLA towards 0458−020 is the average of the values obtained in the two observing runs in 2008 March and May, while the rms noise is at a resolution of 2.4 kHz, averaging over the two runs. See Section 5 for details.
^{d}The low elevation of 0528−250 during the WSRT observations resulted in a multiplicative error by a factor of 1.71 in the flux density scale. The measured flux density and rms noise were 82 mJy and 4.1 mJy, respectively; however, the quoted values in the table are on the flux scale of Carilli et al. (1996). Note that the flux scale has no effect on the inferred optical depth.
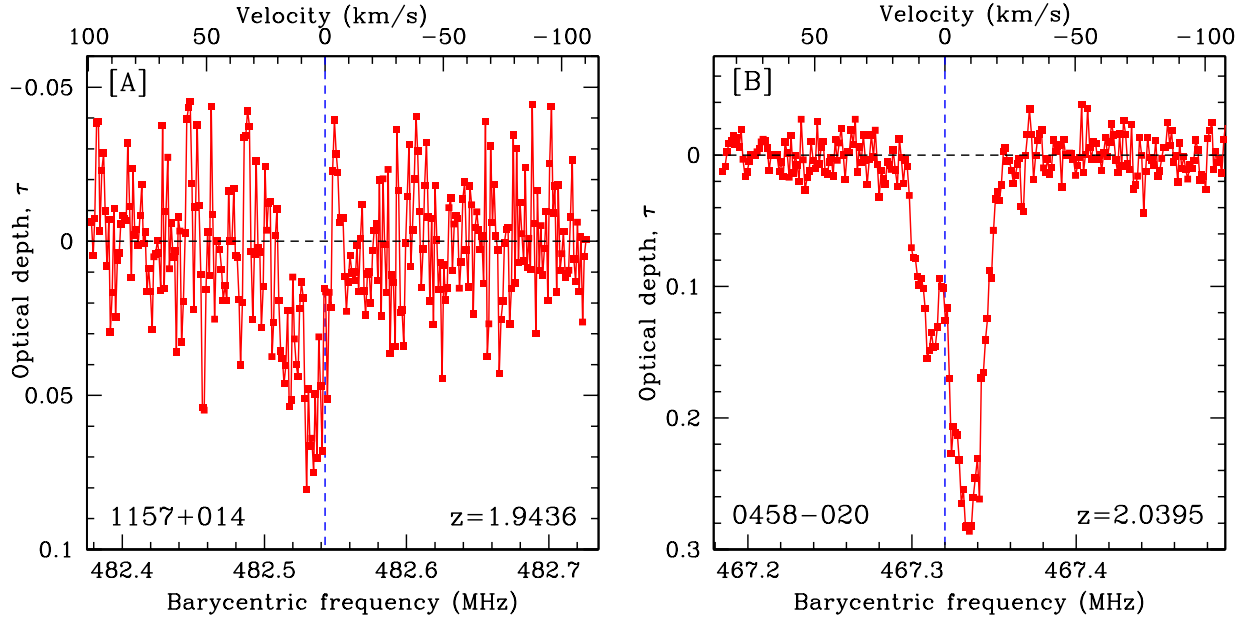
Figure 1. Detections of H I 21 cm absorption in two known H I 21 cm absorbers, [A] at $z = 1.9436$ towards 1157+014 and [B] $z = 2.0395$ towards 0458−020, with H I 21 cm optical depth plotted against the barycentric frequency, in MHz. The top axis in each panel shows velocity (in km s^{-1}), relative to the DLA redshift. See the main text for discussion.

2.1.3 Spectra and results

New detections of H I 21 cm absorption were obtained in two DLAs, at $z \sim 3.387$ towards 0201+113 and $z \sim 2.347$ towards 0438−436. These results were discussed in detail by Kanekar et al. ([2006](#)) and Kanekar, Chengalur & Lane ([2007](#)), and the spectra are not shown here. H I 21 cm absorption was also detected in two known H I 21 cm absorbers, at $z \sim 1.9436$ towards 1157+014 (Wolfe et al. [1981](#)) and $z = 2.0395$ towards 0458−020 (Wolfe et al. [1985](#)); these spectra are shown in Fig. [1](#). For the non-detections, the final H I 21 cm spectra are shown in Fig. [2](#), in order of increasing right ascension.

The observational details and results of the GBT, GMRT and WSRT spectroscopy are summarized in Table [1](#). The columns of this table show (1) the quasar name, (2) the quasar emission redshift, (3) the DLA redshift, (4) the redshifted H I 21 cm line frequency, (5) the telescope used for the H I 21 cm search, (6) the on-source integration time, in hours, (7) the bandwidth, in MHz, (8) the velocity resolution, in km s^{-1}, after Hanning smoothing and re-sampling, (9) the rms noise at this velocity resolution, in mJy, (10) the source flux density, in Jy and (11) for detections, the integrated H I 21 cm optical depth $\int \tau_{21\,cm}\, dV$, or, for non-detections, the 3σ limit on $\int \tau_{21\,cm}\, dV$, assuming a Gaussian line profile with a line full width at half-maximum (FWHM) of $\Delta V = 15\,km\,s^{-1}$, with the rms noise computed at a similar velocity resolution. For the eight GBT targets where the final H I 21 cm spectrum was unusable due to RFI, column (10) contains 'RFI', and the remaining column entries have been left blank. We note, in passing, that the assumed line FWHM of 15 km s^{-1} is comparable to the widths of spectral components in known redshifted H I 21 cm absorbers; assuming a narrower line FWHM would yield a more stringent lower limit on the spin temperature (see Section 3 for discussion).

2.2 VLBA imaging studies

We used the VLBA 327 MHz, 606 MHz and 1.4 GHz receivers in proposals BK89, BK131, BK153, BK159 and BK175 to obtain high-spatial-resolution images of the compact radio structure of the quasars behind a sample of DLAs and H I 21 cm absorbers, to measure the quasar core fractions, and thus estimate the DLA covering factors. For each target, the VLBA observing frequency was chosen to be within a factor of ≈ 2 of the redshifted H I 21 cm line frequency, to ensure that the spatial extent of the background radio continuum was determined close to the line frequency. In practice, the VLBA observing frequency was within a factor of 1.5 of the redshifted H I 21 cm line frequency for all targets except for three H I 21 cm absorbers at $z \sim 1.3$ lying towards faint background quasars (J0850+5159, J0852+3435 and 2337−011, all with flux densities $\lesssim 100$ mJy at the redshifted H I 21 cm line frequency). These three sources were observed with the higher sensitivity L-band receivers of the VLBA.

The results from the initial VLBA data of proposals BK89 and BK131 were presented by Kanekar et al. ([2009a](#)). We will not describe these data again here, but will instead simply use the core flux density estimates from that paper. 13 DLAs and H I 21 cm absorbers were observed with the VLBA in proposals BK153, BK159 and BK175, six with the 327 MHz receivers, three with the 606 MHz receivers and four with the 1.4 GHz receivers. Bandwidths of 12, 4 and 32 MHz were used at 327 MHz, 606 MHz and 1.4 GHz, respectively, sub-divided into 32 spectral channels and with two polarizations and two-bit sampling. The on-source time was ≈ 2 h for each source. One or more of the strong fringe finders 0438−436, 3C454.3, 3C84, 3C147, 3C286 and 3C345 were observed during each run for bandpass calibration; phase referencing was not used.

The VLBA data were also reduced in 'classic' AIPS, following procedures similar to those described in Section 2.1.2. However, for the VLBA data, the flux density scale was calibrated by using online measurements of the antenna gains and system temperatures, and the calibration steps included ionospheric corrections and fringe fitting to determine the delay rates. Unfortunately, the ionospheric phase stability was relatively poor during the 327 and 606 MHz observations and only five to six antennas could be retained during
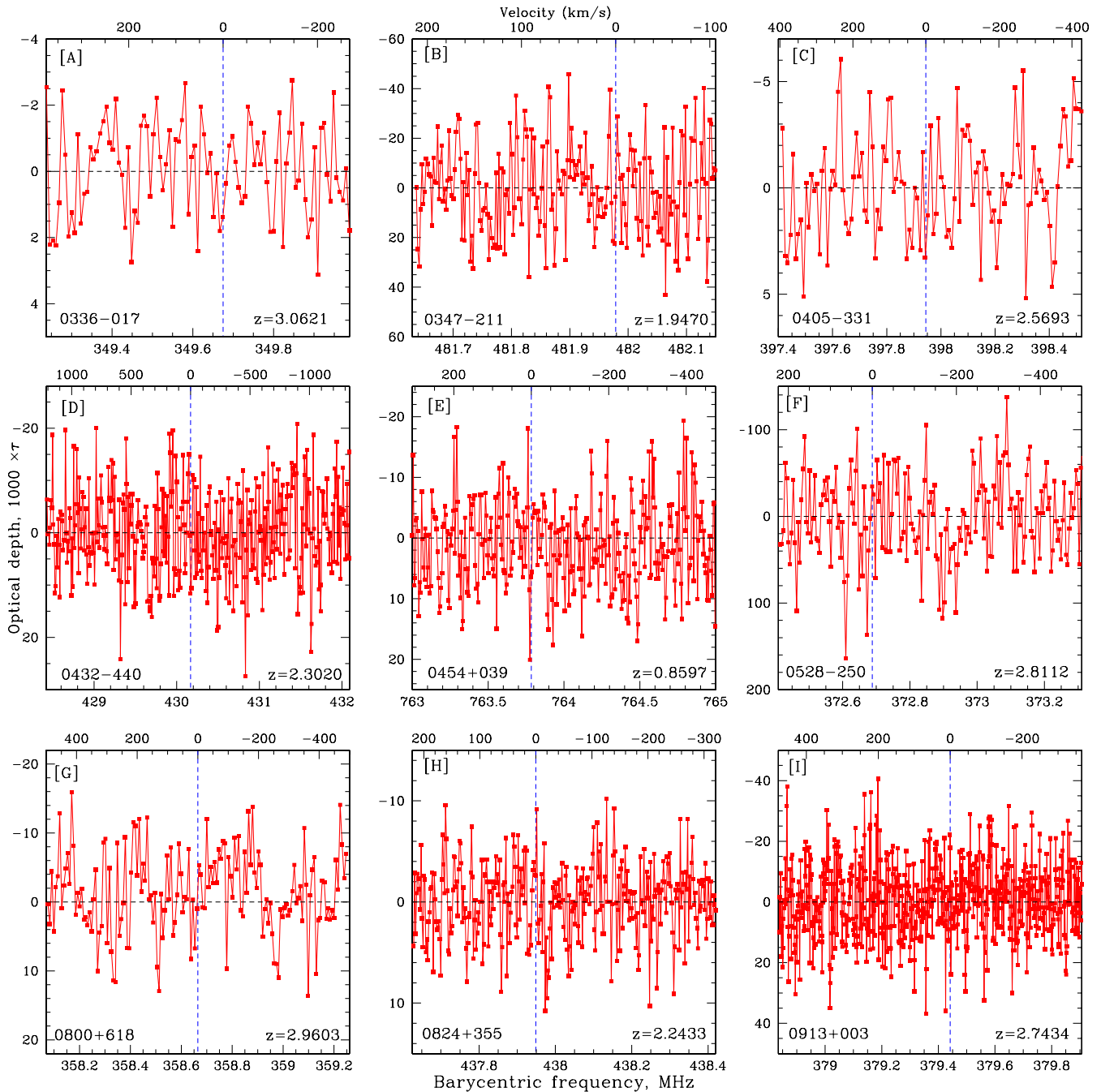
Figure 2. The 16 non-detections of H I 21 cm absorption, in order of increasing right ascension, with optical depth ($10^3 \times \tau$) plotted against barycentric frequency, in MHz. The top axis in each panel shows velocity (in km s^{-1}), relative to the DLA redshift, while the expected H I 21 cm line frequency, from the optically determined redshift, is indicated by the dashed line in each panel. The panels contain spectra for [A] the $z = 3.0621$ DLA towards 0336−017, [B] the $z = 1.9470$ DLA towards 0347−211, [C] the $z = 2.5693$ DLA towards 0405−311, [D] the $z = 2.3020$ DLA towards 0432−440, [E] the $z = 0.8597$ DLA towards 0454+039, [F] the $z = 2.8112$ DLA towards 0528−250, [G] the $z = 2.9603$ DLA towards 0800+618, [H] the $z = 2.2433$ DLA towards 0824+355, [I] the $z = 2.7434$ DLA towards 0913+003, [J] the $z = 2.7670$ DLA towards 1013+615, [K] the $z = 0.6819$ DLA towards 1122−168, [L] the $z = 2.7799$ DLA towards 1354−170, [M] the $z = 2.7076$ DLA towards 1402+044, [N] the $z = 3.4483$ DLA towards 1418−064, [O] the $z = 2.5200$ DLA towards 1614+051 and [P] the $z = 2.9082$ DLA towards 2342+342. The dashed vertical line marks the expected redshifted H I 21 cm frequency. The shaded vertical region in panel [L] (for 1354−170) indicates a frequency range affected by RFI.

the self-calibration procedure. Further, the final VLBA images were produced with phase self-calibration alone, again after the usual iterative procedure involving a number of self-calibration and imaging cycles. The core flux density of each source was measured using the task JMFIT, by fitting an elliptical Gaussian model to the core

radio emission. The core emission was found to be fairly compact in most cases, with little extended emission; a single Gaussian was hence used as the model for most sources. For three sources, adding more source components yielded a clear decrease in the χ^2 and thus an appreciably better fit: a two-component model was hence used
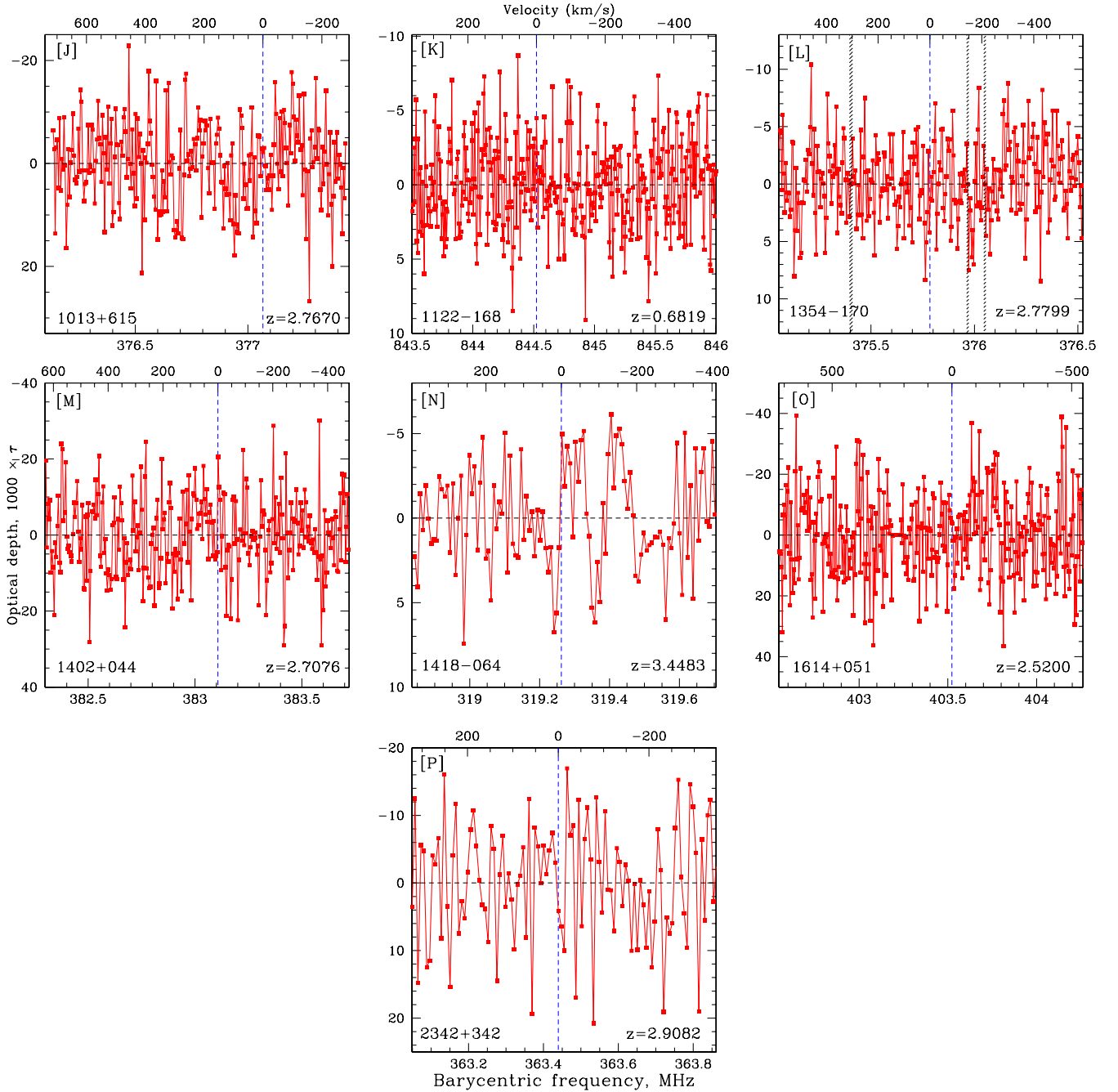
Figure 2 – *continued*

for two of these, 2003−025 and 1122−168, and a three-component model for 0824+355.

The VLBA images are presented in Fig. 3, in order of increasing right ascension, with the results summarized in Table 2. The columns of this table contain (1) the quasar name, (2) the quasar emission redshift, (3) the DLA redshift, (4) the redshifted H I 21 cm line frequency, in MHz, (5) the VLBA observing frequency ν_{VLBA}, in MHz, (6) the total source flux density S_{tot} at the VLBA observing frequency, obtained from single-dish or low-resolution interferometer studies, (7) the VLBA beam, in mas × mas, (8) the core flux density S_{VLBA}, in Jy, measured from the VLBA image (for the three sources with multiple Gaussian components, the most com-

pact component was identified as the core), (9) the deconvolved size of the radio emission, in mas × mas, (10) the spatial extent of the core radio emission at the DLA redshift and (11) the DLA covering factor f, assumed to be equal to the quasar core fraction, i.e. the ratio of the core flux density measured in the VLBA image S_{VLBA} to the total source flux density S_{tot} at the VLBA frequency (see Section 3). For systems without measurements of the total flux density at the VLBA observing frequency, S_{tot} was estimated by extrapolating from measurements at other frequencies. It should be emphasized that the estimates of the deconvolved size of the core emission and its spatial extent are upper limits, because any residual phase errors would increase the apparent size of the core emission. Finally, we
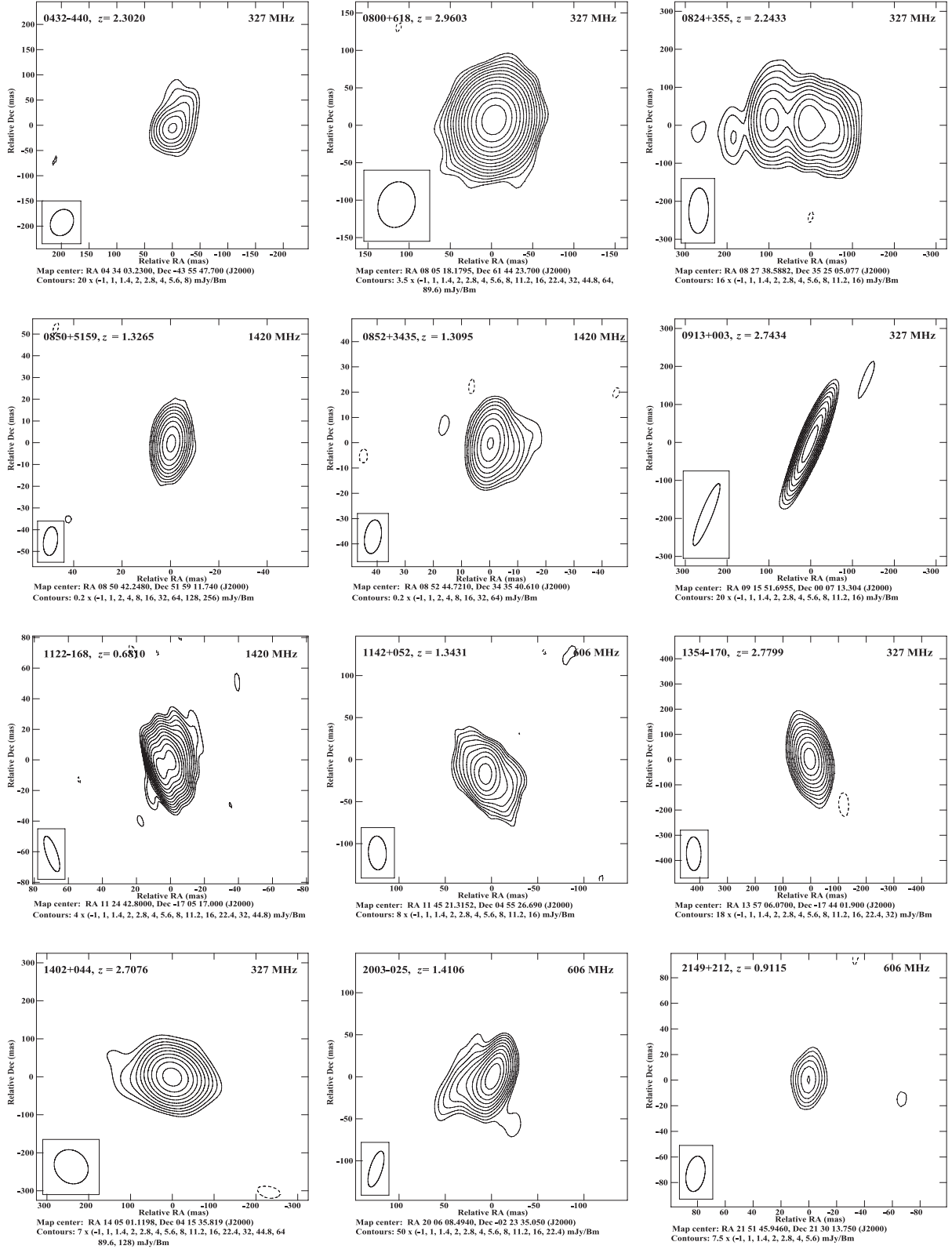
Figure 3. VLBA images of the compact radio structure of the 13 background quasars; the quasar name, DLA redshift and observing frequency are indicated at the top of each panel. The dashed contour shows the largest negative value in each image, with the outermost positive contour at the same level; the penultimate solid contour thus indicates the lowest believable structure in each image. The synthesized beam is shown at the bottom-left corner of each panel.
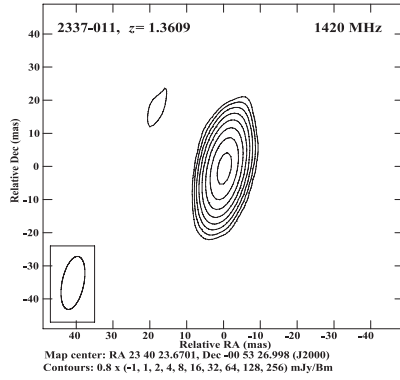
Figure 3 – *continued*

note that error bars have not been included in the covering factor estimates. While we estimate that the errors on the VLBA flux density calibration are ≈10 per cent, the VLBA and total flux density measurements were not carried out simultaneously, implying that individual covering factor estimates could have larger errors due to source variability.

2.3 Optical spectroscopy

2.3.1 VLT-UVES spectroscopy

Very Large Telescope Ultraviolet Echelle Spectrograph (VLT-UVES) data were obtained as part of the programme 67.A-0567(A) (PI: Lane) for 1127−145 in 2001 May/June. Five 3060 s exposures were obtained with both UVES arms in the 346+580 nm standard wavelength setting, with a 1.0 arcsec slit.

Besides the above UVES observations, we also downloaded UVES data on a few DLAs of the sample from the VLT archive, along with the requisite calibration files obtained within a few nights of the science exposures. The instrumental calibration plan dictates how frequently the calibration exposures are obtained, based on knowledge of the instrument stability. The blue arm data downloaded by us on 0952+179 as part of programme 69.A-0371(A) (PI: Savaglio) consist of three 5700 s exposures with the 346 nm central wavelength setting. Data for 0827+243 were obtained as part of programme 68.A-0170(A) (PI: Mallen-Ornelas) with both UVES arms in the 346+564 standard settings and four 1 h exposures. In all cases, the data were obtained with a 1.0 arcsec slit, with the detector binned by 2 in both the spatial and spectral directions.

Table 2. Results from VLBA low-frequency imaging of quasars behind high-z DLAs.

QSO	z_{QSO}	z_{abs}	$\nu_{21\,cm}$ (MHz)	ν_{VLBA} (MHz)	S_{tot}^a (Jy)	Beam (mas × mas)	S_{fit} (Jy)	Angular size (mas × mas)	Spatial extent (pc × pc)	f^c
0432−440	2.649	2.3020	430.17	327	0.69	54 × 40	0.26	$58.2^{+2.5}_{-2.5} \times 24.4^{+2.1}_{-2.3}$	$490^{+21}_{-21} \times 205^{+18}_{-19}$	0.38
0800+618	3.033	2.9603	358.66	327	0.70	61 × 45	0.44	$13.5^{+0.8}_{-0.8} \times 10.3^{+0.6}_{-0.8}$	$107^{+6}_{-6} \times 82^{+5}_{-6}$	0.63
0824+355	2.249	2.2433	437.95	327	2.00	119 × 47	0.40	$27.8^{+6.2}_{-27.8} \times 2.4^{+0.8}_{-2.4}$	$235^{+52}_{-235} \times 20^{+7}_{-20}$	0.20
							0.37	$66.2^{+9.2}_{-9.6} \times 41.1^{+9.9}_{-15.6}$	$560^{+78}_{-81} \times 348^{+84}_{-132}$	–
							0.36	$79.2^{+9.4}_{-9.7} \times 51.7^{+3.4}_{-5.1}$	$670^{+79}_{-82} \times 437^{+29}_{-43}$	–
J0850+5159	1.894	1.3265	610.53	1420	0.061	13.3 × 5.8	0.069	$1.49^{+0.04}_{-0.03} \times 0.95^{+0.17}_{-0.21}$	$12.9^{+0.3}_{-0.3} \times 8.0^{+1.5}_{-1.8}$	1.0
J0852+3435	1.655	1.3095	615.03	1420	0.066	13.4 × 5.9	0.062	$2.9^{+0.03}_{-0.03} \times 0.89^{+0.25}_{-0.35}$	$25.0^{+0.3}_{-0.3} \times 7.7^{+2.2}_{-3.0}$	0.93
0913+003	3.074	2.7434	379.44	327	0.48	173 × 27	0.26	$16.6^{+17.4}_{-9.3} \times 7.6^{+2.2}_{-7.6}$	$134^{+141}_{-75} \times 62^{+18}_{-62}$	0.54
1122−168	2.397	0.6819	844.52	1420	0.29	24.1 × 6.5	0.012	$4.2^{+1.5}_{-2.4} \times 0.0^{+0.0\ b}_{-0.0}$	$30.7^{+11.0}_{-17.5} \times 0.0^{+0.0\ b}_{-0.0}$	0.04
							0.043	$12.5^{+0.4}_{-0.3} \times 5.7^{+0.9}_{-1.0}$	$91.3^{+2.9}_{-2.2} \times 41.6^{+6.6}_{-7.3}$	–
1142+052	1.345	1.3431	606.21	606	1.01	40 × 19	0.30	$36.6^{+1.6}_{-1.6} \times 19.1^{+1.8}_{-2.1}$	$317^{+14}_{-14} \times 165^{+16}_{-18}$	0.30
1354−170	3.150	2.7799	375.78	327	0.83	134 × 53	0.81	$88.3^{+1.8}_{-1.8} \times 38.6^{+2.0}_{-2.1}$	$712^{+15}_{-15} \times 311^{+16}_{-17}$	0.97
1402+044	3.215	2.7076	383.11	327	1.26	93 × 78	0.43	$44.5^{+6.5}_{-7.3} \times 23.4^{+10.6}_{-23.4}$	$362^{+53}_{-59} \times 190^{+86}_{-190}$	0.34
2003−025	1.457	1.4106	589.23	606	3.7	44 × 13	1.97	$14.9^{+0.6}_{-0.5} \times 11.0^{+1.1}_{-1.3}$	$129^{+5}_{-4} \times 95^{+10}_{-11}$	0.53
							1.48	$48.5^{+2.1}_{-2.1} \times 31.2^{+3.2}_{-3.4}$	$421^{+18}_{-18} \times 271^{+28}_{-30}$	–
2149+212	1.538	0.9115	743.08	606	1.92	28 × 13	0.05	$13.3^{+4.2}_{-13.3} \times 7.1^{+5.5}_{-7.1}$	$107^{+34}_{-107} \times 57^{+44}_{-57}$	0.03
2337−011	2.085	1.3606	601.71	1420	0.12	16.2 × 5.9	0.13	$1.5^{+0.2}_{-0.3} \times 0.60^{+0.19}_{-0.60}$	$13.0^{+1.7}_{-2.6} \times 5.2^{+1.6}_{-5.2}$	1.0

^{a}The total flux density S_{tot} at the VLBA observing frequency was estimated by extrapolating from measured values in the literature, usually from the 365 MHz Texas survey (Douglas et al. 1996) and the 1.4 GHz Very Large Array FIRST and NVSS surveys (Becker, White & Helfand 1995; Condon et al. 1998).

^{b}For 1122−168, the deconvolved angular size and spatial extent are both 0.0 along one axis. This is because the angular extent of the core along this axis is significantly smaller than the VLBA synthesized beam.

^{c}We assume that the DLA covering factor f is equal to the quasar core fraction, i.e. the ratio of the core flux density to the total integrated flux density, S_{tot}. For the three sources, 1122−168, 0824+355 and 2003−025, where the model contained multiple Gaussian components, the more compact component has been identified with the core. In such cases, the covering factor estimates assume that only the core has been covered by the foreground DLA.

The UVES data of 1127−145 were reduced with the UVES MIDAS pipeline version 2.1.0,[2] while the archival UVES data were reduced using a custom version of the UVES pipeline, based on MIDAS reduction routines. All data reduction followed the standard procedure for UVES data (e.g. Ellison, Ryan & Prochaska 2001a), with wavelength calibration and normalization carried out for the individual spectra, before the spectra were optimally combined to produce the final one-dimensional spectrum on a heliocentric wavelength scale.

2.3.2 HST-STIS spectroscopy of 1127−145

The Space Telescope Imaging Spectrograph (STIS) on the *Hubble Space Telescope* (*HST*) was used in the E230M echelle mode in proposal 9173 (PI: Bechtold) to obtain a UV spectrum of 1127−145. These data were downloaded from the *HST* archive. The total exposure time on target amounted to 52 380 s with the 0.2 arcsec × 0.2 arcsec aperture. The *HST*-STIS data were reduced with the IDL version of CalSTIS v7.0 (Lindler 1999), following standard procedures, combining data from different exposures with weights inversely proportional to their variance.

2.3.3 GMOS observations of 0311+430

The $z = 2.2890$ DLA towards 0311+430 (York et al. 2007) was observed on 2007 November 14 with the Gemini Multi-Object Spectrograph (GMOS) on the Gemini North telescope (in proposal GN-2007B-Q-76). The quasar was observed in nod and shuffle mode with the R600 grating, a central wavelength of 800 nm and a 0.75 arcsec slit. The CCD was binned by two pixels in both the spatial and spectral directions. In nod and shuffle mode, the target is observed at two spatial positions on the slit in an ABBA configuration. The exposure time at each position was 30 s (120 s cycle^{-1}) with 19 cycles per exposure. Each exposure therefore has an effective integration time of 2280 s, with six exposures taken in all.

The data were reduced using the Gemini IRAF package following standard procedures, but with special modifications for the nod and shuffle mode. First, a bias was constructed, with an interactive fit to the overscan region, using GBIAS. A dark calibration frame was constructed using GNSDARK and subtracting the bias frame from the previous step. GSFLAT was used to make the master flat-field from individual lamp exposures with interactive polynomial fits to remove the underlying spectral shape of the illumination. The application of these calibration frames (bias, dark and flat) to the science data was achieved using GSREDUCE. Sky subtraction is done using GNSSKYSUB on the two-dimensional (2D) spectra by subtracting the shuffled image pixels from those in the unshuffled position. This step in the procedure is one of the great benefits of the nod and shuffle mode, and results in superior subtraction with much lower sky residuals than traditional long-slit spectroscopy. For our reductions, with multiple exposures, GNSSKYSUB is called as part of the GNSCOMBINE routine which applies offsets to the various dithers and yields a single 2D spectrum. After the combination, the 2D frame has a positive and a negative spectrum at position A and B, respectively. A first-order wavelength correction (based on the image header information) of the science image and mosaicking of the three CCDs are achieved by running GSREDUCE again. GSREDUCE is also used to apply the master calibration

files to the arc frames, before the wavelength solution is determined and applied to the science frame using GSWAVELENGTH and GSTRANSFORM, respectively. The 1D spectra (one positive and one negative) were then extracted using GSEXTRACT and averaged together after inversion of the negative spectrum. The final spectrum (obtained after binning by 2 in both spatial and spectral directions) has a wavelength coverage of 6570–9450 Å, an FWHM resolution of ∼3.1 Å and a signal-to-noise ratio (S/N) per pixel of 30–50.

2.3.4 Keck-HIRES spectroscopy

The $z = 0.0912$ and 0.2212 DLAs towards 0738+313 were observed on 2006 December 26 with the High-Resolution Echelle Spectrograph (HIRES) on the W. M. Keck telescope (Vogt et al. 1994), configured with the blue cross-dispersor (i.e. HIRESb). We employed the E3 decker which affords a spectral resolution of FWHM ≈4 km s^{-1}. The grating was tilted to XDANGL = 1.039 giving a nearly continuous wavelength coverage from $\lambda \approx 3100$ to 5900 Å, but with two gaps owing to the CCD mosaic. The science frames (two exposures at 900 s each) and associated calibration files were reduced with the HIRedux data reduction pipeline[3] (for details, see Prochaska et al. 2007). The spectra were optimally extracted and co-added (binning by 2 in the spatial direction), corrected to vacuum wavelengths and the heliocentric reference frame. The S/N at $\lambda \approx 4000$ Å is approximately 13 per 1.3 km s^{-1} pixel.

2.3.5 Abundances and velocity widths

The Keck-HIRES, VLT-UVES, GMOS-N and *HST*-STIS spectra were used to derive column densities and elemental abundances for six DLAs, at $z = 0.0912$ and 0.2212 towards 0738+313, $z = 0.2378$ towards 0952+179, $z = 0.3127$ towards 1127−145, $z = 0.5247$ towards 0827+243 and $z = 2.2890$ towards 0311+430. For all absorbers, the column densities for different species were estimated from the observed line profiles using the apparent optical depth method (AODM; Savage & Sembach 1991).

For the $z = 0.3127$ DLA towards 1127−145, the weakness of the Zn II lines in the *HST*-STIS spectrum prompted us to also try a different route. Here, the strong absorption lines in the VLT-UVES spectrum were first analysed with FITLYMAN (Fontana & Ballester 1995), with Voigt profiles first fitted to the Ca II doublets alone, in order to determine the turbulent Doppler parameters and the redshifts of the individual components. These values were then fixed, together with the column density of the individual Ca II doublets, and the Zn II and Mn II lines included in the fit to determine the Zn II column density from the *HST*-STIS spectrum and the Mn II column density from the VLT-UVES spectrum. This approach yielded $\log[N_{\mathrm{Zn\,II}}/\mathrm{cm}^{-2}] = 13.45 \pm 0.08$, consistent with the AODM value of $\log[N_{\mathrm{Zn\,II}}/\mathrm{cm}^{-2}] = 13.57 \pm 0.05$; the AODM value will be used in the following discussion, as it involves fewer assumptions. We note, in passing, that the Voigt profile fit to the Mg I line yielded a larger Mg I column density than that obtained from the AODM, with $\log[N_{\mathrm{Mg\,I}}/\mathrm{cm}^{-2}] = 13.95 \pm 0.07$. This may be because the Mg I line is nearly saturated in this absorber; in such situations, the AODM estimate should be regarded as a lower limit

Table 3 lists the column densities derived for various species in the six DLAs, along with the H I column density of the absorber. The abundances, relative to the solar abundance, on the solar scale of

Table 3. Ionic column densities.

Ion	λ (Å)	$\log f$	$\log [N_0/\mathrm{cm}^{-2}]^a$	$\log [N/\mathrm{cm}^{-2}]^a$
(1) 0738+313, $z = 0.0912$, HIRES, $\log[N_{\mathrm{H\,I}}/\mathrm{cm}^{-2}] = 21.18 \pm 0.06$				
Mg I				
	2852.964	0.2577	>12.98	>12.98
Ca II				
	3934.777	−0.1871	12.28 ± 0.03	12.26 ± 0.03
	3969.591	−0.4921	12.18 ± 0.08	
Ti II				
	3230.131	−1.1630	<12.74	12.51 ± 0.04
	3384.740	−0.4461	12.51 ± 0.04	
(2) 0738+313, $z = 0.2212$, HIRES, $\log[N_{\mathrm{H\,I}}/\mathrm{cm}^{-2}] = 20.90 \pm 0.07$				
Mg I				
	2852.964	0.2577	>12.46	>12.46
Mg II				
	2796.352	−0.2130	>13.49	>13.75
	2803.531	−0.5151	>13.75	
Ca II				
	3934.777	−0.1871	11.86 ± 0.07	11.92 ± 0.06
	3969.591	−0.4921	12.12 ± 0.09	
Ti II				
	3230.131	−1.1630	<12.58	<11.91
	3384.740	−0.4461	<11.91	
Fe II				
	2586.650	−1.1605	>14.30	>14.30
	2600.173	−0.6216	>13.82	
(3) 0952+179, $z = 0.2378$, UVES, $\log[N_{\mathrm{H\,I}}/\mathrm{cm}^{-2}] = 21.32 \pm 0.05$				
Mg I				
	2852.964	0.2577	12.68 ± 0.03	12.68 ± 0.03
Mg II				
	2796.352	−0.2130	>13.87	>14.13
	2803.531	−0.5151	>14.13	
Ti II				
	3073.877	−0.9622	12.62 ± 0.03	12.62 ± 0.03
Mn II				
	2576.877	−0.4549	12.50 ± 0.03	12.58 ± 0.03
	2594.499	−0.5670	12.67 ± 0.03	
Fe II				
	2586.650	−1.1605	14.52 ± 0.03^b	14.52 ± 0.03
	2600.173	−0.6216	>14.09	
(4) 1127−145, $z = 0.3127$, UVES+STIS, $\log[N_{\mathrm{H\,I}}/\mathrm{cm}^{-2}] = 21.70 \pm 0.08$				
Mg I				
	2852.964	0.2577	13.19 ± 0.03	13.19 ± 0.03^b
Mg II				
	2796.352	−0.2130	>14.07	>14.35
	2803.531	−0.5151	>14.35	
Ca II				
	3934.777	−0.1871	12.69 ± 0.03	12.70 ± 0.03
	3969.591	−0.4921	12.73 ± 0.03	
Mn II				
	2576.877	−0.4549	13.30 ± 0.03	13.26 ± 0.03
	2594.499	−0.5670	13.20 ± 0.03	
	2606.462	−0.7151	13.23 ± 0.03	
Fe II				
	2344.214	−0.9431	>14.71	>15.16
	2374.461	−1.5045	>15.16	
	2382.765	−0.4949	>14.32	
	2586.650	−1.1605	>14.92	
	2600.173	−0.6216	>14.43	
Zn II				
	2026.136	−0.3107	13.57 ± 0.05	13.57 ± 0.05

Table 3 – *continued*

Ion	λ (Å)	$\log f$	$\log [N_0/\mathrm{cm}^{-2}]^a$	$\log [N/\mathrm{cm}^{-2}]^a$
(5) 0827+243, $z = 0.5247$, UVES, $\log[N_{\mathrm{H\,I}}/\mathrm{cm}^{-2}] = 20.30 \pm 0.04$				
Ca II				
	3934.777	−0.1871	12.59 ± 0.03	12.59 ± 0.03
	3969.591	−0.4921	12.60 ± 0.03	
Ti II				
	3073.877	−0.9622	<11.86	11.82 ± 0.04
	3230.131	−1.1630	<11.97	
	3242.929	−0.6345	11.55 ± 0.12	
	3384.740	−0.4461	11.92 ± 0.04	
Fe II				
	2249.877	−2.7397	14.79 ± 0.05	14.84 ± 0.03
	2260.781	−2.6126	14.96 ± 0.03	
	2344.214	−0.9431	>14.66	
	2374.461	−1.5045	14.84 ± 0.03	
	2382.765	−0.4949	>14.43	
(6) 0311+430, $z = 2.2890$, GMOS, $\log[N_{\mathrm{H\,I}}/\mathrm{cm}^{-2}] = 20.30 \pm 0.11$				
Zn II				
	2026.136	−0.3107	<12.5	<12.5
Cr II				
	2056.254	−0.9788	<13.05	<13.05
Mn II				
	2594.499	−0.5670	12.37 ± 0.11	12.50 ± 0.07
	2606.462	−0.7151	12.63 ± 0.09	
Fe II				
	2249.877	−2.7397	14.80 ± 0.10	14.86 ± 0.06
	2260.781	−2.6126	14.91 ± 0.05	
	2374.461	−1.5045	>14.32	

^{a}The column densities measured from individual transitions are listed in the penultimate column ($\log [N_0/\mathrm{cm}^{-2}]$), while the adopted column density for the species is listed in the final column ($\log [N/\mathrm{cm}^{-2}]$). The adopted column density of a given species was obtained by a weighted mean of the measured column densities from all unsaturated line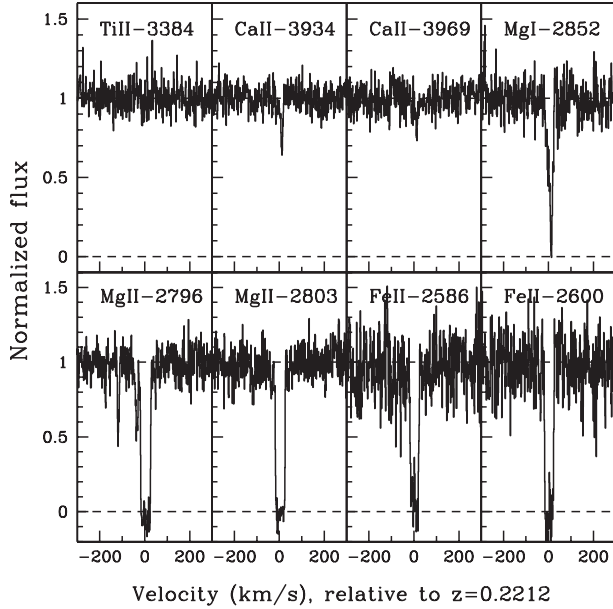s. All limits are at 3σ significance. ^{b}Note that the Fe II $\lambda 2586$ line in the $z = 0.2378$ DLA towards 0952+179 and the Mg I line in the $z = 0.3127$ DLA towards 1127−145 are both close to saturation. If the lines are saturated, the quoted column densities would be lower limits.

Asplund et al. (2009) are summarized for each system in Section 5. The metal lines detected in each spectrum (and, in some cases, a few undetected transitions) are plotted in Figs 4–9.

Finally, we measured the velocity width at 90 per cent optical depth, ΔV_{90}, of the low-ionization metal lines detected in our Keck-HIRES or VLT-UVES spectra of a sub-set of the absorbers of our sample following the criteria and procedures described in Prochaska & Wolfe (1997). In the majority of cases, we analysed an unsaturated, low-ion transition observed at high S/N. For ≈5 systems, however, this did not prove possible (e.g. the DLA at $z = 0.2212$ towards 0738+313). In these cases, we measured ΔV_{90} from a modestly saturated line or a transition from a non-dominant ion (e.g. Mg I $\lambda 2852$). Inspection of the full set of line profiles for these systems indicates that the results should be representative of the gas kinematics. The derived ΔV_{90} values are listed in Table 4, along with the transition used for the estimate.
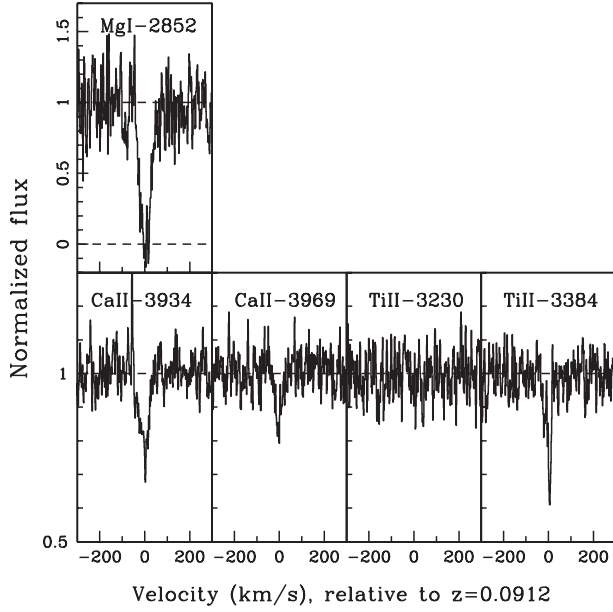
Figure 4. Low-ionization metal absorption profiles from the $z = 0.0912$ DLA towards 0738+313, from the Keck-HIRES spectrum. The *x*-axis represents velocity, in km s^{-1}, relative to the DLA redshift.
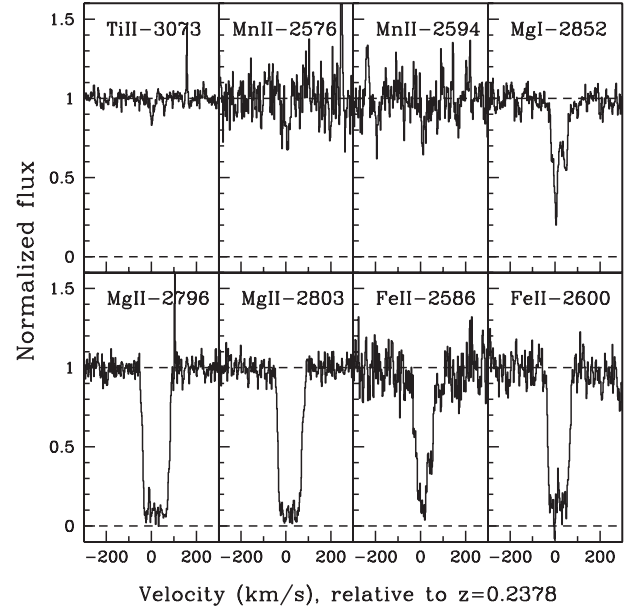

Figure 6. Low-ionization metal absorption profiles from the $z = 0.2378$ DLA towards 0952+179, from the VLT-UVES spectrum. The *x*-axis contains velocity, in km s^{-1}, relative to the DLA redshift.
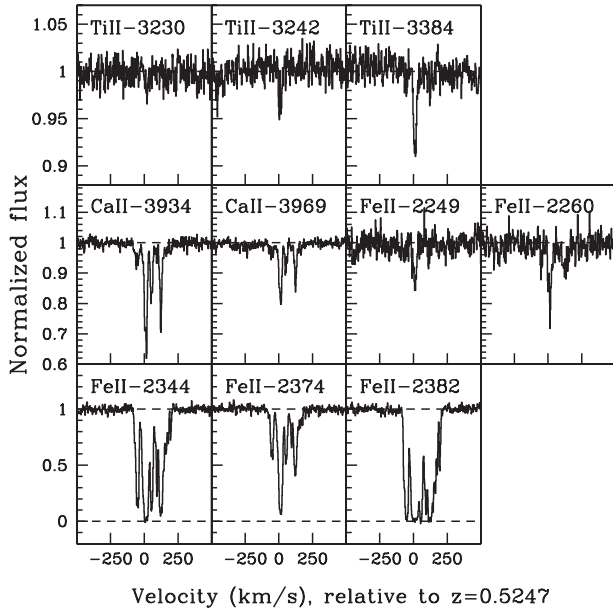

Figure 5. Low-ionization metal absorption profiles from the $z = 0.2212$ DLA towards 0738+313, from the Keck-HIRES spectrum. The *x*-axis contains velocity, in km s^{-1}, relative to the DLA redshift.
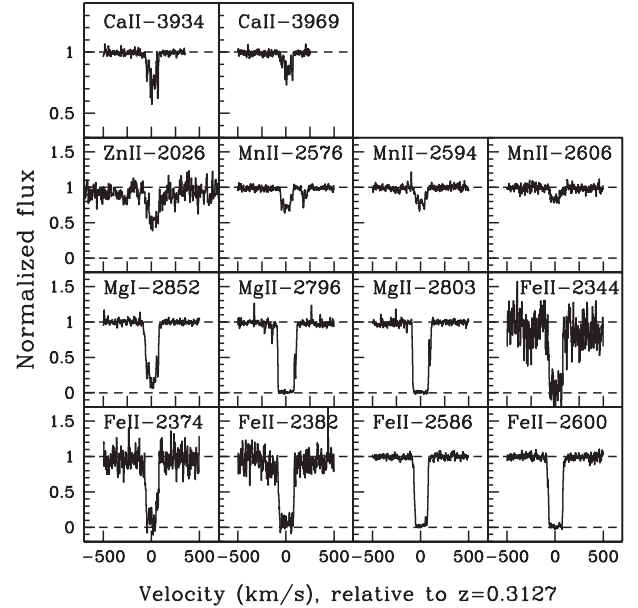
Figure 7. Low-ionization metal absorption profiles from the $z = 0.3127$ DLA towards 1127−145, from the VLT-UVES and *HST*-STIS spectra. The *x*-axis contains velocity, in km s^{-1}, relative to the DLA redshift.

3 SPIN TEMPERATURES, COVERING FACTORS AND VELOCITY WIDTHS

For a DLA towards a radio-loud background quasar, the H I column density $N_{\rm H_I}$, the H I 21 cm optical depth $\tau_{21\,cm}$ and the spin temperature T_s are related by the expression (Rohlfs & Wilson 2006)

$$N_{\rm H_I} = C_0 \times T_s \times \int \tau_{21\,cm}\, dV, \tag{1}$$

where $N_{\rm H_I}$ is in cm^{-2}, T_s is in K, the integral $\int \tau_{21\,cm}\, dV$ is over the observed line profile in velocity space, in km s^{-1}, and the constant $C_0 = 1.823 \times 10^{18}$ cm^{-2} K^{-1} km^{-1} s. Note that the H I 21 cm optical

depth is given by $\tau_{21\,cm} = -\log\left[1 - \Delta S/S\right]$, where ΔS is the line depth and S is the flux density of the background quasar.

Equation (1) implicitly assumes that the all quantities are measured at the same spatial resolution. However, in the case of DLAs, the H I column density is measured from the redshifted Lyman α absorption line towards the optical quasar, i.e. along a narrow pencil beam through the absorber. Conversely, the H I 21 cm optical depth is measured against the more extended radio emission. Ideally, the H I 21 cm absorption studies should be carried out with very long baseline interferometry (VLBI), so that the radio and optical sight-lines have similar transverse extents in the absorber. Unfortunately,

Figure 8. Low-ionization metal absorption profiles from the $z = 0.5247$ DLA towards 0827+243, from the VLT-UVES spectrum. The *x*-axis contains velocity, in km s^{-1}, relative to the DLA redshift.
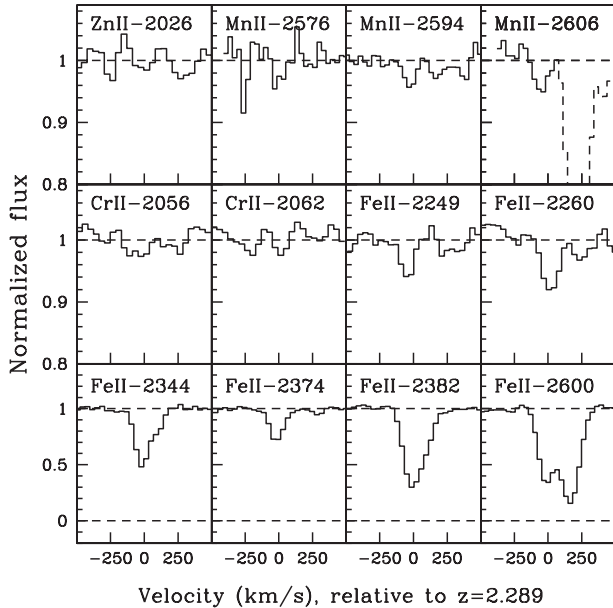
Figure 9. Low-ionization metal absorption profiles from the $z = 2.2890$ DLA towards 0311+430, from the GMOS-N spectrum. The *x*-axis contains velocity, in km s^{-1}, relative to the DLA redshift. The dashed part of the spectrum indicates absorption from a different redshift, which is slightly blended with the Mn II λ2606 line from the $z = 2.2890$ DLA.

current VLBI arrays such as the VLBA or the European VLBI Network have both very poor low frequency coverage and low sensitivity. Further, even the 1000 km baselines of the next-generation Square Kilometre Array would only give a spatial resolution of ≈ 1 kpc at the redshift of a DLA at $z \approx 2$ (e.g. Kanekar & Briggs 2004), far worse than the 'effective' resolution of hundreds of au allowed by optical absorption spectroscopy (arising from the size of the background quasar). As a result, H I 21 cm absorption studies are likely to continue to probe conditions on far larger spatial

scales than optical absorption studies in the foreseeable future. One must hence attempt to correct for resolution effects, as has been done in the present and earlier studies (e.g. Briggs & Wolfe 1983; Carilli et al. 1996; Kanekar et al. 2009a; Ellison et al. 2012). This is discussed in detail below.

There are two effects that must be taken into account in the case of H I 21 cm absorption studies at low angular resolution. First, for extended radio structure in the quasar, the foreground absorber may cover only part of the radio emission, but the angular extent of the emission may be smaller than the telescope beam and hence unresolved. In such cases, if the (unresolved) total quasar flux density measured by the observer is S Jy, but only a fraction f of this emission is covered by the foreground absorber, the true H I 21 cm optical depth is larger than the observed optical depth. The H I 21 cm optical depth corrected for covering factor effects is given by $\tau_{21\,cm} = -\log\left[1 - \Delta S/(fS)\right]$ and equation (1) is modified to

$$N_{\rm H\,I} = 1.823 \times 10^{18} \times T_{\rm s} \times \int -\log\left[1 - \frac{\Delta S}{f\,S}\right] {\rm d}V, \qquad (2)$$

where f is referred to as the DLA covering factor. For most DLAs, the H I 21 cm optical depth is low, $\tau_{21\,cm} \ll 1$, and the expression reduces to

$$N_{\rm H\,I} = 1.823 \times 10^{18} \times [T_{\rm s}/f] \int \frac{\Delta S}{S} {\rm d}V. \qquad (3)$$

The covering factor f is included in the above equation to account for the fact that low-frequency radio emission is often very extended, implying that the foreground DLA may not cover the entire background radio emission. The angular resolution of redshifted H I 21 cm absorption studies (with single dishes or short-baseline interferometers like the GMRT or WSRT) is typically quite poor ($\gtrsim 10$ arcsec for even the GMRT, i.e. $\gtrsim 80$ kpc for a DLA at $z \sim 3$), and the measured H I 21 cm optical depth is hence a lower limit, because some of the radio emission may not be covered by the absorber. Curran et al. (2005) have emphasized unknown covering factors as a critical issue in interpreting the high spin temperatures typically obtained in H I 21 cm absorption studies of high-z DLAs. This is because an apparently low H I 21 cm optical depth could arise due to an unknown low covering factor, a high spin temperature or an overestimated H I column density.

The covering factor can be estimated from VLBI studies close to the redshifted H I 21 cm line frequency (Briggs & Wolfe 1983; Kanekar et al. 2009a), to measure the compact flux density arising from the radio core at this frequency. The ratio of the core flux density to the total source flux density gives the quasar core fraction. In the following, we will assume that this quantity is a reasonable estimate of the covering factor. We note that this is not formally a measurement of the covering factor for an individual absorber because (1) it is possible that the absorber covers some fraction of the extended emission, in addition to the core emission, and (2) it is also possible that the absorber does not entirely cover the radio core. The latter is unlikely if the core size is significantly smaller than the size of a typical galaxy at the absorber redshift. Thus, for core sizes $\lesssim 1$ kpc, the ratio of the core flux density to the total source flux density should provide at least a lower limit to the covering factor.

We note, in passing, that the results of the paper are derived under the assumption that the DLA covering factor is equal to the quasar core fraction. However, in Section 7.9, we consider the possibility that the core fraction and covering factor are entirely unrelated, and use Monte Carlo simulations to show that the hypothesis that they are equal is actually not required for the results described below.

Table 4. The main sample of DLAs with H I 21 cm absorption studies and low-frequency VLBI estimates of the covering factor. See Section 6 for a description of the columns of the table.

QSO	z_{QSO}	z_{abs}	$\log[N_{HI}/cm^{-2}]$	f	T_s (K)	[Z/H]	Z	[Z/Fe]	Dust	ΔV_{90}^a (km s^{-1})	Line	Refs.[b]
0738+313	0.635	0.0912	21.18 ± 0.06	0.98	775 ± 100	−1.21 ± 0.16	Fe[c]	<0.46	Fe	42	Ti II λ3384	2–5
0738+313	0.635	0.2212	20.90 ± 0.08	0.98	870 ± 160	<−0.72	Zn	<0.71	Cr	60	Mg Iλ2852	2–6
0952+179	1.472	0.2378	21.32 ± 0.06	0.66	6470 ± 965	−1.89 ± 0.06	Fe[c]	<1.27	Fe	98	Mg Iλ2852	1, 5, 7–9
1127−145	1.184	0.3127	21.70 ± 0.08	0.90	820 ± 145	−0.76 ± 0.10	Zn	<1.23	Fe	123	Ca II λ3934	1, 6, 7, 9, 10
1229−021	1.043	0.3950	20.75 ± 0.07	0.42	95 ± 15	−0.45 ± 0.15	Zn	>0.81	Fe	122	Mn II λ2576	9, 11–13
0235+164	0.940	0.5242	21.70 ± 0.09	1.00	210 ± 45	−0.14 ± 0.17	XR[d]	1.71 ± 0.45	Fe	−	−	14, 15, 16
0827+243	0.939	0.5247	20.30 ± 0.04	0.70	330 ± 65	−0.51 ± 0.05	Fe[c]	−	−	188	Fe II λ2374	5, 7–9, 16
1429+400	1.215	0.6039	21.20 ± 0.10	0.32	90 ± 23	−0.80 ± 0.21	Zn	0.70 ± 0.24	Fe	70	Mn II λ2576	17
1122−168	2.400	0.6819	20.45 ± 0.05	0.04	>100	−0.90 ± 0.29	Fe[c]	<−0.17	Fe	144	Fe II λ2586	1, 18
1331+305	0.849	0.6922	21.25 ± 0.02	0.90	965 ± 105	−1.35 ± 0.05	Zn	0.26 ± 0.06	Fe	26	Mn II λ2576	12, 19, 20
0454+039	1.350	0.8596	20.69 ± 0.06	0.50	>1380	−0.99 ± 0.12	Zn	−0.02 ± 0.12	Fe	100	Fe II λ2260	1, 12, 21, 22
2149+212	1.538	0.9115	20.70 ± 0.10	0.02	>55	<−0.93	Zn	−	−	−	−	1, 23, 24
2355−106	1.639	1.1727	21.00 ± 0.10	1.00	2145 ± 570	−0.87 ± 0.20	Zn	0.50 ± 0.23	Fe	126	Mn II λ2576	17, 25, 26
1621+074	1.648	1.3367	21.35 ± 0.10	0.34	460 ± 105	−1.07 ± 0.14	Zn	0.45 ± 0.15	Fe	55	Fe II λ2260	17, 26
2003−025	1.457	1.4106	20.54 ± 0.20	0.81	485 ± 195	−	−	−	−	−	−	1, 24, 25
1331+170	2.084	1.7764	21.18 ± 0.07	0.72	625 ± 115	−1.27 ± 0.09	Zn	0.74 ± 0.09	Fe	72	Si II λ1808	9, 27–30
1157+014	2.000	1.9436	21.80 ± 0.07	0.63	1015 ± 255	−1.44 ± 0.10	Zn	0.35 ± 0.10	Fe	84	Ni II λ1741	9, 31–34
0458−020	2.286	2.0395	21.78 ± 0.07	1.00	560 ± 95	−1.27 ± 0.08	Zn	0.45 ± 0.10	Fe	84	Cr II λ2056	27, 35–37
2039+187	3.056	2.1920	20.70 ± 0.09	0.35	160 ± 35	−	−	−	−	−	−	38, 39
1048+347	2.520	2.2410	20.54 ± 0.06	0.69	>2155	−	−	−	−	−	−	38, 39
0311+430	2.870	2.2890	20.30 ± 0.11	0.52	72 ± 18	−0.49 ± 0.13	Fe[c]	>0.33	Fe	−	−	1, 38–40
0432−440	2.649	2.3020	20.78 ± 0.11	0.38	>555	−1.09 ± 0.13	Si	0.34 ± 0.15	Fe	125	Fe II λ1608	1, 41, 42
0438−436	2.863	2.3474	20.78 ± 0.11	0.59	900 ± 250	−0.69 ± 0.12	Zn	0.59 ± 0.16	Fe	55	Fe II λ2260	1, 41–43
0229+230	3.420	2.6200	20.30 ± 0.11	0.30	>140	−	−	−	−	−	−	38, 39
0229+230	3.420	2.6830	20.70 ± 0.09	0.30	>270	−	−	−	−	−	−	38, 39
1402+044	3.215	2.7076	21.01 ± 0.23	0.34	>890	−	−	−	−	−	−	1, 44–46
0913+003	3.074	2.7434	20.74 ± 0.11	0.54	>925	−1.44 ± 0.16	Si	0.13 ± 0.19	Fe	105	Si II λ1526	1, 41, 42
2039+187	3.056	2.7520	20.70 ± 0.09	0.35	>790	−	−	−	−	−	−	38, 39
1354−170	3.147	2.7799	20.30 ± 0.15	0.97	>1030	−1.83 ± 0.16	Si	0.54 ± 0.18	Fe	30	Fe II λ1608	1, 47
0800+618	3.033	2.9603	20.50 ± 0.02	0.63	>570	−	−	−	−	−	−	1, 48
0537−286	3.110	2.9746	20.30 ± 0.11	0.47	>520	<−0.40	Zn	−	−	−	−	9, 41, 42, 49
2342+342	3.053	2.9084	21.10 ± 0.10	0.71	>2200	−1.06 ± 0.10	S	0.47 ± 0.12	Fe	100	Si II λ1808	1, 9, 47, 50
0336−017	3.197	3.0621	21.20 ± 0.10	0.68	>8890	−1.36 ± 0.10	S	0.39 ± 0.11	Fe	108	Si II λ1250	1, 9, 30, 51
0335−122	3.442	3.1799	20.78 ± 0.11	0.62	>1850	−2.53 ± 0.16	Si	0.07 ± 0.19	Fe	39	Al II λ1670	9, 41, 42, 49
0201+113	3.639	3.3869	21.25 ± 0.07	0.76	1050 ± 175	−1.19 ± 0.17	S	0.16 ± 0.22	Fe	64	Ni II λ1317	9, 52–55
1239+376	3.819	3.4110	20.40 ± 0.09	0.54	>2330	−	−	−	−	−	−	38, 39
1418−064	3.689	3.4482	20.40 ± 0.10	0.69	>930	−1.45 ± 0.14	Si	0.25 ± 0.17	Fe	41	Fe II λ1608	1, 9, 41, 42

[a]Most of the ΔV_{90} measurements were carried out by us; a few values are taken from Prochaska & Wolfe (1999) and Ledoux et al. (2006).

[b]References for N_{HI}, metallicity, covering factor and spin temperature estimates: (1) This work, (2) Rao & Turnshek (1998), (3) Chengalur & Kanekar (1999), (4) Lane, Briggs & Smette (2000), (5) Kulkarni et al. (2005), (6) Lane et al. (1998), (7) Rao & Turnshek (2000), (8) Kanekar & Chengalur (2001b), (9) Kanekar et al. (2009a), (10) Chengalur & Kanekar (2000), (11) Brown & Spencer (1979), (12) Boisse et al. (1998), (13) Lanzetta & Bowen (1992), (14) Roberts et al. (1976), (15) Junkkarinen et al. (2004), (16) Chen, Kennicutt & Rauch (2005), (17) Ellison et al. (2012), (18) de la Varga et al. (2000), (19) Wolfe et al. (2008b), (20) Brown & Roberts (1973), (21) Pettini et al. (2000), (22) Steidel et al. (1995), (23) Nestor et al. (2008), (24) Rao, Turnshek & Nestor (2006), (25) Kanekar et al. (2009b), (26) Gupta et al. (2009), (27) Wolfe & Davis (1979), (28) Carswell et al. (2011), (29) Prochaska & Wolfe (1999), (30) Prochaska et al. (2001), (31) Wolfe et al. (1981), (32) Ledoux et al. (2003), (33) Dessauges-Zavadsky et al. (2007), (34) Dessauges-Zavadsky et al. (2006), (35) Wolfe et al. (1985), (36) Briggs et al. (1989), (37) Møller et al. (2004), (38) Ellison et al. (2008), (39) Kanekar et al. (2013), (40) York et al. (2007), (41) Ellison et al. (2001b), (42) Akerman et al. (2005), (43) Kanekar et al. (2006), (44) Prochaska et al. (2005), (45) Noterdaeme et al. (2009), (46) Curran et al. (2010), (47) Prochaska et al. (2003a), (48) Jorgenson et al. (2006), (49) Kanekar & Chengalur (2003), (50) Prochaska et al. (2007), (51) Ledoux et al. (2006), (52) White, Kinney & Becker (1993), (53) Kanekar et al. (2007), (54) Srianand et al. (2012), (55) Ellison et al. (2001c), (56) Møller & Warren (1993), (57) Lu et al. (1996), (58) Srianand et al. (2010), (59) Storrie-Lombardi & Wolfe (2000), (60) Lopez & Ellison (2003), (61) Ledoux, Bergeron & Petitjean (2002), (62) Bergeron & Stasińska (1986) and (63) Roy et al. (2013).

[c]In five DLAs, at $z = 0.0912$ towards 0738+313, $z = 0.2378$ towards 0952+179, $z = 0.5247$ towards 0827+243, $z = 0.6819$ towards 1122−168 and $z = 2.2890$ towards 0311+430, the metallicity was estimated using [Z/H] = [Fe/H] +0.4, following Prochaska et al. (2003b). However, in four of the five cases (excluding the DLA towards 0827+243), limits are also available on [Zn/H] or [Si/H]; these limits were used along with the [Fe/H] measurements to derive the dust depletion [Z/Fe].

[d]In the case of the $z = 0.5242$ DLA towards 0235+164, the metallicity is from an X-ray absorption study (Junkkarinen et al. 2004).

Until quite recently, there were very few estimates of DLA covering factors from low-frequency VLBI studies. This is because such studies are technically challenging due to propagation effects in the atmosphere, which can result in decorrelation of the signals on the long VLBI baselines. However, over the last few years, covering factors have been estimated for a large number of high-z DLAs, mostly with the low-frequency receivers of the VLBA (e.g. Kanekar et al. 2009a, 2013; Ellison et al. 2012; Srianand et al. 2012; this work).

The second issue that must be taken into account in the case of H I 21 cm absorption studies at low angular resolution is the fact that, for DLAs, the H I column density in equation (3) is determined from the Lyman -α profile. Using this to derive the spin temperature involves the assumption that the H I columns along the optical and radio sightlines are the same. Since the optical quasar is far smaller than the radio core (typically, sizes of 100–1000 au at optical wavebands and $\gtrsim 10$ pc in the radio), the H I column densities can, in principle, be different along the two sightlines. This assumption will be examined in detail in Section 7.3.

Next, for neutral gas along the line of sight at different temperatures, the spin temperature derived from equation (3) is the column-density-weighted harmonic mean of the spin temperatures of the different phases, i.e.

$$\frac{1}{T_s} = \Sigma_i \frac{n_i}{T_{s,i}} \ , \tag{4}$$

where $n_i = N_i / N_{\rm H I}$ is the fraction of the total H I column density in the ith cloud and $T_{s,i}$ is its spin temperature. Thus, a measurement of $T_s = T$ along a sightline could arise due to the presence of either a single intervening H I 'cloud' with this spin temperature or a combination of clouds with spin temperatures above and below the measured value, T. For example, a measured spin temperature of ≈ 1000 K does not rule out the classic 'two-phase' model of the neutral Galactic ISM (Field, Goldsmith & Habing 1969; McKee & Ostriker 1977), as this would arise naturally for sightlines with two types of H I 'clouds', at temperatures of ≈ 100 and ≈ 8000 K.

It should be emphasized that the spin temperature along multiphase sightlines is biased towards cold gas. Specifically, a sightline with H I equally divided between cold and warm phases, at spin temperatures of $T_s = 100$ and 8000 K, respectively, would yield a derived spin temperature of ≈ 180 K. Conversely, a sightline with 90 per cent of the H I at $T_s = 8000$ K and 10 per cent at $T_s = 100$ K would yield a derived spin temperature of ≈ 900 K. Further, collisions drive the spin temperature towards the gas kinetic temperature (≈ 40–200 K; Wolfire et al. 1995) in the cold neutral medium (CNM). However, in the warm neutral medium (WNM), the number density is too low to thermalize the transition and the spin temperature is typically significantly lower than the kinetic temperature T_k (e.g. $T_s \approx 1000$–4000 K for $T_k \approx 5000$–8000 K; Liszt 2001). The result of both these effects is that a high measured spin temperature ($\gtrsim 1000$ K) can only be explained by a preponderance of neutral gas in the WNM. The only caveat to this statement is if the H I column density measured towards the optical quasar is significantly larger than that towards the radio core, which, as we will discuss in Section 7.3, may occur on individual sightlines but is very unlikely to arise in a systematic manner.

For DLAs that do not show detectable H I 21 cm absorption, one can use the upper limit on the H I 21 cm optical depth in equation (3) to obtain a lower limit to the spin temperature. The derived limit depends on the assumed shape of the velocity profile; further, the detection sensitivity worsens with increasing line width ($\propto \sqrt{\Delta V}$, where ΔV is the line FWHM), implying that significant non-thermal broadening makes it harder to detect H I 21 cm absorption. For non-detections, we will in all cases assume a Gaussian profile of FWHM = 15 km s^{-1}, corresponding to thermally broadened H I at a kinetic temperature of 5000 K (i.e. in the WNM range). This is a conservative strategy as it allows for significant non-thermal broadening of cold H I along the line of sight. We also note that individual H I 21 cm spectral components in DLAs with detected H I 21 cm absorption typically have FWHMs of 5–15 km s^{-1}.

4 PROXIMATE DLAs AND SUB-DLAs

Two sub-classes of damped absorbers, proximate DLAs ('PDLAs') and sub-DLAs, merit special mention (see also Ellison et al. 2012). PDLAs are defined as absorbers with redshifts within ≈ 3000 km s^{-1} of the quasar redshift, i.e. arising in gas associated with the quasar host galaxy (e.g. Møller, Warren & Fynbo 1998; Ellison et al. 2002; Prochaska, Hennawi & Herbert-Fort 2008b). For such systems, the population distribution in the hyperfine levels, and thus the spin temperature, will be significantly influenced by the quasar radiation field at the H I 21 cm line frequency (e.g. Field 1958; Wolfe & Burbidge 1975). Since this complicates the interpretation of the derived spin temperatures, we will exclude PDLAs from the later analysis and discussion.

Sub-DLAs are absorbers with H I column densities below the defining DLA column density of $N_{\rm H I} = 2 \times 10^{20}$ cm^{-2}, but which still show damping wings in the Lyman α profile (e.g. Péroux et al. 2003). Numerical estimates of self-shielding against the UV background in DLAs and sub-DLAs suggest that the absorbers are physically distinct: these studies find that most of the gas in DLAs is neutral, while that in sub-DLAs is predominantly ionized and at high temperatures (Viegas 1995; Prochaska 1999; Wolfe et al. 2005; Milutinovic et al. 2010). In keeping with the above, recent Galactic H I 21 cm absorption studies have shown that the CNM fraction increases sharply at $N_{\rm H I} \approx 2 \times 10^{20}$ cm^{-2}, with very low CNM fractions below this threshold (Kanekar, Braun & Roy 2011). Sub-DLAs are thus likely to show significantly higher spin temperatures than DLAs; we will hence exclude them from the full sample and the later analysis.

5 NOTES ON INDIVIDUAL SOURCES

The H I 21 cm optical depths listed in Table 1 and the covering factors of Table 2 and Kanekar et al. (2009a) were used to derive spin temperatures for the DLAs and sub-DLAs of our sample whose H I 21 cm data were not affected by RFI. The elemental abundances of Table 3 were used to complement and, in some cases, to improve the metallicities given in the literature. This section briefly summarizes the results for each absorber for which new data have been presented in this paper, again in order of increasing right ascension.

(i) *0201+113, z = 3.3869*: the *z = 3.3869* DLA towards 0201+113 was detected by White et al. (1993) and its H I column density was measured to be $N_{\rm H I} = (1.8 \pm 0.3) \times 10^{21}$ cm^{-2} by Ellison et al. (2001c). After inconclusive results from a number of H I 21 cm absorption studies with different radio telescopes (de Bruyn et al. 1996; Briggs et al. 1997; Kanekar & Chengalur 1997), H I 21 cm absorption was finally detected from this absorber with the GMRT (Kanekar et al. 2007). The DLA covering factor is $f = 0.76$, from a 327 MHz VLBA imaging study (Kanekar et al. 2009a), yielding a spin temperature of $T_s = (1050 \pm 175) \times (f/0.76)$ K.

(ii) *0311+430, z = 2.2890*: the *z = 2.2890* DLA towards 0311+430 was found by Ellison et al. (2008) and has an H I column density of $(2.0 \pm 0.5) \times 10^{20}$ cm^{-2} and a spin temperature of $T_s = (72 \pm 18) \times (f/0.52)$ K (York et al. 2007; Kanekar et al. 2013). The Si II λ1808 line, detected in the original low-resolution GMOS spectrum, yields [Si/H] > -0.56, assuming the line to be unsaturated (York et al. 2007; Ellison et al. 2008). We do not detect the Zn II λ2026 line in our new GMOS spectrum (see Table 3), implying $\log[N_{\rm Zn II}/{\rm cm}^{-2}] < 12.5$ and [Zn/H] < -0.43. The metallicity of the $z = 2.2890$ DLA thus lies in the range $-0.56 <$ [Z/H] < -0.43, from the Zn II upper limit and the Si II lower limit. However, we clearly detect the Fe II$\lambda\lambda$2249, 2260 and 2374 transitions in

the new GMOS spectrum, with $\log[N_{\mathrm{Fe\,II}}/\mathrm{cm}^{-2}] = 14.91 \pm 0.05$, 14.80 ± 0.10 and > 14.32, respectively. Note that the Fe IIλ2374 line yielded a lower column density than the other two lines, probably due to saturation effects. We have hence listed this as a lower limit, and used the former two lines to obtain $\log[N_{\mathrm{Fe\,II}}/\mathrm{cm}^{-2}] = 14.86 \pm 0.06$ and $[\mathrm{Fe/H}] = -0.89 \pm 0.13$. This yields a metallicity of $[\mathrm{Z/H}] = [\mathrm{Fe/H}] + 0.4 = -0.49 \pm 0.13$ for the $z = 2.2890$ DLA.

(iii) *0336−017, $z = 3.0621$*: the $z = 3.0621$ DLA towards $0336-017$ was found by Lu et al. (1993), with an H I column density of $N_{\mathrm{H\,I}} = (1.5 \pm 0.3) \times 10^{21}$ cm^{-2} (Prochaska et al. 2001). The DLA covering factor is $f = 0.68$ (Kanekar et al. 2009a); our upper limit on the H I 21 cm optical depth then yields the lower limit $T_s > 8890 \times (f/0.68)$ K on the DLA spin temperature, assuming an FWHM of 15 km s^{-1} for the H I 21 cm line. We note that this T_s limit is extremely high, at the upper end of the range of WNM kinetic temperatures. The low-ionization metal lines of this DLA have a relatively large velocity spread, $\Delta V_{90} \approx 108$ km s^{-1} (see Table 4). However, even assuming that the H I 21 cm line has a comparable velocity FWHM (perhaps due to non-thermal broadening) would only lower the spin temperature limit to $T_s \gtrsim 8890 \times \sqrt{(15/108)}$, i.e. to $T_s \gtrsim 3315$ K. The H I content in this DLA thus appears to be dominated by warm gas, unless there is significant small-scale structure along the sightline and the H I column along the radio sightline is much lower than that towards the optical quasar.

(iv) *0347−211, $z = 1.9470$*: the $z = 1.9470$ DLA towards $0347-211$ was detected by Ellison et al. (2001b) in the CORALS survey, and has an H I column density of $N_{\mathrm{H\,I}} = (2.0 \pm 0.5) \times 10^{20}$ cm^{-2}. No low-frequency VLBI images of the background quasar are currently available; we hence do not have a reliable estimate of its covering factor. Our upper limit on the H I 21 cm optical depth yields $T_s > (380 \times f)$ K.

(v) *0405−331, $z = 2.5693$*: the PDLA towards $0405-331$ has an H I column density of $N_{\mathrm{H\,I}} = (4 \pm 1) \times 10^{20}$ cm^{-2} (Ellison et al. 2001b) and a covering factor of $f = 0.44$ (Kanekar et al. 2009a), yielding $T_s > 1220 \times (f/0.44)$ K.

(vi) *0432−440, $z = 2.3020$*: the $z = 2.3020$ DLA towards $0432-440$ has an H I column density of $N_{\mathrm{H\,I}} = (6.0 \pm 1.5) \times 10^{20}$ cm^{-2} (Ellison et al. 2001b). The VLBA 327 MHz image of this DLA shows a weak extension, but we were unable to obtain a stable two-component fit (probably due to the weakness of the extension); we hence used a single-Gaussian model here, obtaining $f = 0.38$. Combining this with our upper limit on the H I 21 cm optical depth yields $T_s > 555 \times (f/0.38)$ K.

(vii) *0438−436, $z = 2.3474$*: this DLA has an H I column density of $N_{\mathrm{H\,I}} = (6.0 \pm 1.5) \times 10^{20}$ cm^{-2} (Ellison et al. 2001b) and a covering factor of $f = 0.59$ (Kanekar et al. 2009a). The GBT detection of H I 21 cm absorption then yields $T_s = (900 \pm 250) \times (f/0.59)$ K (Kanekar et al. 2006).

(viii) *0454+039, $z = 0.8597$*: the $z = 0.8597$ DLA towards $0454+039$ has an H I column density of $N_{\mathrm{H\,I}} = (5.0 \pm 0.7) \times 10^{20}$ cm^{-2} (Boisse et al. 1998; see also Steidel et al. 1995) and a covering factor $f = 0.53$ (Kanekar et al. 2009a). Our GBT upper limit to the H I 21 cm optical depth then yields $T_s > 990 \times (f/0.53)$ K.

(ix) *0458−020, $z = 2.0395$*: there are multiple estimates of the H I column density of this DLA, $N_{\mathrm{H\,I}} = (4.5 - 6) \times 10^{21}$ cm^{-2} (Wolfe et al. 1993; Pettini et al. 1994; Møller et al. 2004; Heinmüller et al. 2006), from different telescopes and spectrographs, all consistent with each other within the measurement errors. We will use the value $N_{\mathrm{H\,I}} = (6 \pm 1) \times 10^{21}$ cm^{-2} (Møller et al. 2004), as this was obtained from a high-sensitivity VLT-FORS1 spectrum (the other results use either echelle spectroscopy or 4 m class telescopes).
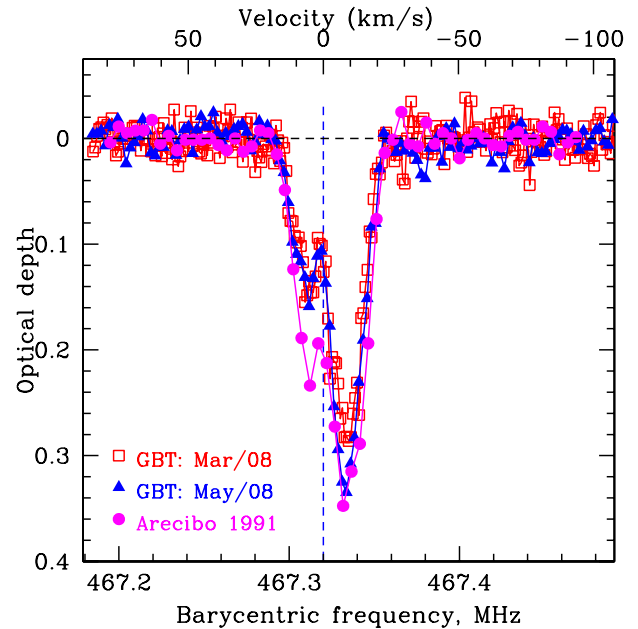
Figure 10. Comparison between the H I 21 cm absorption profiles obtained from the $z = 2.0395$ DLA towards $0458-020$ with the Arecibo telescope (in 1991) and the GBT telescope (in 2008 March and May).

H I 21 cm absorption in the $z = 2.0395$ DLA was originally detected by Wolfe et al. (1985), with two distinct absorption components (see also Briggs et al. 1989). We observed the H I 21 cm line with the GBT on two separate occasions, in 2008 March and May; these spectra are shown in Fig. 10, overlaid on an old H I 21 cm spectrum obtained with the Arecibo telescope (kindly provided by Art Wolfe). The GBT and Arecibo spectra are clearly different, with the secondary H I 21 cm component significantly weaker in the GBT spectra. We note that part of this discrepancy might arise due to flux scale errors (and perhaps bandpass calibration issues) in the Arecibo spectrum, given that the source is at the edge of the Arecibo declination range. However, while the secondary component has the same depth in the two GBT runs, a statistically significant difference is seen in the primary component. Indeed, the integrated H I 21 cm optical depths obtained at the GBT are $\int \tau_{21\,\mathrm{cm}}\, \mathrm{d}V = (5.534 \pm 0.080)$ km s^{-1} in 2008 March and $\int \tau_{21\,\mathrm{cm}}\, \mathrm{d}V = (6.198 \pm 0.088)$ km s^{-1} in 2008 May; the difference has $\approx 5\sigma$ significance, indicating that the H I 21 cm absorption has changed on a time-scale of ≈ 2 months. No significant narrow-band interference was observed on either observing run, and the Doppler shift between the runs is ≈ 20 km s^{-1}, comparable to the FWHMs of the components. We conclude that the spectra show evidence for variability in the H I 21 cm profile, on time-scales of months, and possibly of years. Such line variations have been seen earlier, on time-scales as short as a few days, in two low-z DLAs, at $z \sim 0.5242$ towards AO0235+164 (Wolfe, Briggs & Davis 1982) and $z \sim 0.3127$ towards $1127-145$ (Kanekar & Chengalur 2001a). They can be explained by a number of scenarios, including refractive interstellar scintillation, gravitational microlensing, transverse motion of compact components in the quasar radio jet, etc. (e.g. Briggs 1983; Gwinn 2001; Kanekar & Chengalur 2001a; Macquart 2005), all typically requiring small-scale structure in the quasar radio emission, the ISM of the absorber and/or the ISM of the Galaxy.

The DLA covering factor has been estimated to be ≈ 1 from a VLBI study in the H I 21 cm line (Briggs et al. 1989). The average integrated H I 21 cm optical depth from the two GBT

Table 5. DLAs or sub-DLAs with H I 21 cm absorption studies, but not included in the 'main' sample.

QSO	z_{QSO}	z_{abs}	$\log[N_{H I}/\text{cm}^{-2}]$	f	T_s (K)	[Z/H]	Z	[Z/Fe]	Dust	ΔV_{90} (km s^{-1})	Line	Refs.[b]
PDLAs, with the absorber within 3000 km s^{-1} of the background quasar
0105−008	1.374	1.3708	21.70 ± 0.15	0.32	305 ± 45	−1.40 ± 0.16	Zn	0.16 ± 0.16	Fe	33	Fe II λ2249	9, 17, 26
0824+355	2.249	2.2433	20.30	0.20	>320	–	–	–	–	–	–	1, 48
0405−331	2.570	2.5693	20.60 ± 0.11	0.44	>1220	−1.37 ± 0.16	Si	0.35 ± 0.19	Fe	261	Si II λ1526	1, 41, 42
1013+615	2.805	2.7681	20.60 ± 0.15	0.81[a]	>945	–	–	–	–	–	–	1, 44, 54
0528−250	2.813	2.8110	21.35 ± 0.07	0.94	>2103	−0.89 ± 0.10	Zn	0.45 ± 0.13	Fe	304	S II λ1253	1, 54, 56, 57
1354−107	3.006	2.9660	20.78 ± 0.11	–	>615	−1.28 ± 0.16	Si	0.24 ± 0.19	Fe	59	Si II λ1808	41, 42, 49
J1337+3152	3.174	3.1745	21.36 ± 0.10	1.00[a]	600 ± 297	−1.73 ± 0.28	Zn	0.17 ± 0.29	Fe	–	–	58
Sub-DLAs, with $N_{H I} < 2 \times 10^{20}$ cm^{-2}
2128−123	0.501	0.4297	19.37 ± 0.08	–	>980	–	–	–	–	–	–	49, 61
0215+015	1.715	1.3439	19.89 ± 0.09	–	>1020	−0.66 ± 0.22	Fe	–	–	–	–	49, 62
0237−233	2.223	1.6724	19.78 ± 0.07	0.90	390 ± 125	−0.57 ± 0.12	Zn	0.09 ± 0.12	Fe	43	Fe II λ2374	17, 25
1402+044	3.215	2.4850	20.20 ± 0.20	0.35	>380	–	–	–	–	–	–	1, 44–46
J1406+3433	2.566	2.4989	20.20 ± 0.20	0.76	>210	–	–	–	–	–	–	44, 45, 54
J0733+2721	2.938	2.7263	20.25 ± 0.20	–	>690	–	–	–	–	–	–	45, 54
DLAs with covering factor estimates at frequencies significantly higher (>1.5 times) the redshifted H I 21 cm line frequency
0620+389	3.469	2.0310	20.30 ± 0.11	0.79	>400	–	–	–	–	–	–	38, 39
J0852+2431	3.617	2.7902	20.70 ± 0.20	0.49	>420	–	–	–	–	–	–	45, 54
J0816+4823	3.573	3.4358	20.80 ± 0.20	0.60	>145	–	–	–	–	–	–	45, 54
Absorbers without covering factor estimates
J0011+1446	4.967	3.4523	21.65 ± 0.15	–	>3040	–	–	–	–	–	–	63
0347−211	2.944	1.9470	20.30 ± 0.11	–	>380	<−0.55	Zn	–	–	–	–	1, 41, 42
1614+051	3.215	2.5200	20.40	–	>450	–	–	–	–	–	–	1, 59
J0407−4410	3.020	2.5950	21.05 ± 0.10	–	>380	−1.00 ± 0.10	Zn	0.35 ± 0.10	Fe	79	Si II λ1808	51, 54, 60
J0407−4410	3.020	2.6214	20.47 ± 0.10	–	>80	−1.99 ± 0.12	Si	0.33 ± 0.12	Fe	–	–	54, 60
J0801+4725	3.276	3.2235	20.70 ± 0.15	–	>2820	–	–	–	–	–	–	45, 54, 63
J1435+5435	3.811	3.3032	20.30 ± 0.20	–	>420	–	–	–	–	–	–	45, 54

References: see Table 4.
[a]These PDLAs also have covering factor estimates at frequencies >1.5 times higher than the redshifted H I 21 cm line frequency.

runs is $\int \tau_{21\,cm}\,dV = (5.866 \pm 0.059)$ km s^{-1}; we then obtain $T_s = (560 \pm 95)$ K, assuming $f = 1$. Note that the H I 21 cm optical depth is fairly high, $\tau \approx 0.3$, implying that the low optical depth approximation of equation (3) should not be used.

(x) *0528−250, z = 2.8112*: the $z = 2.8112$ PDLA towards 0528−250 has an H I column density of $(2.24 \pm 0.05) \times 10^{21}$ cm^{-2} (Møller & Warren 1993) and a covering factor of unity (Kanekar et al. 2009a). Our WSRT non-detection of H I 21 cm absorption then yields $T_s > 925 \times (f/1.0)$ K. We note that Srianand et al. (2012) present a GBT spectrum of this absorber, obtaining an upper limit of $\int \tau_{21\,cm}\,dV < 0.58$ km s^{-1} and $T_s > 2103$ K, using the *b*-parameter of the detected H$_2$ absorption for the line width. We have quoted this result in Table 5, due to its higher sensitivity.

(xi) *0738+313, z = 0.0912*: this is the lowest redshift DLA of the sample, with $N_{H I} = (1.5 \pm 0.21) \times 10^{21}$ cm^{-2} (Rao & Turnshek 1998) and $T_s = (775 \pm 100) \times (f/0.98)$ K (Chengalur & Kanekar 1999; Lane et al. 2000). Note that this is one of the few DLAs whose spin temperature has been directly measured from a VLBA H I 21 cm absorption study (Lane et al. 2000). Kulkarni et al. (2005) detected Fe II and Cr II absorption from this system in an *HST*-STIS spectrum, yielding [Fe/H] = −1.61 ± 0.16 and [Cr/H] = −1.55 ± 0.23; their non-detection of Zn II λ2026 absorption gives [Zn/H] < −1.15. Our Keck-HIRES spectrum yields $\log[N_{Ti II}/\text{cm}^{-2}] = 12.51 \pm 0.04$ and thus a titanium abundance [Ti/H] = −1.58 ± 0.08. This is consistent with the original Ti II detection of Khare et al. (2004), from a medium-resolution spectrum ($\log[N_{Ti II}/\text{cm}^{-2}] = 12.53^{+0.14}_{-0.06}$).

(xii) *0738+313, z = 0.2212*: the second DLA towards 0738+313 was also detected by Rao & Turnshek (1998), with $N_{H I} = (7.9 \pm 1.5) \times 10^{20}$ cm^{-2}; this has $T_s = (870 \pm 160) \times (f/0.98)$ K (Lane et al. 1998; Chengalur & Kanekar 1999; Kanekar, Ghosh & Chengalur 2001). Zn II absorption was not conclusively detected in the *HST*-STIS spectrum of Kulkarni et al. (2005), giving [Zn/H] < −0.72. However, these authors did detect Cr II absorption from the DLA, with [Cr/H] = −1.43 ± 0.22. We obtain $\log[N_{Fe II}/\text{cm}^{-2}] > 14.30$ and $\log[N_{Ti II}/\text{cm}^{-2}] < 11.90$ from our Keck-HIRES spectrum, yielding [Fe/H] > −2.05 and [Ti/H] < −1.91.

(xiii) *0800+618, z = 2.9603*: this absorber was detected in the UCSD survey of Jorgenson et al. (2006), with an H I column density of $N_{H I} = (3.16 \pm 0.15) \times 10^{20}$ cm^{-2}. Using this with our covering factor estimate ($f = 0.63$) and our limit on the H I 21 cm optical depth yields $T_s > 570 \times (f/0.63)$ K.

(xiv) *0824+355, z = 2.2433*: the PDLA towards 0824+355 has $N_{H I} = 2 \times 10^{20}$ cm^{-2} (Jorgenson et al. 2006). The VLBA 327 MHz image shows three clear components, apparently a core with an extended jet, and possibly a fourth weak component. We fit a three-component model to the image, obtaining a core covering factor of $f = 0.20$. Our non-detection of H I 21 cm absorption then yields $T_s > 320 \times (f/0.20)$ K.

(xv) *0827+243, z = 0.5247*: this is another DLA from the *HST* sample of Rao & Turnshek (2000), with $N_{H I} = (2.00 \pm 0.18) \times 10^{20}$ cm^{-2}. H I 21 cm absorption was detected in this absorber by Kanekar & Chengalur (2001b) and its covering factor measured

by Kanekar et al. ([2009a](#)); the DLA spin temperature is $T_s = (330 \pm 65) \times (f/0.7)$ K. Kulkarni et al. ([2005](#)) give weak upper limits on the Zn and Cr abundances from their *HST*-STIS non-detections of absorption, with [Zn/H] < -0.04 and [Cr/H] < 0.43. Conversely, detections of Fe II and Mn II absorption in a medium-resolution spectrum (Khare et al. [2004](#)) yielded [Fe/H] $= -1.01 \pm 0.11$ and [Mn/H] $= -0.86 \pm 0.35$ (Chen et al. [2005](#)). Our high-resolution VLT-UVES spectrum gives a slightly higher Fe II column density (albeit consistent within the errors), with [Fe/H] $= -0.91 \pm 0.05$, and also yields [Ti/H] $= -1.39 \pm 0.06$. The DLA metallicity is then [Z/H] $=$ [Fe/H] $+ 0.4 = -0.51 \pm 0.05$.

(xvi) *0913+003, z = 2.7434*: the DLA towards 0913+003 has $N_{\rm H\,I} = (5.5 \pm 1.4) \times 10^{20}$ cm^{-2} (Ellison et al. [2001b](#)) and $f = 0.54$. Our GBT non-detection of H I 21 cm absorption then yields $T_s > 925 \times (f/0.54)$ K.

(xvii) *0952+179, z = 0.2378*: the $z = 0.2378$ DLA towards 0952+179 was detected by Rao & Turnshek ([2000](#)), with $N_{\rm H\,I} = (2.09 \pm 0.24) \times 10^{21}$ cm^{-2}. Kanekar & Chengalur ([2001b](#)) detected H I 21 cm absorption in this absorber, and its covering factor was measured to be $f = 0.66$ by Kanekar et al. ([2009a](#)), giving $T_s = (6470 \pm 965) \times (f/0.66)$ K. Kulkarni et al. ([2005](#)) report an upper limit on the Zn II column density (with [Zn/H] < -1.02) and a detection of Cr II absorption (with [Cr/H] $= -1.64 \pm 0.16$). Our VLT-UVES spectrum yields $\log[N_{\rm Fe\,II}/{\rm cm}^{-2}] = 14.52 \pm 0.03$ and [Fe/H] $= 2.29 \pm 0.06$. This gives a metallicity of [Z/H] $=$ [Fe/H]$+0.4 = -1.89 \pm 0.06$. We also obtain [Ti/H] $= -1.61 \pm 0.07$ and [Mn/H] $= -2.22 \pm 0.07$.

(xviii) *1013+615, z = 2.7670*: Prochaska et al. ([2005](#)) obtain $N_{\rm H\,I} = (4.0 \pm 0.9) \times 10^{20}$ cm^{-2} for this PDLA from an SDSS spectrum [see also Jorgenson et al. ([2006](#)) and Srianand et al. ([2012](#))]. No VLBI studies of this quasar have been carried out at frequencies similar to that of the redshifted H I 21 cm line. While Srianand et al. ([2012](#)) estimate $f = 0.86$, this is from a 1.4 GHz VLBA image. Our GBT non-detection of H I 21 cm absorption yields $T_s > 1100 \times f$ K, about a factor of 1.5 more sensitive than the non-detection of Srianand et al. ([2012](#)).

(xix) *1122−168, z = 0.6819*: the $z = 0.6819$ DLA towards 1122−168 has $N_{\rm H\,I} = (2.82 \pm 0.99) \times 10^{20}$ cm^{-2} (de la Varga et al. [2000](#)). The VLBA image of the background quasar shows at least two components, with a total flux density of ≈ 50 mJy. We identify the more compact component with the quasar core; this has a total 1.4 GHz flux density of 12 mJy, yielding a covering factor of $f \approx 0.04$. If both components are covered by the foreground DLA, the covering factor would be $f \approx 0.17$. Our GBT upper limit to the H I 21 cm optical depth yields $T_s > 100 \times (f/0.04)$ K; the weak limit is due to the extremely low covering factor.

(xx) *1127−145, z = 0.3127*: with $N_{\rm H\,I} = (5.01 \pm 0.92) \times 10^{21}$ cm^{-2} (Rao & Turnshek [2000](#)), this is one of the highest column density DLAs at low redshifts, $z \lesssim 0.5$. H I 21 cm absorption from this DLA was originally detected by Lane et al. ([1998](#)) (see also Kanekar & Chengalur [2001a](#)) and the covering factor measured by Kanekar et al. ([2009a](#)); the DLA spin temperature is $(820 \pm 145) \times (f/0.9)$ K. Our detection of Zn II absorption in the *HST*-STIS spectrum yields $\log[N_{\rm Zn\,II}/{\rm cm}^{-2}] = 13.53 \pm 0.13$ and [Zn/H] $= -0.80 \pm 0.16$. We also obtain $\log[N_{\rm Mn\,II}/{\rm cm}^{-2}] = 13.26 \pm 0.03$ and $\log[N_{\rm Fe\,II}/{\rm cm}^{-2}] > 15.16$, implying [Mn/H] $= -1.92 \pm 0.09$ and [Fe/H] > -2.0, from the VLT-UVES spectrum.

(xxi) *1157+014, z = 1.9436*: H I 21 cm absorption from this DLA was detected by Wolfe et al. ([1981](#)), using the Arecibo telescope. The DLA has an H I column density of $N_{\rm H\,I} = (6.3 \pm 1.5) \times 10^{21}$ cm^{-2} (Wolfe et al. [1981](#); Ledoux et al. [2003](#)) and a covering

factor of $f = 0.63$ (Kanekar et al. [2009a](#)). The new GBT H I 21 cm spectrum, shown in Fig. [1](#)[A], confirms the detection of Wolfe et al. ([1981](#)), although the absorption is significantly weaker in our spectrum. We note, however, that strong out-of-band RFI has been found at the GBT around the redshifted H I 21 cm line frequency (≈ 482.5 MHz); this could imply significant uncertainty in our flux density calibration. We will hence use the original integrated H I 21 cm optical depth of Wolfe et al. ([1981](#)) to estimate the spin temperature; this yields $T_s = (1015 \pm 255) \times (f/0.63)$ K.

(xxii) *1354−170, z = 2.7799*: this DLA has an H I column density of $N_{\rm H\,I} = (2.0 \pm 0.7) \times 10^{20}$ cm^{-2} (Prochaska et al. [2003a](#)) and a covering factor of ≈ 0.97 (this work). Our GBT non-detection of H I absorption then yields $T_s > 1030 \times (f/0.97)$ K.

(xxiii) *1402+044, z = 2.7076*: the H I column density of this DLA is $N_{\rm H\,I} = (1.0 \pm 0.5) \times 10^{21}$ cm^{-2} (Noterdaeme et al. [2009](#); see also Prochaska et al. [2005](#)) and its covering factor is $f = 0.34$ (this work). Combining these with our upper limit on the H I 21 cm optical depth yields $T_s > 890 \times (f/0.34)$ K.

(xxiv) *1418−064, z = 3.4483*: this CORALS DLA has an H I column density of $N_{\rm H\,I} = (2.5 \pm 0.6) \times 10^{20}$ cm^{-2} (Ellison et al. [2001b](#)) and a covering factor of $f = 0.69$ (Kanekar et al. [2009a](#)). Our GMRT non-detection of H I 21 cm absorption then yields $T_s > 930 \times (f/0.69)$ K.

(xxv) *1614+051, z = 2.5200*: this DLA has $N_{\rm H\,I} = 2.5 \times 10^{20}$ cm^{-2} (Storrie-Lombardi & Wolfe [2000](#)), but does not have an estimate of the covering factor; we obtain $T_s > 450 \times f$ K.

(xxvi) *2003−025, z = 1.4106*: this DLA was found by Rao et al. ([2006](#)) in their *HST* survey of strong Mg II λ2796 absorbers, with $N_{\rm H\,I} = (3.5 \pm 1.6) \times 10^{20}$ cm^{-2}. H I 21 cm absorption was later detected in this absorber by Kanekar et al. ([2009b](#)). The VLBA image shows a central core with weak extended emission and a core covering factor of $f = 0.53$; this yields a spin temperature of $T_s = (485 \pm 195) \times (f/0.53)$ K.

(xxvii) *2149+212, z = 0.9115*: the $z = 0.9115$ DLA towards 2149+212 was also found by Rao et al. ([2006](#)). Unfortunately, its very low covering factor ($f = 0.03$) implies that our GBT upper limit on the H I 21 cm optical depth only yields a weak limit on the spin temperature, $T_s > 55 \times (f/0.03)$ K.

(xxviii) *2342+342, z = 2.9082*: this DLA was detected by White et al. ([1993](#)), and has $N_{\rm H\,I} = (1.3 \pm 0.3) \times 10^{21}$ cm^{-2} (Prochaska et al. [2003a](#)) and $f = 0.71$ (Kanekar et al. [2009a](#)). Our GMRT non-detection of H I 21 cm absorption then yields $T_s > 2200 \times (f/0.71)$ K.

6 THE FULL SAMPLE

Including systems from the literature, the full sample of DLAs and sub-DLAs towards 'compact' radio quasars with estimates of the spin temperature via H I 21 cm absorption spectroscopy now contains 60 systems (e.g. Kanekar & Chengalur [2003](#); Ellison et al. [2012](#); Srianand et al. [2012](#); Kanekar et al. [2013](#); this work). This includes six sub-DLAs, with $10^{19} < N_{\rm H\,I} < 2 \times 10^{20}$ cm^{-2}, and seven PDLAs, for which the absorber redshift lies within 3000 km s^{-1} of the quasar redshift. Note that we have excluded DLAs towards extended radio sources e.g. at $z = 0.4369$ towards 3C196 (Brown & Mitchell [1983](#); Briggs, de Bruyn & Vermeulen [2001](#)), $z = 0.5318$ towards 1629+12 (Rao & Turnshek [2000](#); Kanekar & Chengalur [2003](#)) and $z = 0.6561$ towards 3C336 (Rao & Turnshek [2000](#); Curran et al. [2007](#)) from the sample, as the optical and radio sightlines are very different for these sources.

Seven absorbers of the full sample are PDLAs. As noted earlier, spin temperatures in PDLAs are likely to be affected by the proximity of a bright radio source; we will hence exclude these systems from our analysis. The six sub-DLAs are also expected to have systematically higher spin temperatures than DLAs, based on observations in the Galaxy (Kanekar et al. 2011); these too will be excluded from the analysis. For seven DLAs, the lack of covering factor estimates implies that we only have estimates of T_s/f from the H I 21 cm absorption spectroscopy; we will exclude these systems from the following discussion. 37 of the remaining 40 DLAs have covering factor estimates at low frequency (≤ 1.4 GHz) VLBI studies, at frequencies within a factor of ≈ 1.5 of the redshifted H I 21 cm line frequency (e.g. Kanekar et al. 2009a, 2013; Ellison et al. 2012; this work). The covering factor estimates are likely to be reliable in these cases. However, for three absorbers at $z > 2$, the VLBI images are at 1.4 GHz, more than a factor of 3 larger than the redshifted H I 21 cm line frequency (Srianand et al. 2012; Kanekar et al. 2013). Compact radio cores are likely to have an inverted spectrum (due to synchrotron self-absorption), while extended radio structure is expected to have a steep spectrum. As a result, measurements of the covering factor at a significantly higher frequency than the line frequency could overestimate the covering factor, and hence underestimate the spin temperature. We will hence also exclude these three systems from our analysis, ending with 37 bona fide DLAs towards compact background quasars with covering factor measurements close to the redshifted H I 21 cm line frequency.

Our final sample of 37 absorbers contains 19 detections of H I 21 cm absorption, nine at $z < 1$, five at $1 < z < 2$, four at $2 < z < 3$ and one at $z > 3$. Of the 18 remaining systems with non-detections of H I 21 cm absorption, 14 have strong lower limits on the spin temperature, $T_s > 500$ K, while 4 have weak lower limits, $T_s > 55-270$ K. We emphasize that all systems of the sample have estimates of the DLA covering factor from low-frequency VLBI studies. These covering factor estimates have been used to derive the DLA spin temperatures.

Detailed information on various properties of the absorbers of the full sample is provided in Tables 4 and 5. The 37 absorbers constituting our final sample are listed in Table 4, while Table 5 contains the 23 excluded systems: (1) the seven PDLAs, (2) the six sub-DLAs, (3) the three DLAs with estimates of f at frequencies >1.5 times the redshifted H I 21 cm line frequency and (4) the seven DLAs with no covering factor estimates. The columns of both tables contain (1) the quasar name, (2) the quasar emission redshift, (3) the DLA absorption redshift, (4) the H I column density and error, (5) the covering factor (i.e. the quasar core fraction at low frequencies), (6) the spin temperature or lower limits to T_s, after correcting for the absorber covering factor, (7) the metallicity [Z/H], (8) Z, the element used for the metallicity estimate, (9) the dust depletion [Z/Fe], (10) 'Dust', the element used for the dust abundance, (11) the velocity spread of the low-ionization metal lines, between 90 per cent optical depth points, ΔV_{90}, in km s^{-1} (Prochaska & Wolfe 1997), (12) the metal-line transition on which the ΔV_{90} estimate is based, and (13) references for the H I column density, spin temperature, abundances and ΔV_{90} values. The metallicities are relative to the solar abundance, on the scale of Asplund et al. (2009). Following Prochaska et al. (2003b), we have used, in order of preference, [Z/H] $\equiv$ [Zn/H], [S/H], [Si/H] and [Fe/H]+0.4, except for the $z = 0.524$ DLA towards AO0235+164, where the metallicity is from an X-ray measurement (Junkkarinen et al. 2004). Most of the ΔV_{90} estimates are from our own Keck-HIRES or VLT-UVES high-resolution echelle spectra.

7 RESULTS AND DISCUSSION

7.1 The present T_s sample and the general DLA population

Before proceeding with a discussion of the various properties of our final sample of DLAs, it is relevant to test whether the sample is representative of the known DLA population, so that inferences drawn from the former can be applied to the latter. Since the defining property of a DLA is its H I column density, we compared the distribution of $N_{H I}$ values in our sample with those of the general DLA population. The comparison sample was made up of 1080 DLAs drawn from a variety of surveys (Storrie-Lombardi & Wolfe 2000; Ellison et al. 2001b; Prochaska et al. 2005; Jorgenson et al. 2006; Rao et al. 2006; Noterdaeme et al. 2009). The distributions of $N_{H I}$ values in the two samples are shown in Fig. 11[A], where the fraction of DLAs plotted on the y-axis has been normalized by the total number of DLAs in each sample to allow for a direct comparison between the two distributions. A similar plot in Fig. 11[B] compares the $N_{H I}$ distributions in the high-z and low-z DLA samples.

While the fraction of high-$N_{H I}$ DLAs appears to be larger in the H I 21 cm sample, the number of absorbers in this sample is quite small (37 systems), implying large fluctuations from Poisson statistics. The literature sample is dominated by the SDSS DLAs, at $z \geq 2.2$; conversely, the median absorber redshift in our sample is $z_{med} = 2.192$, so our sample contains a significantly higher fraction of low-z DLAs than the literature sample (e.g. ≈ 40 per cent at $z < 1.5$ in our sample, against ≈ 3 per cent for the literature sample). While the samples have different redshift distributions, a number of studies have found no evidence for redshift evolution in the H I column density distribution function (e.g. Prochaska et al. 2005; Zwaan et al. 2005). We find that the $N_{H I}$ distributions of our sample and the literature DLAs agree within 1.8σ significance in a Wilcoxon two-sample test.[4] We hence conclude that there is no statistically significant evidence against the null hypothesis that the DLAs of our sample are representative of the general DLA population.

7.2 The covering factor

It has been suggested by Curran & Webb (2006) (see also Curran 2012) that unknown covering factors are the main cause of the high spin temperature estimates in high-z DLAs. These authors argue that this is due to a geometric effect, owing to the fact that the angular diameter distances of absorbers at $z \gtrsim 1$ are comparable to those of the background quasars (at $z > 1$), implying that higher redshift absorbers are 'less efficient' at obscuring the background radio emission and hence have lower covering factors. While this may or may not be applicable for systems which do not have estimates of the low-frequency covering factor f, all 37 DLAs of our sample have estimates of the covering factor at frequencies within a factor of 1.5 of the redshifted H I 21 cm line frequency. The estimated covering factors are plotted versus redshift in Fig. 12[A]: no evidence was found for a difference between the distributions of covering factors for the sub-samples of absorbers with $z < z_{med}$ and $z > z_{med}$ (note that $z_{med} = 2.192$); the distributions agree within 0.7σ significance in a Wilcoxon two-sample test.

Fig. 12[B] plots the upper limit to the spatial extent of the core radio emission at the DLA redshift versus the DLA redshift. While the spatial extent does appear to be larger at high redshifts, it should

---

[4] The statistical tests described here were mostly carried out using the Astronomical Survival analysis ASURV package (Isobe, Feigelson & Nelson 1986).
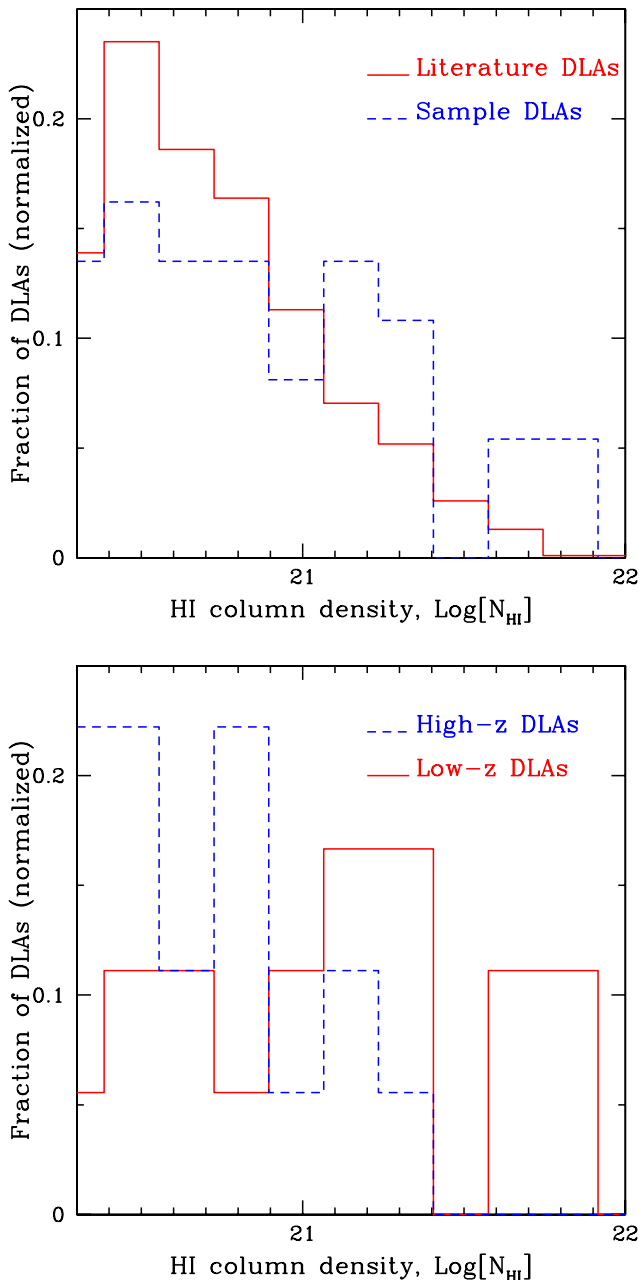
Figure 11. [A] Top panel: histograms of the distribution of the $N_{H I}$ values of the 37 DLAs of our sample and of a sample of 1080 DLAs from a number of surveys in the literature. A Wilcoxon two-sample test finds no statistically significant evidence against the hypothesis that the sample DLAs are drawn from the general population; see the main text for discussion. [B] Bottom panel: histograms of the distributions of the $N_{H I}$ values of the low-z (solid) and high-z (dashed) DLA sub-samples, separated at the median redshift $z = 2.192$. A Wilcoxon two-sample test finds that the two $N_{H I}$ distributions are different at $\approx 2.7\sigma$ significance.

be emphasized that the core spatial extents plotted in Fig. 12[B] are *upper limits*, due to the possibility of residual phase errors in the VLBA data. This issue is especially important at low frequencies (327 and 606 MHz), due to ionospheric effects. As a result, the size estimates of Fig. 12[B] are systematically larger for the DLAs at $z \gtrsim 2$, as these were all observed with the 327 MHz VLBA receivers.

Fig. 12[B] shows that the background radio cores have a transverse size of $\lesssim 1$ kpc at the absorber redshift in 36 of the 37 ab-

sorbers, significantly smaller than the size of even dwarf galaxies. For DLAs at $z > 2$, the median upper limit (due to the possibility of residual phase errors) to the transverse size of the core emission is ≈ 350 pc. This indicates that the radio cores are likely to be entirely covered by all the foreground absorbers. The sole exception is 0458−020, where the agreement between VLBI and single-dish H I 21 cm absorption profiles led Briggs et al. (1989) to argue that the $z = 2.0395$ DLA covers both the radio core and the extended lobes, implying an absorber size $\gtrsim 16$ kpc; note that this system lies off the scale in Fig. 12[B].

We also examined whether the probability of detecting H I 21 cm absorption or the estimated spin temperatures depend on the absorber covering factors. Fig. 13 plots the spin temperature versus covering factor for the 37 DLAs of the sample. The median covering factor of the absorbers in the sample is $f_{med} = 0.64$. For sightlines with $f > f_{med}$, there are 12 detections and 5 non-detections of H I 21 cm absorption, while sightlines with $f < f_{med}$ have 7 detections and 11 non-detections. The detection probabilities are 71^{+27}_{-20} per cent for the high-f sample and 37^{+20}_{-13} per cent for the low-f sample.[5] Thus, while the detection rate appears to be higher for the high-f sample (as would be expected on physical grounds), the difference is not statistically significant (agreeing within $\approx 1.2\sigma$ significance) in the current sample. Similarly, a Peto–Prentice generalized Wilcoxon two-sample test (for censored data) finds no evidence for a difference between the distributions of T_s values for the high-f and low-f samples; the two T_s distributions agree within 0.1σ significance. We thus find no statistically significant evidence that the probability of detecting H I 21 cm absorption or the spin temperature estimates depend on the absorber covering factor.

The fact that we do not detect a significant dependence of the detection rate of H I 21 cm absorption on the covering factor may appear surprising. This is likely to be at least partly due to the fact that the sample is still relatively small, with only ≈ 18 systems apiece in the high-f and low-f sub-samples. Further, the sensitivity to H I 21 cm absorption is not uniform across the sample: the optical depth sensitivity is typically better for brighter background sources.

We will revisit the arguments of Curran & Webb (2006) regarding angular diameter distances in Section 7.6.

7.3 Differing H I columns along optical and radio sightlines

As noted in Section 3, a critical assumption in estimating spin temperatures in DLAs is that the H I column densities measured from the damped Lyman α profile can be used in equation (3), i.e. that the $N_{H I}$ values along the optical and radio sightlines are the same. If the H I columns are systematically different along the radio and the optical sightlines (e.g. if there is significant spatial structure in the H I distribution), it would lead to systematic errors in the derived spin temperatures. For example, Wolfe, Gawiser & Prochaska (2003b) suggest that the average H I column towards the radio core of 0201+113 may be significantly lower than that towards

---

[5] The quoted errors are 1σ Gaussian confidence intervals, based on small-number Poisson statistics (Gehrels 1986). Note that the error does not scale linearly with confidence interval, e.g. the 2σ lower confidence interval is not twice the 1σ lower confidence interval, and care is hence needed while comparing detection rates for different sub-samples. In all cases, we have used two approaches to test whether the detection rates for different sub-samples are in agreement: (1) naively assuming that the errors scale linearly with confidence interval, and (2) checking whether the 2σ confidence intervals of the detection rates of the sub-samples overlap with each other. The quoted differences in the detection rates are from the first approach.
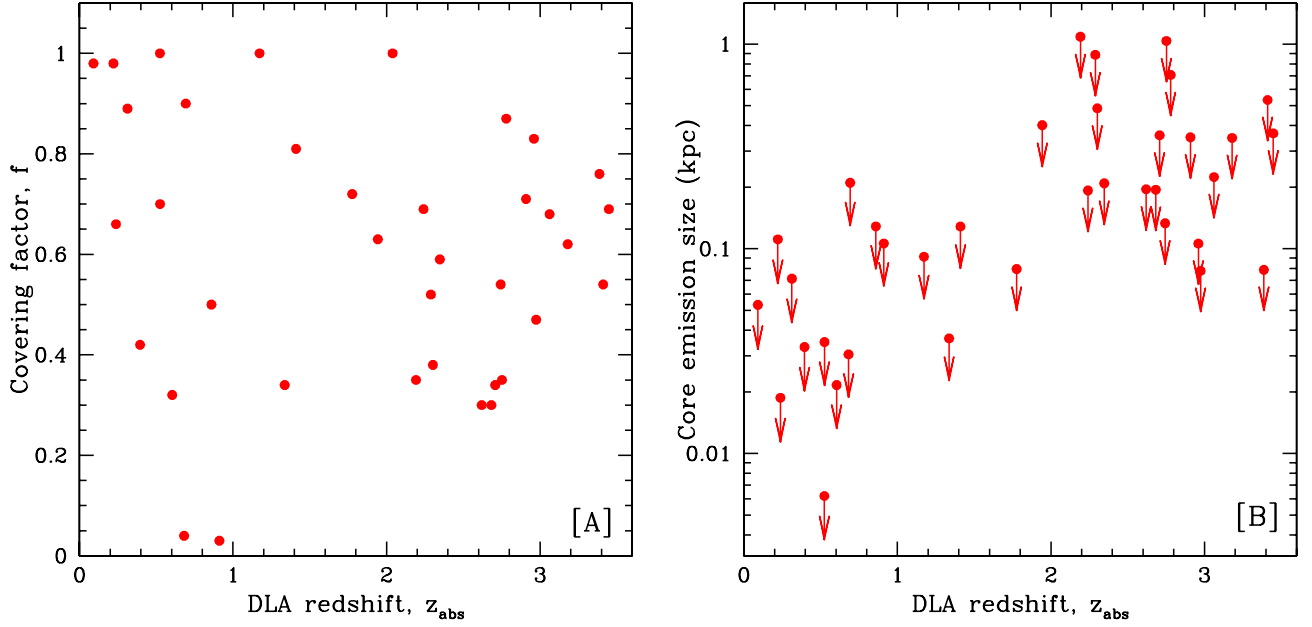
Figure 12. [A] Left-hand panel: the covering factors of the 37 DLAs of the full sample, plotted against absorber redshift, z_{abs}. No difference is apparent between the distributions of covering factors above and below the median redshift, $z_{med} = 2.192$. [B] Right-hand panel: the spatial extent of the compact radio emission of the background quasars (at the DLA redshift), plotted against z_{abs}. Note that each point is an upper limit to the size of the radio emission, due to the possibility of residual phase errors in the VLBA data. The points have hence been shown with downward-pointing arrows. As a result, the limits are much poorer for the DLAs at $z \gtrsim 2$, as all these systems were observed with the VLBA at 327 MHz, where the ionospheric activity is significantly worse than at higher frequencies. Despite this, the upper limit to the core size is $\lesssim 1$ kpc in 36 out of the 37 DLAs of the sample.
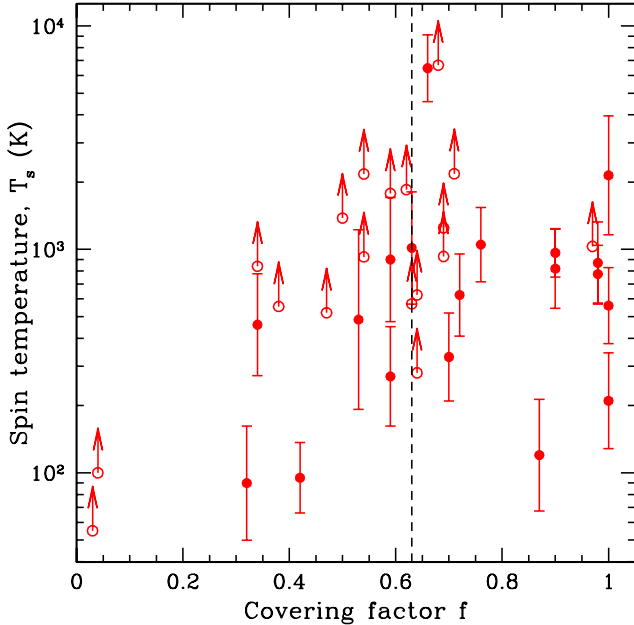
Figure 13. The spin temperature T_s plotted against the covering factor for the 37 DLAs of the sample; non-detections of H I 21 cm absorption are indicated by lower limits to the spin temperature. The median covering factor $f_{med} = 0.63$ is indicated by the vertical dashed line. No evidence was found that either the detection probability or the spin temperature depends on the absorber covering factor.

the optical quasar, thus resulting in an incorrectly high estimate of the spin temperature. Note that this effect is not the same as the issue of the geometric covering factor discussed in the preceding section, although the two are often confused in the literature.

Absorption spectroscopy of lensed quasars provides an interesting tool to measure H I column density along multiple sightlines through a DLA, and to thus test for structure in the H I distribution (e.g. Smette et al. 1995; Zuo et al. 1997; Lopez et al. 2005; Monier, Turnshek & Rao 2009). For example, Smette et al. (1995) measured H I column densities of $\log[N_{H I}/cm^{-2}] = 20.6$ and $\log[N_{H I}/cm^{-2}] = 17.6$ at $z = 1.6616$ towards images A and B of quasar HE 1104−1805, respectively, at a separation of ≈ 3 arcsec (≈ 26 kpc at the redshift). Conversely, Lopez et al. (2005) found the H I column densities in a $z = 0.9313$ galaxy towards images A and B of the quasar HE 0552−3315 to be in excellent agreement, at a separation of 0.644 arcsec (≈ 5.2 kpc at the absorber redshift). Unfortunately, there are as yet only a handful of DLAs known towards lensed quasars.

The most direct way of testing whether the H I columns are different along the radio and optical sightlines is to compare H I column densities measured from pencil-beam (i.e. UV or optical) studies and studies at coarser angular resolution. This has been done in the Galaxy (Dickey & Lockman 1990; Wakker, Lockman & Brown 2011), by comparing $N_{H I}$ values obtained at the same or neighbouring locations from Lyman α absorption studies of background quasars and H I 21 cm emission studies. Wakker et al. (2011) carried out such a comparison along 59 sightlines, using *HST*-STIS Lyman α absorption spectra and H I 21 cm emission spectra at angular resolutions of 9–36 arcmin from the GBT and the 140 ft telescope. For the former, the $N_{H I}$ values were derived from the usual Voigt profile fits to the damping wings of the Lyman α line, as is done for high-z DLAs. For the latter, the $N_{H I}$ values were inferred under the assumption that the H I 21 cm emission is optically thin, in which case the observed H I 21 cm emission brightness temperature is directly proportional to the H I column density (Rohlfs & Wilson 2006). Wakker et al. (2011) found the H I column densities obtained from the two methods to be in excellent agreement, with the ratio

having a mean value of unity and a dispersion of 10 per cent. Note that one does not know the distance to the absorbing clouds, and hence cannot estimate the spatial resolution of the H I 21 cm emission spectra. If the clouds are at an average distance of ≈ 1 kpc, it would imply that the H I column density averaged over regions of size ≈ 10 pc is similar to that on scales of 100–1000 au.

Similarly, Welty, Xue & Wong (2012) compared H I column densities in the Large Magellanic Cloud (LMC) measured from the Lyman α absorption profile towards stars in the LMC and H I 21 cm emission spectroscopy at a spatial resolution of 15 pc. They found good agreement between the $N_{H I}$ values by excluding H I 21 cm emission from gas lying behind the stars (based on the emission velocity). This too indicates that the H I column density on scales of ≈ 100–1000 au is similar to that on scales of ≈ 15 pc.

However, Fig. 12[B] shows that the spatial extent subtended by the radio core at the DLA redshift may be significantly larger than 10 pc, with a median value of ≈ 350 pc for DLAs at $z > 2$. Although, as noted in the preceding section, these transverse sizes are upper limits, most of the background quasars are likely to have radio cores of spatial extent greater than a few tens of parsecs at the redshift of the foreground DLA (see Wolfe et al. 2003b for the $z = 3.387$ DLA towards 0201+113). This is because the angular size of the radio core must be sufficiently large at low frequencies to have a brightness temperature lower than either the equipartition limit or the inverse Compton limit ($\approx 10^{11}$–10^{12} K; Kellermann & Pauliny-Toth 1969; Readhead 1994; Singal 2009), unless the radio emission is relativistically beamed towards us. Relativistic beaming is unlikely to be important for most of the background quasars of our sample, as few of them have highly variable flux densities. Thus, for most of the absorbers of the sample, the radio core emission is likely to subtend a transverse size of tens of pc, and perhaps as large as a few hundred pc, at the DLA redshift.

One thus has to hence examine whether the H I column density averaged over spatial scales of a few hundred pc is systematically different from that measured along a pencil beam. A direct comparison between the H I column densities measured from the Lyman α line and from H I 21 cm emission has so far been carried out in a single DLA, at $z = 0.009$ towards SBS 1549+593 (Bowen, Tripp & Jenkins 2001). For this system, Chengalur & Kanekar (2002) measured $N_{H I} \approx (4.9 \pm 0.6) \times 10^{20}$ cm^{-2} from a GMRT H I 21 cm emission study with a spatial resolution of ≈ 5.3 kpc at the DLA redshift, while Bowen et al. (2001) obtained a slightly lower value, $N_{H I} \sim (2.2 \pm 0.5) \times 10^{20}$ cm^{-2}, from the damped Lyman α profile (albeit with unknown systematic errors due to the extended wings of the STIS G140L grating line spread function and blending with the Lyman α line of the Galaxy; Bowen et al. 2001). Note that the spatial resolution of the H I 21 cm study here is far larger than the typical transverse scale subtended by the radio cores at the redshifts of the DLAs of our sample.

An alternative approach is to compare the H I column density measured at high spatial resolution along sightlines in an H I 21 cm emission cube of a nearby galaxy with the $N_{H I}$ values obtained along the same sightlines on smoothing the cube to lower spatial resolutions. Such a comparison was carried out by Ryan-Weber, Staveley-Smith & Webster (2005), between $N_{H I}$ values measured at 15 pc and 3.6 kpc resolution. These authors found that the fine structure – at both low and high column densities – is washed out on smoothing to 3.6 kpc resolution, resulting in sightlines with original $N_{H I}$ values in the sub-DLA regime returning higher values and gas with $N_{H I} > 10^{21}$ cm^{-2} yielding values with $N_{H I} < 10^{21}$ cm^{-2}.

We follow the same approach as Ryan-Weber et al. (2005), analysing a high-spatial-resolution H I 21 cm emission image of
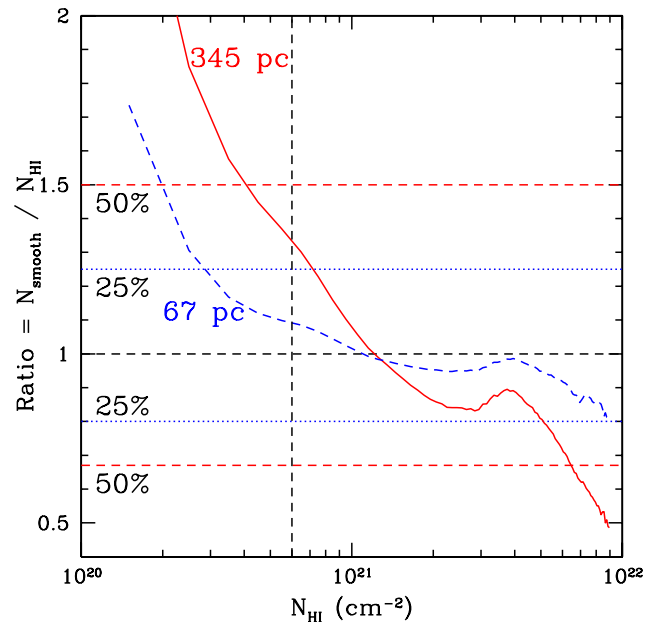
Figure 14. H I in the LMC: the ratio of the smoothed H I column density N_{smooth} at spatial resolutions of 67 pc (dashed curve) and 345 pc (solid curve) to the H I column density at the original (15 pc) resolution $N_{H I}$ plotted versus $N_{H I}$. The horizontal dotted and dashed lines, respectively, demarcate regions where the ratio is within 25 and 50 per cent of unity. The dashed vertical line indicates $N_{H I} = 6 \times 10^{20}$ cm^{-2}, the median H I column density of the DLA sample.

the LMC, obtained by combining data from the Australia Telescope Compact Array and the Parkes multibeam receiver (Kim et al. 2003). The spectral cube has a spatial resolution of ≈ 15 pc at the distance of the LMC. We have smoothed the cube to different spatial resolutions, up to a maximum of 1 kpc, and measured the H I column density at the same position at each resolution, assuming the H I 21 cm emission to be optically thin in all cases. Finally, we averaged the results from different spatial locations with the same value of the original, unsmoothed H I column density, using uniform $N_{H I}$ bins.

The results are shown in Fig. 14, which plots the ratio of the H I column density measured at two different spatial resolutions (67 and 345 pc) to that at the original resolution (15 pc) versus the unsmoothed $N_{H I}$. These spatial resolutions were chosen because the median transverse sizes of quasar radio cores at the absorber redshift are ≈ 70 and ≈ 350 pc for DLAs at $z < 2$ and $z > 2$, respectively, allowing a direct comparison.

It is clear that the behaviour depends on the absolute value of the H I column density: at both smoothed resolutions, the ratio is larger than unity (i.e. the smoothed H I column density is larger than the original) for $N_{H I} \lesssim 10^{21}$ cm^{-2}, and lower than unity (i.e. the smoothed $N_{H I}$ is lower than the original) for $N_{H I} \gtrsim 10^{21}$ cm^{-2}. However, smoothing to a resolution of ≈ 67 pc does not significantly alter the H I column density over most of the range: the mean value of the ratio is within ≈ 10 per cent of unity for $5.0 \times 10^{20} < N_{H I} < 6.3 \times 10^{21}$ cm^{-2}. Even for $2 \times 10^{20} < N_{H I} < 5 \times 10^{20}$ cm^{-2}, the ratio is <1.5.

The situation is similar in the case of smoothing to a spatial resolution of 345 pc, although with somewhat larger deviations from unity. Here, the ratio is within 25 per cent of unity for $N_{H I} = (0.7$–$5.1) \times 10^{21}$ cm^{-2}, within 50 per cent of unity over the

ranges $N_{\rm H\,I} = (5.1$–$6.5) \times 10^{21}$ and $(4$–$7) \times 10^{20}$ cm^{-2}, and lower than 2 for $N_{\rm H\,I} = (2$–$4) \times 10^{20}$ cm^{-2}.

The above results can be used to draw inferences about the derived spin temperatures in DLAs, assuming that the spatial distribution of H I in DLAs is similar to that in the LMC. From the above results, using the H I column density measured from the damped Lyman α profile in the equation for the H I 21 cm optical depth to derive the spin temperature would not result in a *systematically higher or lower* $T_{\rm s}$ estimate in all DLAs. The spin temperature would be slightly underestimated for DLAs with $N_{\rm H\,I} < 1 \times 10^{21}$ cm^{-2} and overestimated for DLAs with $N_{\rm H\,I} > 1 \times 10^{21}$ cm^{-2}.

All DLAs of the sample have H I column densities in the range 2×10^{20}–6.3×10^{21} cm^{-2}. For absorbers at $z < 2$ (where the median transverse size of the radio core is ≈ 69 pc), the derived spin temperature would be within 10 per cent of the 'true' value for all $N_{\rm H\,I}$ values except the range $2 \times 10^{20} < N_{\rm H\,I} < 5 \times 10^{20}$ cm^{-2}, where the derived $T_{\rm s}$ could be lower than the 'true' value by up to a factor of 1.5. Conversely, for DLAs at $z > 2$ (where the median transverse size of the radio core is ≈ 350 pc), the derived $T_{\rm s}$ would be within 50 per cent of the correct value for all $N_{\rm H\,I}$ values except for the range $N_{\rm H\,I} = (2$–$4) \times 10^{20}$ cm^{-2}. For the latter range, the $T_{\rm s}$ estimate could be lower than the 'true' value by up to a factor of 2.

The median H I column density of the present DLA sample is $N_{\rm H\,I} \approx 6 \times 10^{20}$ cm^{-2}, with 23 absorbers having $N_{\rm H\,I} \leq 1 \times 10^{21}$ cm^{-2}. Of the remaining 14 systems, 12 have $N_{\rm H\,I} < 5.1 \times 10^{21}$ cm^{-2} and should thus, on the average, have systematic errors lower than 25 per cent on the spin temperature. There are thus only two absorbers, at $z = 1.9436$ towards 1157+014 and $z = 2.0395$ towards 0458−020, whose H I column densities are in the regime where the spin temperature might be overestimated by ≈ 50 per cent. Conversely, there are 10 DLAs in the sample with $N_{\rm H\,I} < 4 \times 10^{20}$ cm^{-2}, 7 of which are at $z > 2$, for which the spin temperature could be underestimated, on the average, by using the optical $N_{\rm H\,I}$ in equation (3).

For clarity, we emphasize that the above statements are only valid in a statistical sense; it is certainly possible that the H I column densities along the radio and optical sightlines are very different in individual absorbers. However, on the average, the use of the H I column density derived from the Lyman α profile is likely to result in *underestimating* the spin temperature for most DLAs of the present sample, by up to a factor of 2 at the lowest H I column densities. The spin temperature is likely to be overestimated for only a few DLAs with the highest $N_{\rm H\,I}$ values, $N_{\rm H\,I} > 5 \times 10^{21}$ cm^{-2}.

7.4 H I 21 cm optical depths, DLA spin temperatures and H I column densities

It is well known that the strength of the H I 21 cm absorption in the Galaxy and M31 shows a rough power-law dependence on the H I column density (e.g. Braun & Walterbos 1992; Carilli et al. 1996; Kanekar et al. 2011). A similar trend has been seen in earlier studies of DLAs, using smaller samples and without covering factor measurements (Carilli et al. 1996; Kanekar & Chengalur 2001b). For the current sample of 37 DLAs, Fig. 15[A] shows the integrated H I 21 cm optical depth ($\int \tau_{\rm 21\,cm} dV$), corrected for the absorber covering factor, plotted against the H I column density $N_{\rm H\,I}$. It is clear that the strength of the H I 21 cm absorption does correlate with $N_{\rm H\,I}$; the correlation is detected at $\approx 3.8\sigma$ significance in a non-parametric generalized Kendall-tau test (Brown, Hollander & Korwar 1974; Isobe et al. 1986).

Fig. 15[B] shows the spin temperature plotted versus H I column density for the 37 DLAs of the sample; no evidence is seen for a relation between the two quantities. We further tested whether the DLA spin temperatures are systematically different in absorbers with low and high H I column densities, below and above the median $N_{\rm H\,I} \approx 6 \times 10^{20}$ cm^{-2}. A Peto–Prentice test finds that the spin temperature distributions of the sub-samples with $N_{\rm H\,I}$ values above and below the median are in agreement within $\approx 0.8\sigma$ significance.
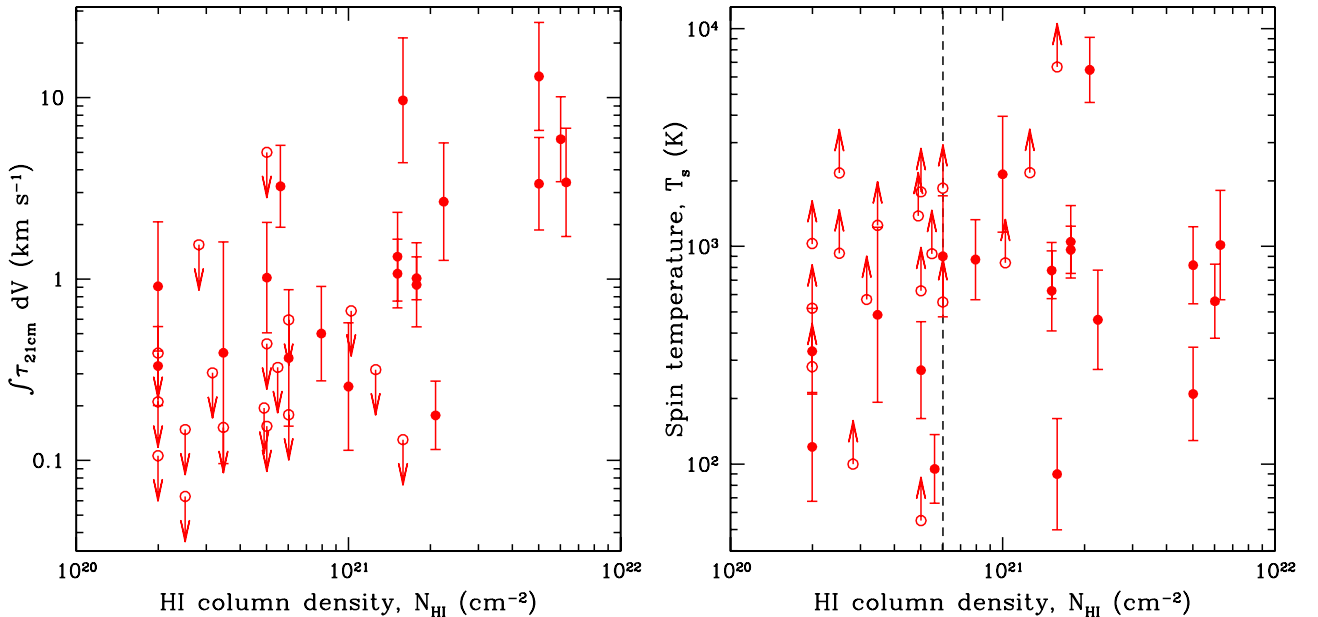
Figure 15. [A] Left-hand panel: the integrated H I 21 cm optical depth $\int \tau_{\rm 21\,cm} dV$, corrected for the DLA covering factor. [B] Right-hand panel: the spin temperature $T_{\rm s}$, plotted against the H I column density $N_{\rm H\,I}$ for the 37 DLAs of the sample. Non-detections of H I 21 cm absorption are plotted as open circles, with arrows indicating upper limits to the H I 21 cm optical depth and lower limits to the spin temperature. The dashed vertical line in the right-hand panel indicates the median value of the H I column density, $N_{\rm H\,I} \approx 6 \times 10^{20}$ cm^{-2}. See the text for discussion.

We also considered the possibility that the N_{HI} values along the radio and optical sightlines might be somewhat different at low and high HI column densities, as inferred from the results in Section 7.3 for the LMC. This was done by using the ratio of the HI column densities measured along the high resolution and the smoothed sightlines in the LMC (from Fig. 14) to convert the measured N_{HI} values towards the optical QSO to that towards the radio core. For DLAs at $z < 2$ and $z > 2$, we used the ratios measured at smoothed resolutions of 67 and 345 pc, respectively, in each case equal to the median size of the core at the DLA redshift. We also corrected the spin temperature for the new N_{HI} value. Again, no significant difference was obtained in the spin temperature distributions for the sub-samples with low and high HI column densities; the distributions agree at 1.4σ significance in a Peto–Prentice test.

We thus find no evidence that DLA spin temperatures have a systematic dependence on the HI column density (see also Srianand et al. 2012). Note that the spin temperatures of the Galactic sample also do not show a statistically significant dependence on the HI column density: a similar Peto–Prentice test finds that the Galactic spin temperature distributions above and below the median HI column density (1.48×10^{21} cm^{-2}) are in agreement within $\approx 1.3\sigma$ significance.

In order to consider whether the detection rate of HI 21 cm absorption depends on the HI column density, we restricted the sample to the 34 DLAs with either detections of HI 21 cm absorption or strong lower limits on the spin temperature ($T_s > 500$ K). This was done to avoid the possibility that our conclusions might be biased by DLAs with weak limits on the HI 21 cm optical depth. The median HI column density of this sub-sample is $N_{HI} = 6 \times 10^{20}$ cm^{-2}. The detection rates of HI 21 cm absorption are $\approx 81^{+19}_{-22}$ and $\approx 33^{+23}_{-14}$ per cent for absorbers with HI column densities higher and lower than 6×10^{20} cm^{-2}, respectively. While the detection rate appears to be higher in the high-N_{HI} sample, the difference has only 1.3σ significance. At present, we find no statistically significant evidence that the detection rate of HI 21 cm absorption in DLAs depends on the HI column density (although we note that this too might arise due to the relatively small size of the two sub-samples).

7.5 Redshift evolution of DLA spin temperatures

The high spin temperatures obtained in DLAs have been an issue of interest ever since the earliest studies of HI 21 cm absorption in high-z DLAs (Wolfe & Davis 1979; Wolfe et al. 1981). There are two separate questions here: (1) whether DLA spin temperatures are systematically different from those measured in the Milky Way and local spiral galaxies, and (2) whether DLA spin temperatures evolve with redshift (i.e. whether low-z and high-z DLAs have different distributions of spin temperatures). While a number of studies have indicated that high-z DLAs tend to have higher spin temperatures than those seen in both low-z DLAs and the Galaxy (e.g. Carilli et al. 1996; Chengalur & Kanekar 2000; Kanekar & Chengalur 2001b, 2003; Srianand et al. 2012), the results have been uncertain due to a combination of small sample size and lack of covering factor measurements.

Fig. 16 shows the spin temperature plotted versus redshift for the 37 DLAs of our sample; the median absorber redshift is $z_{med} = 2.192$. We emphasize that all systems have estimates of the absorber covering factor and that this is by far the largest sample that has been used for such studies. There are 3 detections and 15 non-detections of HI 21 cm absorption in DLAs at $z > 2.192$, and 15
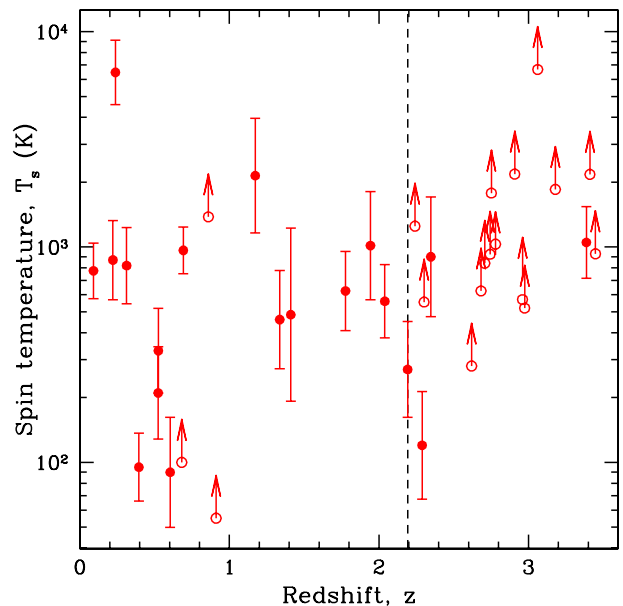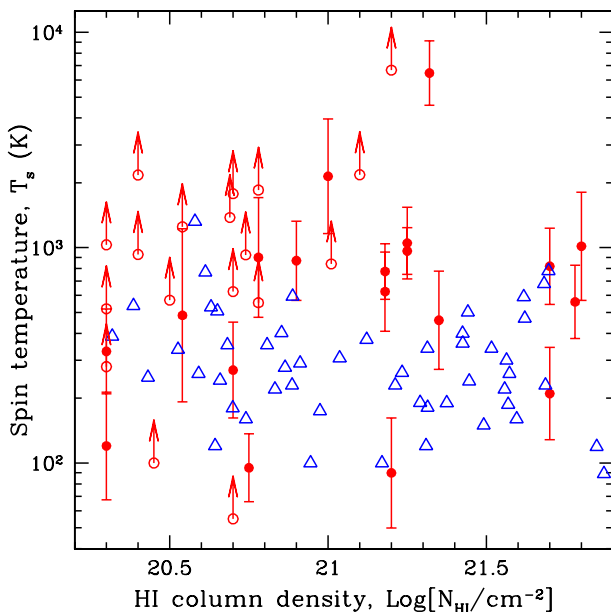

Figure 16. The spin temperature T_s plotted against redshift for the 39 DLAs (filled circles) and sub-DLAs (open stars) of the sample; non-detections of HI 21 cm absorption are indicated by lower limits to the spin temperature. The median absorption redshift, $z_{med} = 2.192$, is indicated by the vertical dashed line. A generalized Wilcoxon two-sample test finds that the distributions of spin temperatures are different in the high-z and low-z samples; see the text for discussion.

detections and 3 non-detections of HI 21 cm absorption in systems at $z < 2.192$. The detection fractions are (17^{+16}_{-9}) per cent ($z > 2.192$) and (83^{+17}_{-21}) per cent ($z < 2.192$). The detection fraction thus appears to be higher in the low-z sample, albeit only at $\approx 2.5\sigma$ significance (see also Kanekar et al. 2009b). However, a comparison between the two spin temperature distributions via a Peto–Prentice test finds that the T_s distributions are different at $\approx 3.5\sigma$ significance. Note that there is nothing special about the median redshift, $z = 2.192$, chosen to demarcate the high-z and low-z DLA sub-samples. For example, a comparison between the T_s distributions of absorber at redshifts above and below $z = 2.4$ (23 systems in the low-z sample and 14 in the high-z sample) yields a difference with 4.0σ statistical significance. We conclude that there is statistically significant evidence for evolution in the spin temperatures of DLAs from high redshifts to low redshifts, with a larger fraction of low-T_s DLAs in the low-redshift sample as well as a higher detection fraction at low redshifts.

It should be mentioned that DLAs in the low-z and high-z samples were not gathered via the same selection criteria. Most of the DLAs in the low-z sample were initially targeted due to the presence of strong Mg II $\lambda 2796$ absorption in the quasar spectrum, with follow-up Lyman α spectroscopy resulting in the detection of the DLA (e.g. Rao & Turnshek 1998, 2000; Rao et al. 2006; Ellison et al. 2012). Conversely, DLAs in the high-z sample were obtained from direct absorption surveys in the Lyman α absorption line. While the Mg II $\lambda 2796$ rest equivalent width is correlated with the absorber metallicity (Murphy et al. 2007), there is no evidence that the Mg II $\lambda 2796$ selection criterion (at an Mg II $\lambda 2796$ rest equivalent width threshold of 0.5 Å; Rao et al. 2006) preferentially yields DLAs with higher metallicity. It thus appears unlikely that the different selection methods could give rise to differing spin temperature distributions in the low-z and high-z samples.

The distributions of H I column densities of the low-z and high-z DLA samples (again separated at the median redshift, $z = 2.192$) do show a weak difference in a Wilcoxon two-sample test (at $\approx 2.7\sigma$ significance). Histograms of the $N_{\rm H I}$ distributions of the low-z and high-z sub-samples are plotted in Fig. 11[B]. While it should be noted that the sizes of the two sub-samples are small (with only 18 systems in each sub-sample), there appear to be more high-$N_{\rm H I}$ DLAs in the low-z sub-sample and more low-$N_{\rm H I}$ DLAs in the high-z sub-sample. Since the strength of the H I 21 cm absorption correlates with the H I column density, this could contribute to the larger fraction of detections of H I 21 cm absorption in the low-z sample. However, this would be the case only if the H I 21 cm studies were carried out at uniform optical depth sensitivity. In reality, the H I 21 cm absorption studies have been targeted at detecting gas at high spin temperatures, by aiming for higher optical depth sensitivity in DLAs with lower H I column densities. It thus appears unlikely that the difference in H I column density distributions in the low-z and high-z DLA samples significantly influences the detection rates of H I 21 cm absorption. Of course, it was shown in Section 7.4 that the spin temperature does not correlate with the H I column density, either in DLAs or in the Galaxy. The difference in H I column density distributions should hence also not yield a difference in the spin temperature distributions of the high-z and low-z samples.

Fig. 17 shows the spin temperatures of the 37 DLAs of the sample (filled circles) and the $T_{\rm s}$ values measured along 51 Galactic sightlines towards compact radio sources with $N_{\rm H I} \geq 2 \times 10^{20}$ cm^{-2} (open triangles) plotted versus H I column density; the Galactic data are from Colgan, Salpeter & Terzian ([1988](#)) and Kanekar et al. ([2011](#)). As was originally pointed out by Carilli et al. ([1996](#)) (albeit for integrated H I 21 cm optical depths), the majority of the DLAs lie at or above the upper edge of the distribution of the Galactic $T_{\rm s}$ values. While the H I column densities of the two samples are consistent with being drawn from the same distribution, a Peto–Prentice test finds that the distributions of spin temperatures in DLAs and the Galaxy are different at $\approx 6.0\sigma$ significance. We conclude that there is clear evidence that conditions in the neutral ISM in DLAs are very distinct from those measured along sightlines through the Galaxy, with significantly higher spin temperatures in most DLAs than are observed in the Milky Way.

7.6 Spin temperature or covering factor as the cause for $T_{\rm s}$ evolution?

Curran & Webb ([2006](#)) have argued that the apparent difference in spin temperature distributions between low-z and high-z DLA samples arises mainly due to covering factor effects (see also Curran [2012](#)). These authors argue that high-z DLAs are inefficient at covering the quasar radio emission because the angular diameter distances of the absorber (DA$_{\rm DLA}$) and the quasar (DA$_{\rm QSO}$) are essentially the same for DLAs at $z \gtrsim 1$. Conversely, low-z ($z < 1$) DLAs are typically more efficient at covering the radio emission because many low-z DLAs would have DA$_{\rm DLA}$ < DA$_{\rm QSO}$ (Curran [2012](#)).

As discussed in Section 7.2, our VLBA estimates of the covering factor have shown that the median upper limit to the transverse size of the radio core emission in DLAs at $z > 2$ is 350 pc. This is significantly lower than the size of even a dwarf galaxy, making it likely that all the core radio emission is covered in all cases: covering factor estimates should thus not be a serious issue for DLAs of the sample, especially since we have shown in Section 7.2 that the covering factor does not correlate with redshift. However, the increased sample size allows a simple test of whether the argument of Curran ([2012](#)), based on the similar angular diameter distances of foreground DLAs and background quasars, is indeed tenable. For this purpose, we restrict the base sample to the 25 DLAs at $z \geq 1$, the redshift above which the angular diameter distances to both the foreground DLAs and the background quasars are roughly equal. We divide these 25 absorbers into two sub-samples with redshifts above and below the median redshift of DLAs with $z \geq 1$ ($z_{\rm med} = 2.683$), and compare the spin temperature distributions of the two sub-samples. Since all 25 DLAs have DA$_{\rm DLA} \approx$ DA$_{\rm QSO}$, the issue of angular diameter distances cannot affect the results.

There are 12 DLAs each in the low-z ($1.0 < z < 2.683$) and high-z ($z > 2.683$) sub-samples (one absorber is at $z = 2.683$). The low-z sample has 9 detections and 3 non-detections of absorption, while the high-z sample has 11 non-detections and a single detection. We used a Peto–Prentice generalized Wilcoxon test to compare the spin temperature distributions (again appropriately taking into account the limits on $T_{\rm s}$) and find that the two $T_{\rm s}$ distributions differ at $\approx 3.5\sigma$ significance. There are both far more non-detections and higher spin temperatures in the high-z DLA sample.

Thus, the spin temperature distributions are clearly different even within the sub-sample of absorbers at $z \geq 1$, i.e. with DA$_{\rm DLA} \approx$ DA$_{\rm QSO}$. We conclude that angular diameter distances (and hence DLA covering factors) do not play a significant role in the low H I 21 cm optical depths measured in high-z DLAs, and that it is indeed the spin temperature that shows redshift evolution.

Figure 17. A comparison between the spin temperature distributions in the 37 DLAs of the full sample (filled circles) and sightlines in the Milky Way (open triangles), with both quantities plotted against the H I column density. Note that the Milky Way spin temperatures were estimated by comparing H I 21 cm emission and H I 21 cm absorption studies on neighbouring sightlines, while the DLA spin temperatures were estimated by comparing the H I 21 cm optical depth with the H I column density measured from the Ly-α absorption profile. The figure shows that the majority of DLA spin temperature lie at or above the upper edge of the envelope of Galactic $T_{\rm s}$ values (see also Carilli et al. [1996](#)). Two-sample tests yield strong evidence that the spin temperature distributions in DLAs and in the Galaxy are very different.

7.7 The CNM fraction in DLAs

As noted in Section 3, for sightlines containing a mixture of neutral gas in different temperature phases, the spin temperature derived from equation (3) is the column-density-weighted harmonic mean of the spin temperatures of different phases. One can hence use the measured spin temperatures in DLAs and assumptions about the spin temperatures in different gas phases to estimate the fraction of cold (≤ 200 K) gas along each sightline.

For the standard two-phase medium models of the ISM in the Milky Way, the kinetic temperatures of the CNM and WNM are ≈ 40–200 and ≈ 5000–8000 K, respectively (Field et al. 1969; Wolfire et al. 1995). While the actual temperature range depends on local conditions (e.g. the metallicity, pressure, the constituents of the ISM, etc.), detailed studies have shown that typical CNM kinetic temperatures are ≈ 100 K in both the Milky Way and external galaxies like M31 (e.g. Braun & Walterbos 1992; Heiles & Troland 2003a). Further, the high densities in the CNM imply that the H I 21 cm hyperfine transition is thermalized by collisions and the spin temperature in the CNM is hence approximately equal to the kinetic temperature (e.g. Field 1959; Liszt 2001).

On the other hand, there are few reliable estimates of the gas kinetic temperature in the WNM, even in the Milky Way, and there is even evidence that significant amounts of gas are in the unstable phase (e.g. Heiles & Troland 2003a; Kanekar et al. 2003). In DLAs, there have so far been two estimates of the WNM kinetic temperature, in the $z = 0.0912$ and 0.2212 DLAs towards 0738+313: Lane et al. (2000) obtained $T_k \approx 5500$ K in the former system, while Kanekar et al. (2001) measured $T_k \approx 7600$ K in the latter, both in agreement with the temperature ranges predicted by the two-phase models. Note that the spin temperature is expected to be lower than the kinetic temperature in the WNM, as the low gas density in WNM implies that collisions are insufficient to thermalize the H I 21 cm line here (e.g. Liszt 2001).

Kanekar & Chengalur (2003) and Srianand et al. (2012) assumed specific values for the CNM and WNM spin temperatures in order to infer the CNM fraction in their absorber samples. However, while it is reasonable to assume that the CNM spin temperature is equal to its kinetic temperature, this assumption is unlikely to be valid for the WNM. Given this, we will use a conservative approach to estimating the fraction of cold gas in the DLAs of our sample. We assume that each DLA contains some fraction of neutral gas (f_{CNM}) in the CNM phase and that the remaining gas is not in the CNM phase but at higher kinetic temperatures, with a fraction $f_{nCNM} = 1 - f_{CNM}$. Note that both fractions include gas at different kinetic (and spin) temperatures, in the range $T_s \approx T_k = 40-200$ K for the CNM and at higher temperatures for the remaining gas in the non-CNM phase. We also assume that the column-density-weighted harmonic mean spin temperature in the CNM is $T_{s,CNM} \approx 100$ K (the results do not change significantly if one assumes a higher CNM spin temperature, ≈ 200 K). This allows us to rewrite equation (4) for the measured DLA spin temperature as

$$\frac{1}{T_s} = \frac{f_{CNM}}{100} + \frac{1 - f_{CNM}}{T_{s,nCNM}} \ , \tag{5}$$

where T_s is the DLA spin temperature and $T_{s,nCNM}$ is the column-density-weighted harmonic mean spin temperature for the gas that is *not* CNM. One then obtains

$$f_{CNM} = \left[\frac{1}{(T_{s,nCNM}/100) - 1} \right] \left[\frac{T_{s,nCNM}}{T_s} - 1 \right] \ . \tag{6}$$

Fig. 18 shows the CNM fraction f_{CNM} plotted against $T_{s,nCNM}$ for different values of the DLA spin temperature, T_s. It is clear that, for
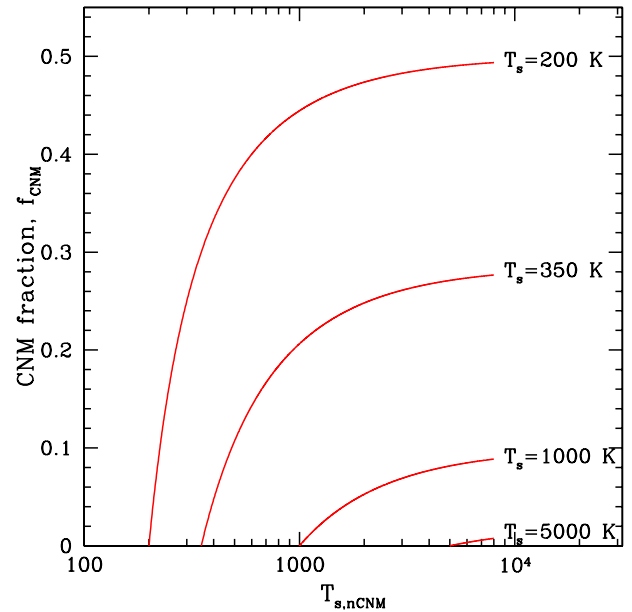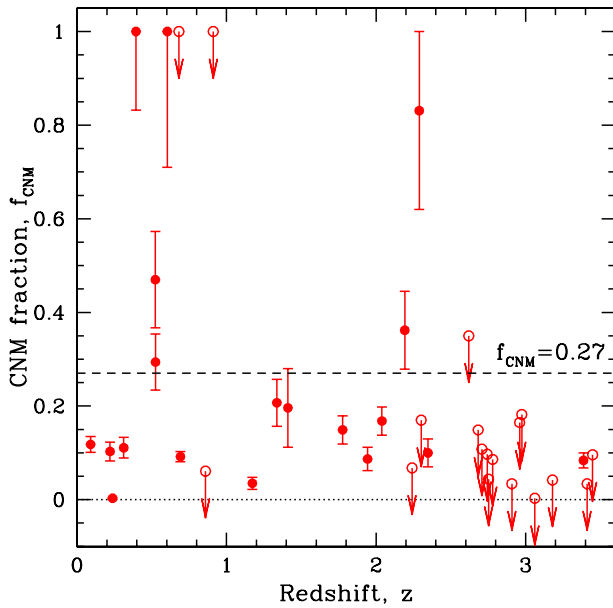

Figure 18. The CNM fraction plotted against the column-density-weighted harmonic mean spin temperature of gas that is *not* in the CNM phase $T_{s,nCNM}$, for different DLA spin temperatures T_s and an assumed CNM spin temperature of 100 K. Note that the DLA spin temperature T_s is the value inferred from equation (3), when the possible multiphase nature of the gas is not taken into account. The *highest* CNM fraction is obtained when $T_{s,nCNM} = 8000$ K (not shown in the figure).

a given DLA spin temperature, the *highest* value of f_{CNM} will be obtained when $T_{s,nCNM}$ is large. We can thus obtain an upper limit on the CNM fraction for each DLA by assuming $T_{s,nCNM} = 8000$ K in equation (6), along with the DLA spin temperature. Note that this is equivalent to assuming that all the remaining (non-CNM) gas is in the WNM, with $T_s = 8000$ K. This is a stringent assumption for two reasons: (1) 8000 K is the upper limit of the range of stable WNM kinetic temperatures (Wolfire et al. 1995), and (2) the spin temperature is expected to be lower than the kinetic temperature in the WNM (Liszt 2001).

Fig. 19 shows the CNM fraction estimated from the above approach plotted versus DLA redshift for the 37 DLAs of the full sample. The downward-pointing arrows in the figure indicate non-detections of H I 21 cm absorption, and thus lower limits on the DLA spin temperature and upper limits on the CNM fraction. The figure shows that the CNM fractions in DLAs are typically quite low, $\lesssim 20$ per cent, at all redshifts, with only a few absorbers having comparable CNM and WNM fractions. At high redshifts, $z > 1.7$, only 2 of the 23 absorbers have CNM fractions greater than 27 per cent, with one of the upper limits also in this range. This is significantly lower than the CNM fraction along Galactic sightlines, where the median CNM fraction is ≈ 27 per cent (Heiles & Troland 2003b). We emphasize further that every point in Fig. 19 is an *upper* limit to the CNM fraction in a DLA, due to the assumption that gas in the non-CNM phase has $T_{s,nCNM} = 8000$ K. We conclude that the CNM fractions in high-z DLAs are significantly lower than those typical of the Galaxy. Similar conclusions have been drawn based on smaller H I 21 cm absorption samples by Kanekar & Chengalur (2003), Srianand et al. (2012) and Ellison et al. (2012), and from H$_2$ absorption studies by Petitjean, Srianand & Ledoux (2000).

We note that three of the four low-z absorbers with $f_{CNM} \gtrsim 0.27$ have been identified with spiral galaxies; these are the DLAs at $z = 0.3950$ towards $1229-021$ ($f = 1$), $z = 0.5242$ towards

Figure 19. The CNM fraction plotted against redshift for the 37 DLAs of the sample (i.e. excluding the two sub-DLAs); the dashed horizontal line shows the median CNM fraction in the Galaxy ($f_{CNM} = 0.27$). The column-density-weighted harmonic mean spin temperatures are assumed to be 100 K in the CNM and 8000 K in the non-CNM phases; this ensures that the derived CNM fraction is an upper limit to the 'true' CNM fraction. The majority of DLAs, especially at high redshifts, have low CNM fractions, ≤ 20 per cent.

0235+164 ($f = 0.47$) and $z = 0.5247$ towards 0827+243 ($f = 0.294$; Burbidge et al. 1996; le Brun et al. 1997; Chen, Kennicutt & Rauch 2005). We suggest that the fourth system, at $z = 0.6019$ towards 1429+400 ($f = 1$; Ellison et al. 2012), as well as the two high-CNM absorbers at $z \sim 2.192$ towards 2039+187 ($f = 0.36$; Kanekar et al. 2013) and $z \sim 2.2890$ towards 0311+430 ($f = 0.83$; York et al. 2007) are also likely to be bright disc galaxies. Imaging studies of these DLAs would be of much interest.

7.8 DLA spin temperatures, metallicities and dust depletions

The results of the preceding sections have shown that the majority of DLAs at all redshifts have higher spin temperatures and lower CNM fractions than typically seen in the Milky Way and M31 (e.g. Colgan et al. 1988; Braun & Walterbos 1992; Kanekar et al. 2011), due to lower fractions of the cold phase of neutral hydrogen. In the ISM, collisional excitation of the fine-structure lines of metals like C II and O I dominates the cooling below temperatures of ≈ 8000 K (Launay & Roueff 1977; Wolfire et al. 1995). Galaxies with low metallicities would then be expected to have fewer cooling routes than high-metallicity systems like the Milky Way, and hence larger amounts of warm gas. For example, fig. 6 of Wolfire et al. (1995) shows that, at lower metallicities, a higher central pressure is needed to produce the cold phase of H I. Kanekar & Chengalur (2001b) used this to argue that the high spin temperatures in most high-z DLAs could be naturally explained if the absorbers are typically low-metallicity systems with low CNM fractions due to a lack of cooling routes. Conversely, DLAs with high metallicities would be expected to have higher CNM fractions and low spin temperatures. Kanekar & Chengalur (2001b) hence predicted an anticorrelation between the spin temperature and metallicity, if metallicity is indeed the dominant cause in determining the cold gas content of a galaxy.

A test of this hypothesis was first carried out by Kanekar et al. (2009c) (see also Kanekar & Chengalur 2005), who used T_s and [Z/H] data on 26 DLAs (including limits) to detect the predicted anticorrelation at 3.6σ significance, via a non-parametric generalized Kendall test (Brown et al. 1974; Isobe et al. 1986). The anticorrelation was detected at lower significance ($\approx 3\sigma$) in a sub-sample of 20 systems with estimates of the covering factor. Ellison et al. (2012) extended this study to 26 DLAs and sub-DLAs with covering factor estimates, using some of the new data presented in this paper; this improved the detection significance of the anticorrelation to $\approx 3.4\sigma$. Recently, Srianand et al. (2012) examined the possibility of redshift evolution in the relation between T_s and [Z/H], but found no evidence in support of this, perhaps due to the small size of their sample.

Three of the DLAs in this paper have new VLBA estimates of the covering factor, while the detection of H I 21 cm absorption at $z = 2.192$ towards 2039+187 has recently been presented by Kanekar et al. (2013). These systems were not included in the analysis of Ellison et al. (2012). We have also in this paper obtained more accurate estimates of the metallicities of the $z = 0.3127$ and 0.5247 DLAs towards 1127−145 and 0827+243, respectively. The sample of DLAs with estimates (including limits) of T_s and [Z/H], as well as measurements of the low-frequency covering factor now contains 29 systems. Fig. 20 shows the spin temperature T_s plotted against metallicity [Z/H] for this sub-sample. We have used the generalized Kendall-tau rank correlation test (the BHK statistic; Brown et al. 1974) to detect the anticorrelation between T_s and [Z/H] at $\approx 3.5\sigma$ significance, somewhat higher than the result of Ellison et al. (2012). We emphasize that this is a non-parametric test that also takes into account the presence of limits in the sample. Further, unlike Ellison et al. (2012), we have excluded sub-DLAs from the present analysis.

We also tested whether either the high-z or the low-z DLA sub-sample dominates the detected anticorrelation between the metallicity and spin temperature. The median redshift of the 29 DLAs with
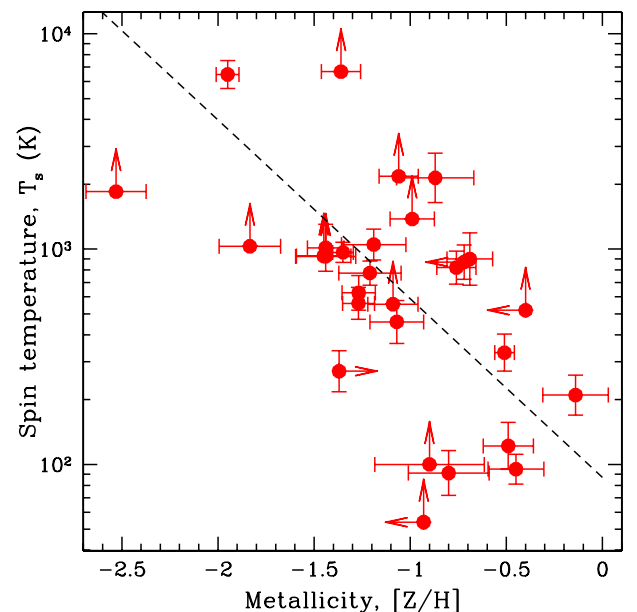
Figure 20. The spin temperature T_s plotted against metallicity [Z/H] for the 29 DLAs of the full sample that have measurements of both quantities. The dashed line shows the linear regression fit, $\log[T_s] = (-0.83 \pm 0.16) \times [Z/H] + (1.94 \pm 0.20)$, to the 16 measurements of both T_s and [Z/H].

estimates of both metallicity and spin temperature is $z = 1.7763$, with 14 DLAs each in the low-z and high-z sub-samples. The anticorrelation between T_s and [Z/H] is detected at 2.3σ and 2.2σ significance in the low-z and high-z sub-samples, respectively. A similar statistical significance (2.2σ) is obtained for the anticorrelation even on restricting the sample to the 12 DLAs at $z < 1$. This indicates that the anticorrelation is not dominated by either the low-z or the high-z DLAs. Specifically, the high-z DLAs, where the covering factor is more uncertain, do not dominate the anticorrelation.

The dashed line in Fig. 20 shows an update of the linear fit of Ellison et al. (2012) to the T_s–[Z/H] relation. This uses a regression analysis based on the BCES(Y/X) estimator (Akritas & Bershady 1996), with [Z/H] as the independent variable, X, applied to the 16 DLAs with measurements of *both* T_s and [Z/H] (Kanekar et al. 2009c; Ellison et al. 2012). We obtain $\log[T_s] = (-0.83 \pm 0.16) \times$ [Z/H] + (1.94 ± 0.20), essentially the same as the fit of Ellison et al. (2012). Note that the sample used for the latter regression analysis included the $z = 1.6724$ sub-DLA towards 0237−233.

We have also examined the sample for a relation between T_s and dust depletion [Z/Fe]. 26 DLAs with covering factor measurements also have estimates of both quantities (cf. 23 DLAs and sub-DLAs in Ellison et al. 2012). Fig. 21 plots the spin temperature against dust depletion for this sub-sample. We find only weak evidence for an anticorrelation between T_s and [Z/Fe]; this is detected at $\approx 2.4\sigma$ significance. As argued by Kanekar et al. (2009c) and Ellison et al. (2012), it does not appear that the anticorrelation between T_s and metallicity is due to an underlying relation between T_s and dust depletion.

We find no evidence that the probability of detecting H I 21 cm absorption depends on the absorber metallicity. For the 25 DLAs with measurements of metallicity (i.e. excluding absorbers with only limits on the metallicity), the median metallicity is $[Z/H]_{med} = -1.09$. The H I 21 cm detection rates are 75^{+25}_{-25} and 54^{+29}_{-20} per cent for systems above and below the median metallicity, consistent within 1σ confidence intervals.
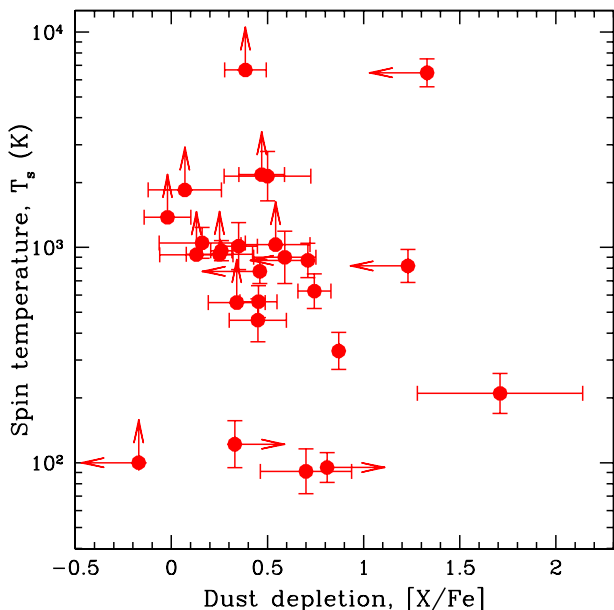
Figure 21. The spin temperature T_s plotted against dust depletion [Z/Fe] for the 26 DLAs with low-frequency covering factor estimates that have measurements of both quantities. Only weak evidence is found for an anticorrelation between T_s and [Z/Fe].

In passing, we note that the above analysis has used the X-ray metallicity estimate for the $z = 0.524$ DLA towards QSO 0235+164. As discussed in Ellison et al. (2012), excluding this DLA from the sample does not significantly affect the significance of the anticorrelation between the metallicity and spin temperature.

Note that the DLA spin temperatures have been estimated under the assumptions that (1) the H I column density measured along the optical sightline is the same as that towards the radio core, and (2) the quasar core fraction can be interpreted as the DLA covering factor. Conversely, the DLA metallicities have been estimated from the optical spectra alone, without any such assumptions. Any breakdown in the assumptions (e.g. due to differences in the H I column densities along the optical and radio sightlines) should weaken any underlying relation between T_s and [Z/H]. The fact that the predicted anticorrelation between T_s and [Z/H] is yet detected in a non-parametric test indicates that such differences between the optical and radio sightlines are very unlikely to give rise to the high spin temperatures seen in the majority of high-z DLAs. We conclude that the assumptions regarding the H I column density and the DLA covering factor are likely to be reliable, at least in a statistical sense (unless the observed anticorrelation is mere coincidence).

7.9 On the assumption that the covering factor is equal to the core fraction

The results in Sections 7.5–7.8 are based on the assumption that the DLA covering factor is equal to the radio core fraction. While the measured radio core sizes are quite small, <1 kpc, far smaller than the size of a typical absorbing galaxy, it is possible that this assumption is violated for at least some DLAs of the sample. Further, it is also possible that any detected H I 21 cm absorption might arise against extended radio structure and not against the radio core; in such a situation, the covering factor would be uncorrelated with the core fraction. Unfortunately, it is very difficult to directly measure the covering factor of individual DLAs. In this section, we hence use Monte Carlo simulations to test whether our results critically depend on the assumption that the covering factor is equal to the core fraction.

We first considered the possibility that the covering factor is indeed statistically equal to the core fraction, but that there is a random error associated with each covering factor estimate. We assume that this error is normally distributed with a standard deviation equal to 10, 20, 50 and 100 per cent of the measured core fraction. For each assumed standard deviation, we randomly selected values of f (constrained to be in the range $0 < f \leq 1$), re-compute the spin temperature and use the Kendall-tau test to estimate the significance of the anticorrelation between the metallicity and spin temperature, and the Peto–Prentice test to determine the significance of the redshift evolution of the spin temperature, as done in Sections 7.8 and 7.5, respectively. The process was repeated over 10 000 Monte Carlo runs for each assumed standard deviation, and we then computed the mean statistical significance of the anticorrelation between T_s and [Z/H] and of the redshift evolution in T_s over each set of 10 000 runs. We found that the significance of both results remains high, even if the error on the covering factor has a 50 per cent standard deviation. Specifically, for a standard deviation of 50 per cent, the anticorrelation between T_s and [Z/H] is detected at $\approx 3.2\sigma$ significance, while the difference in the T_s distributions in high-z and low-z samples (separated at the median redshift, $z_{med} = 2.192$) has $\approx 3.3\sigma$ significance. Indeed, even allowing for a 100 per cent error in the covering factor only reduces the significance of the anticorrelation between T_s and [Z/H] to 2.7σ, not a very strong effect, while

the difference in T_s distributions has $\approx 3.2\sigma$ significance. We conclude that even a large random error in the inferred covering factor does not significantly affect our results.

We also considered the worst-case scenario in which the covering factor is entirely uncorrelated with the measured radio core fraction. Since the covering factor must take values between 0 and 1, we randomly selected values for f in this range (assuming a uniform distribution between 0 and 1), independently for each DLA of the sample, and then re-computed the spin temperature for each DLA. We then repeated the Monte Carlo simulations for the anticorrelation between the spin temperature and metallicity and the redshift evolution of the spin temperature (following the approach described in the previous paragraph), with the mean statistical significance of the two relations again computed from 10 000 Monte Carlo runs. The anticorrelation between T_s and [Z/H] is then detected at $\approx 2.9\sigma$ significance, while the difference between the spin temperature distributions in the high-z and low-z DLA samples (again separated at the median redshift, $z_{med} = 2.192$) has $\approx 3.1\sigma$ significance, averaging over 10 000 Monte Carlo runs. Again, while the significances of both results are somewhat lower than the values obtained on using the assumption that the covering factor is equal to the core fraction ($\approx 3.5\sigma$ for the T_s–[Z/H] relation and $\approx 3.5\sigma$ for the redshift evolution in T_s; see Sections 7.5 and 7.8), it is clear that there is no significant change in the results even on assuming an entirely random distribution of DLA covering factors.

We also used the above Monte Carlo simulations to examine the effect of systematic biases in the covering factor. We find that if all DLAs have low (or high) covering factors, our two main results (the anticorrelation between T_s and [Z/H] and the redshift evolution of T_s) remain unchanged. The only way to reduce the statistical significance of the T_s–[Z/H] anticorrelation is to assign very low covering factors ($f < 0.1$) to DLAs with high inferred spin temperatures, so as to effectively reduce the derived T_s. This is essentially similar to the argument of Curran & Webb (2006), that low DLA covering factors due to geometric effects can account for the inferred high DLA spin temperatures. However, as discussed in Section 7.6, there is statistically significant evidence for redshift evolution in the spin temperature even when we only consider the sub-sample of DLAs at $z > 1$, for which geometric effects cannot yield different DLA covering factors. As such, the result that the spin temperature of DLAs shows evidence of redshift evolution remains unaffected by the possibility that high-z DLAs are less effective at covering the background quasars.

Further, if low covering factors of high-z DLAs are the cause of the anticorrelation between the metallicity and spin temperature, we would expect that the anticorrelation would be detected at higher significance in the high-z DLA sample. As discussed in Section 7.8, this is not the case, with the low-z and high-z sub-samples making roughly equal contributions to the significance of the anticorrelation.

We conclude that our results do not significantly depend on the assumption that the DLA covering factors are equal to the quasar radio core fractions. We also find no evidence that our results might be affected by systematic biases in the covering factor.

7.10 DLA spin temperatures and velocity widths

DLA metallicities have been shown to be correlated with the velocity spreads of low-ionization metal lines (Wolfe & Prochaska 1998; Ledoux et al. 2006; Prochaska et al. 2008a), as well as with the rest equivalent widths of the Mg II λ2796 and Si II λ1526 lines (Murphy et al. 2007; Prochaska et al. 2008a). We hence examined the possibility that the anticorrelation between the spin temperature
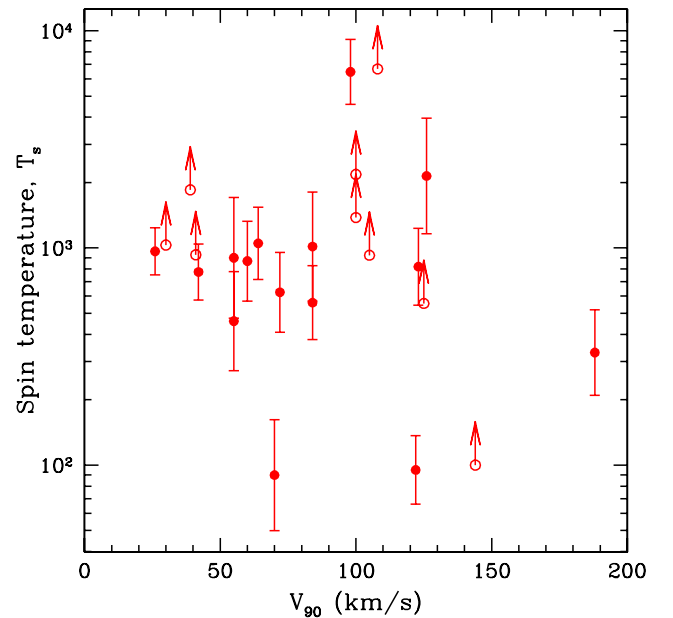
Figure 22. The spin temperature T_s plotted against the velocity width at the 90 per cent optical depth in the low-ionization metal lines, ΔV_{90}, for the 25 DLAs (filled circles) and sub-DLAs (open star) with estimates of both quantities. The figure shows no evidence for a relation between T_s and ΔV_{90}.

and metallicity might arise because the spin temperature depends on the velocity spread of the absorber.

Our sample contains ΔV_{90} measurements for 24 DLAs, with a median ΔV_{90} value of $84\,km\,s^{-1}$. The detection rates of H I 21 cm absorption are 45^{+31}_{-20} and 73^{+27}_{-25} per cent for systems with ΔV_{90} values above and below the median, respectively. We thus find no evidence that the detection rate of H I 21 cm absorption depends on the velocity spread of the low-ionization metal lines.

Fig. 22 plots the spin temperature against the 90 per cent optical depth velocity spread ΔV_{90} for the 24 DLAs with estimates of both quantities. The figure resembles a scatter plot, with no obvious relation between the two quantities. Similarly, the generalized Kendall-tau test (taking limits into account) finds no evidence of a correlation between T_s and ΔV_{90} (0.2σ statistical significance). We conclude that it is very unlikely that the observed correlation between T_s and metallicity arises due to an underlying relation between the spin temperature and the velocity spread of the low-ionization metal lines.

The correlation between the metallicity and velocity spread in DLAs has usually been interpreted in terms of a mass–metallicity relation (Ledoux et al. 2006), similar to those observed in the local Universe or in bright high-z galaxies (e.g. Tremonti et al. 2004; Erb et al. 2006; Prochaska et al. 2008a; Neeleman et al. 2013). Since high-mass galaxies have higher central pressures, they are expected to have higher CNM fractions (Wolfire et al. 1995). It might then appear curious that no relation is seen between T_s and ΔV_{90}. While the sample size of systems with ΔV_{90} estimates is relatively small (24 systems), the anticorrelation between the spin temperature and metallicity is detected at 3.6σ significance with a similar number of systems (29). We surmise that this is because the metallicity directly determines the number of cooling routes and hence the cold gas fraction. Conversely, it is clear that there are other contributors besides mass to the observed ΔV_{90} in absorption. For example, high-mass galaxies observed at low inclinations to the line of sight

can have low velocity spreads in absorption; DLA surveys may have some bias towards such systems, due to their larger surface area on the sky. There are also contributions to the velocity spread from merging galaxies, outflows from galactic winds, galactic infall, etc., which can increase ΔV_{90} for low-mass galaxies above the values expected due to rotation. For galaxies in the local Universe, where the mass can be estimated directly, Zwaan et al. (2008) find only a weak relation between ΔV_{90} and mass. Finally, the relation between [Z/H] and ΔV_{90} itself has a large spread, ≈ 1.5 dex in metallicity at a given ΔV_{90} (see fig. 6[A] of Prochaska et al. 2008a). It is hence perhaps not very surprising that the observed spin temperature does not depend strongly on the velocity spread of the absorbing galaxy.

7.11 Comparisons with results from C II* absorption studies

Over the last decade, it has been suggested that the strength of C II* $\lambda 1335.7$ absorption provides a means of distinguishing between DLAs containing significant CNM fractions and ones whose neutral phase is dominated by the WNM (Wolfe, Prochaska & Gawiser 2003a; Wolfe et al. 2003b, 2004). This is because the most important coolant of the neutral ISM is the [C II] 158 µm line (e.g. Pottasch, Wesselius & van Duinen 1979; Wright et al. 1991; Wolfire et al. 1995). Since this arises from transitions between the $^2P_{3/2}$ and $^2P_{1/2}$ levels in the ground state of ionized carbon, it should be possible to determine the cooling rate per H atom by measuring the abundance in the [C II] $^2P_{3/2}$ state from the strength of the UV C II* $\lambda 1335.7$ line (Pottasch et al. 1979). Assuming thermal balance then allows one to infer the heating rate from the cooling rate: for the CNM, where the cooling is dominated by the [C II] 158 µm line, the heating rate is approximately equal to the cooling rate, while, for the WNM, the heating rate is significantly larger than the derived cooling rate. Since the heating rate is dominated by photoelectric emission of electrons from grains by incident far-UV radiation (Bakes & Tielens 1994), Wolfe et al. (2003a) argued that one could use this heating rate in conjunction with measurements of the dust-to-gas ratio in DLAs and an assumed grain photoelectric heating efficiency to infer the SFR per unit area in high-z DLAs. This could further be used to probe the distribution of neutral gas between the CNM and WNM phases, by assuming two-phase models in pressure equilibrium (Field et al. 1969; Wolfire et al. 1995, 2003).

Wolfe et al. (2003a) considered two models for the neutral ISM, a 'pure-WNM' model with all the H I in the WNM and a 'CNM+WNM' model in which comparable amounts of H I are in each phase. They find that 'pure-WNM' models are ruled out for DLAs with strong C II* $\lambda 1335.7$ absorption, as the bolometric luminosities of such DLAs would be far higher than observed values (see also Wolfe et al. 2003b, 2004). The 'pure-WNM' model was found to be applicable to absorbers with low C II* $\lambda 1335.7$ column densities (i.e. either non-detections of C II* $\lambda 1335.7$ absorption or weak C II* $\lambda 1335.7$ absorbers). About half the DLAs in the sample of Wolfe et al. (2008a) lie in this category. Wolfe et al. argue that the observed strong C II* $\lambda 1335.7$ absorption in the remaining DLAs must arise in the CNM and that the 'CNM+WNM' model is applicable here. Finally, Wolfe et al. (2008a) argue that the C II 158 µm cooling rate per hydrogen atom l_c may be a separator of DLAs into two categories, 'high-cool' systems with high cooling rates $l_c > 10^{-27}$ erg s^{-1} H^{-1} (with high metallicities, large velocity spreads and significant CNM fractions) and 'low-cool' systems with low cooling rates $l_c < 10^{-27}$ erg s^{-1} H^{-1} (with low metallicities, low velocity spreads and with the H I mostly in the WNM phase).

With regard to H I 21 cm studies, Wolfe et al. (2003b) noted that there are two high-z DLAs with non-detections of H I 21 cm ab-

sorption and high inferred lower limits on the spin temperatures, but which show strong C II* $\lambda 1335.7$ absorption: these are the systems at $z = 3.0621$ towards 0336−017 and $z = 3.387$ towards 0201+113. Wolfe et al. (2003b) suggested that both systems are likely to have high CNM fractions (≈ 50 per cent) along the sightline to the optical QSO; they argued that the high spin temperature limits obtained from the H I 21 cm absorption studies might arise because the relatively small (10−20 pc) CNM clouds do not entirely cover even the radio quasar core, which is significantly more extended than the optical quasar in both cases. Later, Kanekar et al. (2007) detected H I 21 cm absorption towards 0201+113 (see also Briggs et al. 1997) and also found that the radio quasar core here has a transverse size of ≤286 pc. This implies that it is possible that the CNM clouds do not fully cover the radio core, as suggested by Wolfe et al. (2003b). However, Kanekar et al. (2007) also showed that the CNM fraction towards the radio quasar core is ≲17 per cent, even if one assumes that the sightline towards the optical core has a far higher CNM fraction, ≈ 50 per cent. Thus, even if the arguments of Wolfe et al. (2003b) are correct and the 10−20 pc-sized CNM clouds do not efficiently cover the radio core, the sightline towards the radio core is still dominated by the WNM, with >80 per cent of the H I in this phase.

For clarity, the upper part of Table 6 summarizes the C II* $\lambda 1335.7$ and H I 21 cm results for the sub-set of DLAs with studies in both transitions and VLBI estimates of the covering factor. The columns in this table show (1) the quasar name, (2) the quasar redshift z_{QSO}, (3) the DLA redshift, (4) the H I column density, (5) the C II 158 µm cooling rate per atom, $\log[l_c]$, inferred from the C II* $\lambda 1335.7$ line strength (Wolfe et al. 2008a), (6) the metallicity, [Z/H], (7) the spin temperature T_s, (8) the CNM fraction, assuming $T_{s,CNM} = 100$ K and $T_{s,WNM} = 8000$ K, and (9) the H$_2$ fraction (Ledoux et al. 2003; Noterdaeme et al. 2008). Based on the classification of Wolfe et al. (2008a), the absorbers towards 1354−170 and 1331+170 are 'low-cool' systems ($\log[l_c/\text{erg s}^{-1}\,\text{H}^{-1}] \lesssim -27$), while those towards 0201+113, 0336−017, 0458−020, 1157+014 and 2342+342 are 'high-cool' systems ($\log[l_c/\text{erg s}^{-1}\,\text{H}^{-1}] > -27$. Note that the systems towards 1354−170 and 2342+342 are consistent with both categories, within 1σ errors, but are definitely not strong C II* $\lambda 1335.7$ absorbers.

At the outset, it is relevant to note that the C II* $\lambda 1335.7$ and H I 21 cm absorption results appear in reasonable agreement for about half the DLA sample, the systems with weak or undetected C II* $\lambda 1335.7$ absorption (i.e. the 'low-cool' systems). Wolfe et al. (2008a) find that these systems have systematically lower metallicities (and dust-to-gas ratios and velocity widths) than the 'high-cool' systems that have strong C II* $\lambda 1335.7$ absorption, and conclude that the neutral gas here is predominantly WNM. The anticorrelation between the metallicity and spin temperature would lead us to conclude that such DLAs have high spin temperatures and are thus dominated by the WNM; there is thus no disagreement between the C II* $\lambda 1335.7$ and H I 21 cm results for systems with weak C II* $\lambda 1335.7$ absorption and high spin temperatures. These include the DLAs at $z = 2.7799$ towards 1354−170 and $z = 2.9084$ towards 2342+342, for which both the relatively weak C II* $\lambda 1335.7$ absorption and the high spin temperatures are consistent with most of the H I being in the WNM.

The primary difference between the results on the CNM fractions obtained from the C II* $\lambda 1335.7$ and H I 21 cm absorption studies is for the 'high-cool' sample of Wolfe et al. (2008a). However, the apparent discrepancy appears mainly due to the fact that Wolfe et al. (2003b) (and later works) only consider two models, 'CNM+WNM', with half the H I in the CNM phase and the other

Table 6. DLAs with H I 21 cm and C II* λ1335.7 or H_2 absorption studies.

QSO	z_{QSO}	z_{abs}	$\log[N_{HI}/cm^{-2}]$	$\log[l_c]/erg\,s^{-1}\,H^{-1}$	[Z/H]	T_s (K)	$\log[f_{H2}]$
DLAs with H I 21 cm and C II λ1335.7 absorption studies*							
0201+113	3.639	3.3869	21.25 ± 0.07	-26.66 ± 0.14	-1.19 ± 0.17	1050 ± 175	-4.6 to -6.2
0336−017	3.197	3.0621	21.20 ± 0.10	-26.71 ± 0.10	-1.36 ± 0.10	>8890	<-6.90
0458−020	2.286	2.0395	21.78 ± 0.07	>-26.37	-1.269 ± 0.072	560 ± 95	<-6.40
1157+014	2.000	1.9436	21.80 ± 0.07	>-26.51	-1.440 ± 0.086	1015 ± 255	<-6.65
1331+170	2.084	1.7764	21.18 ± 0.07	<-27.12	-1.268 ± 0.076	625 ± 115	-1.25 ± 0.05
1354−170	3.147	2.7799	21.30 ± 0.15	-27.06 ± 0.16	-1.83 ± 0.16	>1030	–
2342+342	3.053	2.9084	21.10 ± 0.10	-26.92 ± 0.12	-1.06 ± 0.10	>2200	<-6.19
DLAs with H I 21 cm and H_2, but no C II λ1335.7, absorption studies*							
0335−122	3.442	3.1799	20.78 ± 0.11	–	-2.53 ± 0.16	>1850	<-5.10
0432−440	2.649	2.3023	20.78 ± 0.11	–	-1.09 ± 0.13	>555	<-5.15
1418−064	3.689	3.4482	20.40 ± 0.10	–	-1.45 ± 0.14	>930	<-5.69

References: the H_2 fractions are from Cui et al. (2005), Noterdaeme et al. (2008) and Srianand et al. (2012), while the $\log[l_c]$ values are from Wolfe et al. (2008a). References for the metallicities, H I column densities and spin temperatures are given in Table 4. Note that PDLAs (e.g. the $z = 2.8111$ system towards 0528−250) have not been included in the table.

half in the WNM, and 'pure-WNM', with all the H I in the WNM, and rule out the latter model, based on the fact that the C II* λ1335.7 absorption must arise from the CNM. But even if one accepts that all the C II* λ1335.7 absorption arises from the CNM (although see Srianand et al. 2005), this does not imply that half the H I must be CNM. There is no obvious problem with a model in which 10–20 per cent of the H I in DLAs with strong C II* λ1335.7 absorption is CNM (as suggested by Fig. 19), and with all the C II* λ1335.7 absorption produced by the CNM. There are three DLAs at $z > 1.7$ that show both H I 21 cm and strong C II* λ1335.7 absorption; these are the absorbers at $z \sim 1.9436$ towards 1157+014, $z \sim 2.0395$ towards 0458−020 and $z \sim 3.3869$ towards 0201+113. The three absorbers have inferred CNM fractions of ≈9–17 per cent and intermediate metallicities, $[Z/H] \approx -1.3$ (see Section 7.7 and Tables 4 and 6); these are not inconsistent with the observed strong C II* λ1335.7 absorption. In fact, given that these DLAs all have high column densities, $N_{HI} \geq 1.8 \times 10^{21}\,cm^{-2}$, it is possible that the H I column density towards the radio core is lower than that towards the optical quasar by a factor of ≈1.5 in these systems (see Section 7.3). The spin temperature estimates in these DLAs could hence be lower, and the inferred CNM fractions higher, by ≈50 per cent. We emphasize that Wolfe et al. (2003b, 2004) only rule out the 'pure-WNM' model for such strong C II* λ1335.7 absorbers, but do not rule out models with CNM fractions of ≈10–20 per cent and WNM fractions of ≈80–90 per cent.

The sole absorber in Table 6 for which there remains a clear discrepancy between the C II* λ1335.7 and T_s data is the $z = 3.0621$ DLA towards 0336−017. Wolfe et al. (2008a) classify this as a 'high-cool' DLA, since $\log[l_c/erg\,s^{-1}\,H^{-1}] = -26.71 \pm 0.10$, while we obtain $T_s > 8890 \times (f/0.68)$. One way of accounting for this difference is a fortuitously high fraction of CNM clouds towards the optical quasar, which do not efficiently cover the more extended radio core (Wolfe et al. 2003b). Following the argument of Kanekar et al. (2007) (in the context of the $z = 3.387$ DLA towards 0201+113), this would still imply a high WNM fraction towards the radio core of 0336−017, since the core is small enough ($\lesssim 224\,pc$; Kanekar et al. 2009a) to be entirely covered by the extended WNM clouds. Another possibility is that the average H I column density towards the quasar radio core is lower in the $z = 3.0621$ DLA towards 0336−017 than that towards the optical QSO. While the upper limit to the transverse core size is only ≈224 pc in the $z = 3.0621$ DLA

(i.e. lower than the median for DLAs at $z > 2$), it is possible that there is small-scale structure in the H I distribution, so that the average H I column towards the optical core is a few times larger than that towards the radio core. This is certainly possible along individual sightlines. It is also possible that some of the C II* λ1335.7 absorption along this sightline arises in either the WNM or ionized gas (Srianand et al. 2005).

Finally, the $z = 1.7764$ DLA towards 1331+170 is a 'low-cool' DLA, with $\log[l_c/erg\,s^{-1}\,H^{-1}] < -27.12$ (Wolfe et al. 2008a; Jorgenson et al. 2010). This has $T_s = (625 \pm 115) \times (f/0.72)$ K and a CNM fraction of $\lesssim 15$ per cent, derived from a new H I 21 cm absorption spectrum (Carswell et al. 2011) and the VLBA covering factor of $f = 0.72$ (Kanekar et al. 2009a). There is no significant contradiction between the T_s and C II* λ1335.7 results in this absorber, since both suggest high WNM fractions. However, it is difficult to reconcile the weak C II* λ1335.7 absorption with the fact that H_2 and C I absorption have both been detected in this DLA (Meyer et al. 1986; Cui et al. 2005; Jorgenson et al. 2010), clearly indicating the presence of CNM in the absorber (as is also shown by the detected H I 21 cm absorption). Indeed, the H_2 fraction in the $z = 1.7764$ DLA is one of the highest in the entire DLA sample (Cui et al. 2005; Noterdaeme et al. 2008). Despite this, C II* λ1335.7 absorption is not detected (or is, at best, quite weak) in this absorber (Jorgenson et al. 2010). Similarly, the C II* λ1335.7 absorption is weak in the $z = 2.431$ DLA towards 2343+125 ($\log[l_c/erg\,s^{-1}\,H^{-1}] = -27.09 \pm 0.10$), despite the presence of H_2 absorption in this system and a high metallicity, $[Z/H] = -0.54 \pm 0.01$ (Petitjean et al. 2006). It thus appears that, contrary to the discussion in Wolfe et al. (2004), the absence of C II* λ1335.7 absorption does not imply the absence of CNM in individual DLAs, while, conversely, the presence of strong C II* λ1335.7 absorption merely indicates the presence of CNM, and not necessarily a high CNM fraction.

In summary, we find that there is no significant discrepancy between the C II* λ1335.7 results of Wolfe et al. (2003a, 2004) and our results from H I 21 cm absorption studies. The anticorrelation between the metallicity and spin temperature is consistent with the finding of Wolfe et al. (2008a) that DLAs with high metallicities tend to be 'high-cool' systems, while those with low metallicities have low cooling rates. The apparent discrepancy between the results is because Wolfe et al. (2003a) (and later papers) only considered two

models, one with half the gas each in the CNM and WNM and the other with all the gas in the WNM. Both the C II* λ1335.7 and H I 21 cm absorption results appear to be consistent with a model in which (1) high-metallicity ([Z/H] $\gtrsim$ −0.5) DLAs have high CNM fractions, $\approx$50 per cent, (2) intermediate-metallicity DLAs (with [Z/H] $\approx$ −1) have 10–20 per cent of the neutral gas in the CNM, with this phase producing the C II* λ1335.7 and H I 21 cm absorption, and (3) low-metallicity DLAs ([Z/H] $\lesssim$ −1.5) have most of their gas in the WNM, with low cooling rates and high spin temperatures.

7.12 Comparing CNM and molecular fractions

It is also interesting to compare the inferred CNM fractions $f_{\rm CNM}$ in DLAs (from Section 7.7) to the molecular hydrogen fraction $f_{\rm H_2} \equiv 2N(\rm H_2)/(2N(\rm H_2) + N_{H_I})$, for absorbers with estimates of both quantities. Since both trace the presence of cold gas, a relation between $f_{\rm CNM}$ and $f_{\rm H_2}$ might provide information on the process of molecule formation in DLAs. Searches for molecular hydrogen have now been carried out in nearly a hundred DLAs, mostly with high-resolution optical spectroscopy (e.g. Levshakov & Varshalovich 1985; Petitjean et al. 2000, 2006; Ledoux et al. 2003; Cui et al. 2005; Noterdaeme et al. 2008). However, detections of H$_2$ absorption have been obtained in only $\approx$16 per cent of DLAs at $z > 2$, with most absorbers showing low molecular fractions, $f_{\rm H_2} \lesssim 10^{-5}$ (e.g. Ledoux et al. 2003; Noterdaeme et al. 2008). Detections of H$_2$ absorption have been obtained in DLAs with relatively high metallicity and dust depletion, [X/Fe] $>$0.4 (Noterdaeme et al. 2008). This is consistent with the anticorrelation obtained between the spin temperature and metallicity, as high-metallicity absorbers should have higher CNM fractions and are thus more likely to form the molecular phase.

Unfortunately, there are at present only nine DLAs with estimates of both $f_{\rm CNM}$ and $f_{\rm H_2}$. Most of these have also been observed in the C II* λ1335.7 line and are listed in the upper part of Table 6. Three additional systems with searches for H I 21 cm and H$_2$, but not C II* λ1335.7, absorption are listed in the lower part of the table. Both H$_2$ absorbers of this sub-sample, at $z = 1.7764$ towards 1331+170 and $z = 3.3869$ towards 0201+113, show H I 21 cm absorption. However, H$_2$ absorption was not detected in two H I 21 cm absorbers, at $z = 2.0395$ towards 0458−020 and $z = 2.3476$ towards 0438−436. Five DLAs were detected in neither H I 21 cm nor H$_2$ absorption, with strong upper limits on the molecular fraction (log[$f_{\rm H_2}$] $<$ −5) and lower limits on the spin temperature ($T_{\rm s} > 500$ K). The small sample size makes it difficult to draw any inferences from these results, especially given that all DLAs of the sample have high spin temperatures, $T_{\rm s} \gtrsim 500$ K. Searches for H$_2$ absorption in DLAs with low spin temperatures would be of much interest.

8 SUMMARY

We have carried out a deep search for redshifted H I 21 cm absorption in a large sample of DLAs at 0.68 $< z <$ 3.44 with the GMRT, the GBT and the WSRT. This has yielded detections of H I 21 cm absorption in two new DLAs, at $z = 3.387$ towards 0201+113 and $z = 2.347$ towards 0438−436, and confirmations of detections in two known H I 21 cm absorbers. We present evidence that the H I 21 cm absorption from one of the DLAs, at $z = 2.0395$ towards 0458−020, has varied on time-scales of $\approx$2 months. Similar variability in the H I 21 cm absorption profile has been earlier reported on even shorter time-scales in two DLAs.

We have also used the VLBA to obtain high-spatial-resolution images of a sample of background quasars with foreground DLAs or H I 21 cm absorbers at frequencies close to the redshifted H I 21 cm line frequency, in order to estimate the quasar core fraction. We assume that the DLA covering factor is the same as this core fraction. We have used our measurements of the H I 21 cm optical depth and the DLA covering factor in conjunction with the known H I column density from the Lyman α profile to estimate the spin temperature of each absorber. Finally, we report metallicity, abundance and velocity width measurements for a set of DLAs with H I 21 cm absorption spectroscopy, from either our own observations or archival data.

We have combined our results with data from the literature to compile a sample of 37 DLAs with spin temperatures derived from a combination of the Lyman α profile, H I 21 cm absorption spectroscopy and low-frequency VLBI estimates of the absorber covering factor. This sample does not include PDLAs, where the spin temperature could be influenced by the proximity of the absorber to the background quasar, or sub-DLAs, where the spin temperature may be affected by self-shielding issues. The H I column density distribution of this sample is statistically indistinguishable from that of the much larger sample of all known DLAs, including absorbers detected in the SDSS. 29 DLAs of the sample have estimates of the gas metallicity [Z/H], 26 of the dust depletion [Z/Fe] and 24 of the velocity width between 90 per cent optical depth points, ΔV_{90}.

The main results of the paper are as follows.

(i) We find that the spatial extent of the quasar radio core at the foreground absorber redshift (as estimated from the VLBI images) is larger for high-z DLAs than for low-z DLAs. However, these are *upper limits* to the transverse core size, due to the possibility of residual phase errors in the VLBA data. This is especially important for lower frequency VLBI images, due to ionospheric effects; DLAs at $z > 2$ are thus the worst affected of the sample. Despite this, the median upper limit to the transverse core size is $\approx$130 pc for the full sample, while that for $z > 2$ DLAs is $\approx$350 pc. For all DLAs but one, the maximum value for the (upper limit to the) transverse core size is $\approx$1 kpc. These are significantly lower than the size of a typical galaxy. We conclude that the foreground DLAs are likely to cover at least the radio cores for all the 37 DLAs of the sample.

(ii) We have examined whether the use of the H I column density derived from the pencil-beam optical sightline in the equation for the H I 21 cm optical depth for the sightline towards the radio emission can cause systematic effects in the spin temperature estimates. This was done by smoothing a high-spatial-resolution (15 pc) H I 21 cm emission cube of the LMC to coarser resolutions, out to $\approx$1 kpc, to test whether the H I column densities measured from the smoothed spectral cubes are systematically different from those at the highest spatial resolution. We find that the H I column densities in the smoothed cube are systematically larger than those in the 15 pc cube for $N_{H_I} \lesssim 1 \times 10^{21}$ cm^{-2} and systematically lower than those in the 15 pc cube for $N_{H_I} \gtrsim 1 \times 10^{21}$ cm^{-2}. In other words, the use of the H I column density from the damped Lyman α profile in the equation for the H I 21 cm optical depth will tend to underestimate the spin temperature for DLAs with $N_{H_I} \lesssim 1 \times 10^{21}$ cm^{-2}, and to overestimate the spin temperature for DLAs with $N_{H_I} \gtrsim 1 \times 10^{21}$ cm^{-2} (assuming that the spatial distribution of neutral gas in DLAs is similar to that in the LMC). We estimated the magnitude of this effect at two spatial resolutions, 67 and 345 pc, approximately the median transverse size of the radio cores at the DLA redshifts for DLAs at $z < 2$ and $z > 2$, respectively. We find that the effect is not very significant, within a factor of 25 per cent for most of the DLAs of the sample, except for systems at low and very high N_{H_I} values

($N_{\rm HI} < 4 \times 10^{20}$ cm^{-2} and $N_{\rm HI} > 5.5 \times 10^{21}$ cm^{-2}, respectively) and with large core sizes. At these extremes of the $N_{\rm HI}$ distribution, the spin temperature could be underestimated by up to a factor of 2 for $N_{\rm HI} \approx 2 \times 10^{20}$ cm^{-2} or overestimated by up to a factor of 1.5 for $N_{\rm HI} \approx 6 \times 10^{21}$ cm^{-2}. Since there are far more DLAs at low $N_{\rm HI}$ values than at extremely high ones, the overall effect is to give a weak bias of the spin temperature distribution of high-z DLAs towards lower values.

(iii) We have examined the full sample of DLAs for trends between different quantities, including the detection rate of H I 21 cm absorption, the spin temperature, the H I column density, the covering factor, the metallicity, the dust depletion, the velocity width at 90 per cent optical depth, etc. Survival analysis methods, as implemented in the ASURV package, were used to appropriately handle censored data.

We found no evidence that the detection rate of H I 21 cm absorption depends on the H I column density, the absorber covering factor, the DLA metallicity or the velocity width at 90 per cent optical depth. For all these variables, the detection rates of H I 21 cm absorption above and below the median value were found to be consistent with each other within the statistical uncertainties. Similarly, there is no statistically significant evidence that the estimated DLA spin temperatures depend on the absorber covering factor, the H I column density or the velocity width at 90 per cent optical depth. However, we caution that the sample size of DLAs with H I 21 cm absorption studies is still quite small and the above detection rates are dominated by Poisson errors. It is plausible that larger absorber samples will indeed show that the detection rates do depend on, e.g., the metallicity and the covering factor.

The detection rate of H I 21 cm absorption in high-z DLAs (with $z > z_{\rm med}$, where $z_{\rm med} = 2.192$) is 17^{+16}_{-9} per cent, while that in low-z DLAs (with $z < z_{\rm med}$) is 83^{+17}_{-21} per cent. The difference between the two detection rates has $\approx 2.6\sigma$ significance. This is tentative evidence that the probability of detecting H I 21 cm absorption increases with decreasing redshift.

(iv) We detect a difference between the spin temperature distributions of absorbers above and below the median redshift, $z_{\rm med} = 2.192$, at $\approx 3.5\sigma$ significance. The statistical significance of the difference in $T_{\rm s}$ distributions is even higher, 4.0σ, if the redshift $z = 2.4$ is used to demarcate the low-z and high-z samples.

We have also restricted the low-z sample to absorbers with redshifts $z > 1$, to ensure that the angular diameter distances of the DLAs and their background quasars are similar for all absorbers. Again sub-dividing the sample into low-z ($z < 2.683$) and high-z ($z > 2.683$) DLAs yields a clear difference, with 3.5σ statistical significance, between the $T_{\rm s}$ distributions of the two sub-samples. Angular diameter distances thus do not appear to play a significant role in the lower H I 21 cm optical depths observed in high-z DLAs. We conclude that DLA spin temperatures show clear redshift evolution: the high-z sample contains both a smaller fraction of DLAs with low spin temperatures and a lower detection rate of H I 21 cm absorption.

(v) We also find that the spin temperature distributions in the full sample of DLAs and in the Milky Way are different, at $\approx 6\sigma$ significance. This is definitive evidence that the neutral ISM in DLAs is significantly different from that in the Galaxy, with far smaller CNM fractions ($\lesssim 20$ per cent) in DLAs than in the Milky Way (median CNM fraction ≈ 27 per cent).

(vi) We continue to find that the DLA metallicities and their spin temperatures are anticorrelated: the anticorrelation between [Z/H] and $T_{\rm s}$ is detected at $\approx 3.5\sigma$ significance in a generalized Kendall-tau test, based on 29 absorbers with estimates of metallicity,

spin temperature and covering factor. This supports the conjecture of Kanekar & Chengalur ([2001b](#)) that the low CNM fractions in DLAs arise due to a paucity of cooling routes in the absorbers, due to their low metallicities. Differences between the H I column densities along the radio and optical sightlines can only worsen any existing anticorrelation. We find only weak ($\approx 2.4\sigma$) evidence for an anticorrelation between $T_{\rm s}$ and dust depletion, from 26 systems. It is thus unlikely that the relation between the spin temperature and metallicity arises due to an underlying relation between the spin temperature and dust depletion.

The DLA spin temperature estimates are based on the assumptions that the quasar core fraction can be interpreted as the DLA covering factor and that the H I column density measured towards the optical quasar is the same as that towards the more extended radio emission. The metallicity estimates do not make either of these assumptions. If the above assumptions are violated for most of the absorbers, we would not expect to detect an underlying relation between $T_{\rm s}$ and [Z/H]. The fact that the predicted anticorrelation between $T_{\rm s}$ and [Z/H] is indeed detected indicates that the assumptions are reliable, at least in a statistical sense.

(vii) We have also examined whether the two main results of this paper, namely the redshift evolution of DLA spin temperatures and the anticorrelation between the spin temperature and metallicity, are affected by the assumption that the DLA covering factor is equal to the quasar radio core fraction. This was done via Monte Carlo simulations with DLA spin temperatures inferred assuming (1) an error in the inferred covering factor, with standard deviation ranging from 10 to 100 per cent of the measured core fraction, and (2) entirely random covering factors, selected from a uniform distribution of values between 0 and 1. For both types of errors, the above two results were obtained at $\gtrsim 3\sigma$ significance, after averaging over 10 000 Monte Carlo runs. Our results thus do not appear to critically depend on the assumption that the DLA covering factor is equal to the quasar radio core fraction.

(viii) We have examined the C II* $\lambda 1335.7$ model of Wolfe et al. ([2003a](#), [2004](#)) in the light of our spin temperature estimates. We find that the C II* $\lambda 1335.7$ results are entirely consistent with our results for at least half the DLA sample, the systems with low metallicities and undetected or weak C II* $\lambda 1335.7$ absorption. The anticorrelation between the metallicity and spin temperature implies that the neutral ISM in such systems should be predominantly WNM, as expected from the low cooling rates derived from the C II* $\lambda 1335.7$ model. Similarly, DLAs with high metallicity are expected to have high CNM fractions based on the $T_{\rm s}$–[Z/H] anticorrelation and are also expected to have a high cooling rate from their strong C II* $\lambda 1335.7$ absorption; the spin temperature and C II* $\lambda 1335.7$ results are thus also in agreement for such systems. Thus, the C II* $\lambda 1335.7$ results are broadly consistent with the spin temperature results except for a few cases where line-of-sight effects may be important. Further, even for these cases, the apparent discrepancy between the spin temperature and C II* $\lambda 1335.7$ results arises for systems with intermediate metallicity, [Z/H] ≈ -1.3. We find that the difference essentially arises because Wolfe et al. ([2003b](#), [2004](#)) use a CNM+WNM model with 50 per cent of the neutral gas in each phase; such a model is not required by the C II* $\lambda 1335.7$ data. It appears possible to alleviate the apparent discrepancy between the C II* $\lambda 1335.7$ and the H I 21 cm results by considering a model wherein 10–20 per cent of the H I in intermediate-metallicity DLAs is in the CNM, producing the majority of the C II* $\lambda 1335.7$ absorption. Such a two-phase model would yield both strong C II* $\lambda 1335.7$ absorption and a high spin temperature ($T_{\rm s} \approx 1000$ K). While it is beyond the scope of the present work to explicitly test this

possibility, we conclude that there is no significant disagreement between the C II* λ1335.7 results and the spin temperature estimates.

REFERENCES

Abazajian K. N. et al., 2009, ApJS, 182, 543
Akerman C. J., Ellison S. L., Pettini M., Steidel C. C., 2005, A&A, 440, 499
Akritas M. G., Bershady M. A., 1996, ApJ, 470, 706
Asplund M., Grevesse N., Sauval A. J., Scott P., 2009, ARA&A, 47, 481
Bakes E. L. O., Tielens A. G. G. M., 1994, ApJ, 427, 822
Battisti A. J., Meiring J. D., Tripp T. M., Prochaska J. X., Werk J. K., Jenkins E. B., Lehner N., Tumlinson J., Thom C., 2012, ApJ, 744, 93
Becker R. H., White R. L., Helfand D. J., 1995, ApJ, 450, 559
Bergeron J., Stasińska G., 1986, A&A, 169, 1
Boisse P., Le Brun V., Bergeron J., Deharveng J.-M., 1998, A&A, 333, 841
Bowen D. V., Tripp T. M., Jenkins E. B., 2001, AJ, 121, 1456
Braun R., Walterbos R., 1992, ApJ, 386, 120
Briggs F. H., 1983, AJ, 88, 239
Briggs F. H., Wolfe A. M., 1983, ApJ, 268, 76
Briggs F. H., Wolfe A. M., Liszt H. S., Davis M. M., Turner K. L., 1989, ApJ, 341, 650
Briggs F. H., Brinks E., Wolfe A. M., 1997, AJ, 113, 467
Briggs F. H., de Bruyn A. G., Vermeulen R. C., 2001, A&A, 373, 113
Brown R. L., Mitchell K. J., 1983, ApJ, 264, 87
Brown R. L., Roberts M. S., 1973, ApJ, 184, L7
Brown R. L., Spencer R. E., 1979, ApJ, 230, L1
Brown B. W. M., Hollander M., Korwar R. M., 1974, in Proschan F., Serfling R. J., eds, Reliability and Biometry. SIAM, Philadelphia, p. 327
Burbidge E. M., Beaver E. A., Cohen R. D., Junkkarinen V. T., Lyons R. W., 1996, AJ, 112, 2533
Carilli C. L., Lane W. M., de Bruyn A. G., Braun R., Miley G. K., 1996, AJ, 111, 1830
Carswell R. F., Jorgenson R. A., Wolfe A. M., Murphy M. T., 2011, MNRAS, 411, 2319
Catinella B., Haynes M. P., Giovanelli R., Gardner J. P., Connolly A. J., 2008, ApJ, 685, L13
Chen H.-W., Kennicutt R. C., Jr, Rauch M., 2005, ApJ, 620, 703
Chengalur J. N., Kanekar N., 1999, MNRAS, 302, L29
Chengalur J. N., Kanekar N., 2000, MNRAS, 318, 303
Chengalur J. N., Kanekar N., 2002, A&A, 388, 383
Chengalur J. N., Kanekar N., 2003, Phys. Rev. Lett., 91, 241302
Colgan S. W. J., Salpeter E. E., Terzian Y., 1988, ApJ, 328, 275
Condon J. J., Cotton W. D., Greisen E. W., Yin Q. F., Perley R. A., Taylor G. B., Broderick J. J., 1998, AJ, 115, 1693
Cooke R., Pettini M., Steidel C. C., Rudie G. C., Nissen P. E., 2011, MNRAS, 417, 1534
Cui J., Bechtold J., Ge J., Meyer D. M., 2005, ApJ, 633, 649
Curran S. J., 2012, ApJ, 748, L18
Curran S. J., Webb J. K., 2006, MNRAS, 371, 356
Curran S. J., Murphy M. T., Pihlström Y. M., Webb J. K., Purcell C. R., 2005, MNRAS, 356, 1509
Curran S. J., Tzanavaris P., Pihlström Y. M., Webb J. K., 2007, MNRAS, 382, 1331
Curran S. J., Tzanavaris P., Darling J. K., Whiting M. T., Webb J. K., Bignell C., Athreya R., Murphy M. T., 2010, MNRAS, 402, 35
de Bruyn A. G., O'Dea C. P., Baum S. A., 1996, A&A, 305, 450
de la Varga A., Reimers D., Tytler D., Barlow T., Burles S., 2000, A&A, 363, 69
Dessauges-Zavadsky M., Calura F., Prochaska J. X., D'Odorico S., Matteucci F., 2004, A&A, 416, 79
Dessauges-Zavadsky M., Prochaska J. X., D'Odorico S., Calura F., Matteucci F., 2006, A&A, 445, 93
Dessauges-Zavadsky M., Calura F., Prochaska J. X., D'Odorico S., Matteucci F., 2007, A&A, 470, 431
Dickey J. M., Lockman F. J., 1990, ARA&A, 28, 215
Douglas J. N., Bash F. N., Bozyan F. A., Torrence G. W., Wolfe C., 1996, AJ, 111, 1945
Drinkwater M. J., Webb J. K., Barrow J. D., Flambaum V. V., 1998, MNRAS, 295, 457
Ellison S. L., Ryan S. G., Prochaska J. X., 2001a, MNRAS, 326, 628
Ellison S. L., Yan L., Hook I. M., Pettini M., Wall J. V., Shaver P., 2001b, A&A, 379, 393
Ellison S. L., Pettini M., Steidel C. C., Shapley A. E., 2001c, ApJ, 549, 770
Ellison S. L., Yan L., Hook I. M., Pettini M., Wall J. V., Shaver P., 2002, A&A, 383, 91
Ellison S. L., York B. A., Pettini M., Kanekar N., 2008, MNRAS, 388, 1349
Ellison S. L., Kanekar N., Prochaska J. X., Momjian E., Worseck G., 2012, MNRAS, 424, 293
Erb D. K., Shapley A. E., Pettini M., Steidel C. C., Reddy N. A., Adelberger K. L., 2006, ApJ, 644, 813
Field G. B., 1958, Proc. IRE, 46, 240
Field G. B., 1959, ApJ, 129, 536
Field G. B., Goldsmith D. W., Habing H. J., 1969, ApJ, 155, L149
Fontana A., Ballester P., 1995, The Messenger, 80, 37
Fumagalli M., O'Meara J. M., Prochaska J. X., Kanekar N., 2010, MNRAS, 408, 362
Fynbo J. P. U. et al., 2010, MNRAS, 408, 2128
Fynbo J. P. U. et al., 2011, MNRAS, 413, 2481
Ge J., Bechtold J., 1997, ApJ, 477, L73

Ge J., Bechtold J., Kulkarni V. P., 2001, ApJ, 547, L1

Gehrels N., 1986, ApJ, 303, 336

Gupta N., Srianand R., Petitjean P., Noterdaeme P., Saikia D. J., 2009, MNRAS, 398, 201

Gwinn C. R., 2001, ApJ, 561, 815

Haehnelt M. G., Steinmetz M., Rauch M., 1998, ApJ, 495, 64

Heiles C., Troland T. H., 2003a, ApJS, 145, 329

Heiles C., Troland T. H., 2003b, ApJ, 586, 1067

Heinmüller J., Petitjean P., Ledoux C., Caucci S., Srianand R., 2006, A&A, 449, 33

Isobe T., Feigelson E. D., Nelson P. I., 1986, ApJ, 306, 490

Jorgenson R. A., Wolfe A. M., Prochaska J. X., Lu L., Howk J. C., Cooke J., Gawiser E., Gelino D. M., 2006, ApJ, 646, 730

Jorgenson R. A., Wolfe A. M., Prochaska J. X., 2010, ApJ, 722, 460

Junkkarinen V. T., Cohen R. D., Beaver E. A., Burbidge E. M., Lyons R. W., Madejski G., 2004, ApJ, 614, 658

Kanekar N., Briggs F. H., 2004, New Astron. Rev., 48, 1259

Kanekar N., Chengalur J. N., 1997, MNRAS, 292, 831

Kanekar N., Chengalur J. N., 2001a, MNRAS, 325, 631

Kanekar N., Chengalur J. N., 2001b, A&A, 369, 42

Kanekar N., Chengalur J. N., 2003, A&A, 399, 857

Kanekar N., Chengalur J. N., 2005, in Williams P., Shu C.-G., Menard B., eds, IAU Colloq. 199: Probing Galaxies through Quasar Absorption Lines. Cambridge Univ. Press, Cambridge, p. 156

Kanekar N., Ghosh T., Chengalur J. N., 2001, A&A, 373, 394

Kanekar N., Subrahmanyan R., Chengalur J. N., Safouris V., 2003, MNRAS, 346, L57

Kanekar N., Subrahmanyan R., Ellison S. L., Lane W. M., Chengalur J. N., 2006, MNRAS, 370, L46

Kanekar N., Chengalur J. N., Lane W. M., 2007, MNRAS, 375, 1528

Kanekar N., Lane W. M., Momjian E., Briggs F. H., Chengalur J. N., 2009a, MNRAS, 394, L61

Kanekar N., Prochaska J. X., Ellison S. L., Chengalur J. N., 2009b, MNRAS, 396, 385

Kanekar N., Smette A., Briggs F. H., Chengalur J. N., 2009c, ApJ, 705, L40

Kanekar N., Braun R., Roy N., 2011, ApJ, 737, L33

Kanekar N., Ellison S. L., Momjian E., York B., Pettini M., 2013, MNRAS, 428, 532

Kellermann K. I., Pauliny-Toth I. I. K., 1969, ApJ, 155, L71

Khare P., Kulkarni V. P., Lauroesch J. T., York D. G., Crotts A. P. S., Nakamura O., 2004, ApJ, 616, 86

Kim S., Staveley-Smith L., Dopita M. A., Sault R. J., Freeman K. C., Lee Y., Chu Y.-H., 2003, ApJS, 148, 473

Kulkarni V. P., Fall S. M., Lauroesch J. T., York D. G., Welty D. E., Khare P., Truran J. W., 2005, ApJ, 618, 68

Kulkarni V. P., Khare P., Som D., Meiring J., York D. G., Péroux C., Lauroesch J. T., 2010, New Astron., 15, 735

Lane W., Smette A., Briggs F., Rao S., Turnshek D., Meylan G., 1998, AJ, 116, 26

Lane W. M., Briggs F. H., Smette A., 2000, ApJ, 532, 146

Lanzetta K. M., Bowen D. V., 1992, ApJ, 391, 48

Launay J.-M., Roueff E., 1977, J. Phys. B: At. Mol. Phys., 10, 879

le Brun V., Bergeron J., Boissé P., Deharveng J.-M., 1997, A&A, 321, 733

Ledoux C., Bergeron J., Petitjean P., 2002, A&A, 385, 802

Ledoux C., Petitjean P., Srianand R., 2003, MNRAS, 346, 209

Ledoux C., Petitjean P., Fynbo J. P. U., Møller P., Srianand R., 2006, A&A, 457, 71

Levshakov S. A., Varshalovich D. A., 1985, MNRAS, 212, 517

Lindler D., 1999, STIS-IDT CALSTIS Manual. NASA/LASP, Greenbelt, MD

Liszt H., 2001, A&A, 371, 698

Lopez S., Ellison S. L., 2003, A&A, 403, 573

Lopez S., Reimers D., Gregg M. D., Wisotzki L., Wucknitz O., Guzman A., 2005, ApJ, 626, 767

Lu L., Wolfe A. M., Turnshek D. A., Lanzetta K. M., 1993, ApJS, 84, 1

Lu L., Sargent W. L. W., Barlow T. A., Churchill C. W., Vogt S. S., 1996, ApJS, 107, 475

Macquart J.-P., 2005, A&A, 433, 827

McKee C. F., Ostriker J. P., 1977, ApJ, 218, 148

Meyer D. M., York D. G., Black J. H., Chaffee F. H., Jr, Foltz C. B., 1986, ApJ, 308, L37

Milutinovic N., Ellison S. L., Prochaska J. X., Tumlinson J., 2010, MNRAS, 408, 2071

Møller P., Warren S. J., 1993, A&A, 270, 43

Møller P., Warren S. J., Fynbo J. U., 1998, A&A, 330, 19

Møller P., Fynbo J. P. U., Fall S. M., 2004, A&A, 422, L33

Monier E. M., Turnshek D. A., Rao S., 2009, MNRAS, 397, 943

Murphy M. T., Curran S. J., Webb J. K., Ménager H., Zych B. J., 2007, MNRAS, 376, 673

Neeleman M. et al., 2013, ApJ, submitted

Nestor D., Pettini M., Hewett P., Rao S., Wild V., 2008, MNRAS, 390, 1670

Noterdaeme P., Ledoux C., Petitjean P., Srianand R., 2008, A&A, 481, 327

Noterdaeme P., Petitjean P., Ledoux C., Srianand R., 2009, A&A, 505, 1087

Noterdaeme P., Petitjean P., Srianand R., Ledoux C., López S., 2011, A&A, 526, L7

Noterdaeme P. et al., 2012a, A&A, 540, 63

Noterdaeme P. et al., 2012b, A&A, 547, L1

Nulsen P. E. J., Barcons X., Fabian A. C., 1998, MNRAS, 301, 168

Penprase B. E., Prochaska J. X., Sargent W. L. W., Toro-Martinez I., Beeler D. J., 2010, ApJ, 721, 1

Péroux C., Dessauges-Zavadsky M., D'Odorico S., Kim T., McMahon R. G., 2003, MNRAS, 345, 480

Péroux C., Bouché N., Kulkarni V. P., York D. G., Vladilo G., 2012, MNRAS, 419, 3060

Petitjean P., Srianand R., Ledoux C., 2000, A&A, 364, L26

Petitjean P., Ledoux C., Noterdaeme P., Srianand R., 2006, A&A, 456, L9

Petitjean P., Ledoux C., Srianand R., 2008, A&A, 480, 349

Pettini M., Smith L. J., Hunstead R. W., King D. L., 1994, ApJ, 426, 79

Pettini M., Smith L. J., King D. L., Hunstead R. W., 1997, ApJ, 486, 665

Pettini M., Ellison S. L., Steidel C. C., Bowen D. V., 1999, ApJ, 510, 576

Pettini M., Ellison S. L., Steidel C. C., Shapley A. E., Bowen D. V., 2000, ApJ, 532, 65

Pettini M., Zych B. J., Steidel C. C., Chaffee F. H., 2008, MNRAS, 385, 2011

Planck Collaboration, 2013, preprint (arXiv:1303.5076)

Pottasch S. R., Wesselius P. R., van Duinen R. J., 1979, A&A, 74, L15

Prochaska J. X., 1999, ApJ, 511, L71

Prochaska J. X., Wolfe A. M., 1997, ApJ, 487, 73

Prochaska J. X., Wolfe A. M., 1999, ApJS, 121, 369

Prochaska J. X., Wolfe A. M., 2009, ApJ, 696, 1543

Prochaska J. X., Wolfe A. M., 2010, preprint (arXiv:1009.3960)

Prochaska J. X. et al., 2001, ApJS, 137, 21

Prochaska J. X., Gawiser E., Wolfe A. M., Cooke J., Gelino D., 2003a, ApJS, 147, 227

Prochaska J. X., Gawiser E., Wolfe A. M., Castro S., Djorgovski S. G., 2003b, ApJ, 595, L9

Prochaska J. X., Herbert-Fort S., Wolfe A. M., 2005, ApJ, 635, 123

Prochaska J. X., Wolfe A. M., Howk J. C., Gawiser E., Burles S. M., Cooke J., 2007, ApJS, 171, 29

Prochaska J. X., Chen H.-W., Wolfe A. M., Dessauges-Zavadsky M., Bloom J. S., 2008a, ApJ, 672, 59

Prochaska J. X., Hennawi J. F., Herbert-Fort S., 2008b, ApJ, 675, 1002

Rafelski M., Wolfe A. M., Prochaska J. X., Neeleman M., Mendez A. J., 2012, ApJ, 755, 89

Rao S. M., Turnshek D. A., 1998, ApJ, 500, L115

Rao S. M., Turnshek D. A., 2000, ApJS, 130, 1

Rao S. M., Turnshek D. A., Nestor D. B., 2006, ApJ, 636, 610

Readhead A. C. S., 1994, ApJ, 426, 51

Roberts M. S., Brown R. L., Brundage W. D., Rots A. H., Haynes M. P., Wolfe A. M., 1976, AJ, 81, 293

Rohlfs K., Wilson T. L., 2006, Tools of Radio Astronomy, 4th edn. Springer, Berlin

Roy N., Mathur S., Gajjar V., Patra N. N., 2013, MNRAS, 436, L94

Ryan-Weber E. V., Staveley-Smith L., Webster R. L., 2005, MNRAS, 364, L51

Savage B. D., Sembach K. R., 1991, ApJ, 379, 245

Savaglio S. et al., 2005, ApJ, 635, 260

Schaye J., 2001, ApJ, 562, L95

Singal A. K., 2009, ApJ, 703, L109

Smette A., Robertson J. G., Shaver P. A., Reimers D., Wisotzki L., Koehler T., 1995, A&AS, 113, 199

Srianand R., Petitjean P., Ledoux C., Ferland G., Shaw G., 2005, MNRAS, 362, 549

Srianand R., Gupta N., Petitjean P., Noterdaeme P., Ledoux C., 2010, MN-RAS, 405, 1888

Srianand R., Gupta N., Petitjean P., Noterdaeme P., Ledoux C., Salter C. J., Saikia D. J., 2012, MNRAS, 421, 651

Steidel C. C., Bowen D. V., Blades J. C., Dickinson M., 1995, ApJ, 440, L45

Storrie-Lombardi L. J., Wolfe A. M., 2000, ApJ, 543, 552

Tremonti C. A. et al., 2004, ApJ, 613, 898

Viegas S. M., 1995, MNRAS, 276, 268

Vogt S. S. et al., 1994, in Crawford D. L., Craine E. R., eds, Proc. SPIE Conf. Ser. Vol. 2198, HIRES: The High-Resolution Echelle Spectrometer on the Keck 10-m Telescope. SPIE, Bellingham, p. 362

Wakker B. P., Lockman F. J., Brown J. M., 2011, ApJ, 728, 159

Warren S. J., Møller P., Fall S. M., Jakobsen P., 2001, MNRAS, 326, 759

Welty D. E., Xue R., Wong T., 2012, ApJ, 745, 173

White R. L., Kinney A. L., Becker R. H., 1993, ApJ, 407, 456

Wolfe A. M., Burbidge G. R., 1975, ApJ, 200, 548

Wolfe A. M., Davis M. M., 1979, AJ, 84, 699

Wolfe A. M., Prochaska J. X., 1998, ApJ, 494, L15

Wolfe A. M., Broderick J. J., Condon J. J., Johnston K. J., 1976, ApJ, 208, L47

Wolfe A. M., Briggs F. H., Jauncey D. L., 1981, ApJ, 248, 460

Wolfe A. M., Briggs F. H., Davis M. M., 1982, ApJ, 259, 495

Wolfe A. M., Briggs F. H., Turnshek D. A., Davis M. M., Smith H. E., Cohen R. D., 1985, ApJ, 294, L67

Wolfe A. M., Turnshek D. A., Lanzetta K. M., Lu L., 1993, ApJ, 404, 480

Wolfe A. M., Prochaska J. X., Gawiser E., 2003a, ApJ, 593, 215

Wolfe A. M., Gawiser E., Prochaska J. X., 2003b, ApJ, 593, 235

Wolfe A. M., Howk J. C., Gawiser E., Prochaska J. X., Lopez S., 2004, ApJ, 615, 625

Wolfe A. M., Gawiser E., Prochaska J. X., 2005, ARA&A, 43, 861

Wolfe A. M., Jorgenson R. A., Robishaw T., Heiles C., Prochaska J. X., 2008a, Nature, 455, 638

Wolfe A. M., Prochaska J. X., Jorgenson R. A., Rafelski M., 2008b, ApJ, 681, 881

Wolfire M. G., Hollenbach D., McKee C. F., Tielens A. G. G. M., Bakes E. L. O., 1995, ApJ, 443, 152

Wolfire M. G., McKee C. F., Hollenbach D., Tielens A. G. G. M., 2003, ApJ, 587, 278

Wright E. L. et al., 1991, ApJ, 381, 200

York B. A., Kanekar N., Ellison S. L., Pettini M., 2007, MNRAS, 382, L53

Zuo L., Beaver E. A., Burbidge E. M., Cohen R. D., Junkkarinen V. T., Lyons R. W., 1997, ApJ, 477, 568

Zwaan M. A., van der Hulst J. M., Briggs F. H., Verheijen M. A. W., Ryan-Weber E. V., 2005, MNRAS, 364, 1467

Zwaan M., Walter F., Ryan-Weber E., Brinks E., de Blok W. J. G., Kennicutt R. C., 2008, AJ, 136, 2886

This paper has been typeset from a TEX/LATEX file prepared by the author.